ABSTRACT

Title of dissertation: MOTION COORDINATION OF MULTIPLE
                         AUTONOMOUS VEHICLES IN
                         A SPATIOTEMPORAL FLOWFIELD

                         Cameron Kai Peterson, Doctor of Philosophy, 2012

Dissertation directed by: Professor Derek Paley
                            Department of Aerospace Engineering

The long-term goal of this research is to provide theoretically justified control strategies to operate autonomous vehicles in spatiotemporal flowfields. The specific objective of this dissertation is to use estimation and nonlinear control techniques to generate decentralized control algorithms that enable motion coordination for multiple autonomous vehicles while operating in a time-varying flowfield. A cooperating team of vehicles can benefit from sharing data and tasking responsibilities. Many existing control algorithms promote collaboration of autonomous vehicles. However, these algorithms often fail to account for the degradation of control performance caused by flowfields. This dissertation presents decentralized multivehicle coordination algorithms designed for operation in a spatially or temporally varying flowfield. Each vehicle is represented using a Newtonian particle traveling in a plane at constant speed relative to the flow and subject to a steering control. Initially, we assume the flowfield is known and describe algorithms that stabilize a circular formation in a time-varying spatially nonuniform flow of moderate intensity. These algorithms are extended by relaxing the assumption that the flow is known: the vehicles dynamically estimate the flow and use that estimate in the control. We propose a distributed estimation and control algorithm comprising a consensus filter to share information gleaned from noisy position measurements, and an information filter to reconstruct a spatially varying flowfield. The theoretical results are illustrated with numerical simulations of circular formation control and validated in outdoor unmanned aerial vehicle (UAV) flight tests.

MOTION COORDINATION OF MULTIPLE AUTONOMOUS VEHICLES IN A SPATIOTEMPORAL FLOWFIELD

by

Cameron Kai Peterson

Dissertation submitted to the Faculty of the Graduate School of the
University of Maryland, College Park in partial fulfillment
of the requirements for the degree of
Doctor of Philosophy
2012

Advisory Committee:
Dr. Derek A. Paley, Chair/Advisor
Dr. Robert M. Sanner
Dr. J. Sean Humbert
Dr. David L. Akin
Dr. Balakumar Balachandran, Dean's Representative

Acknowledgments

I wish to thank my adviser, Dr. Derek Paley for his guidance, knowledge and time. He encouraged and supported me, gave me feedback on the problems and possibilities, made invaluable suggestions to correct and clarify my work, and patiently guided me through the process of completing my Ph.D. I am indebted to him for working with my non-traditional time constraints and never giving up on me throughout this process.

Table of Contents

List of Figures

Chapter 1

Introduction

In 1917, Archibald M. Lowe tested radio gear capable of remotely piloting an airplane. He used a small monoplane powered with a 35-horsepower engine to perform three test flights. In the first flight the airplane climbed too quickly causing it to stall and crash. The next two flights were made with a fixed elevator setting in order to prevent steep climbs, but that restricted the plane's maneuverability and those flights were also of short duration [72]. However, despite the limited flight time, Lowe demonstrated the ability to remotely command an airplane. From this inauspicious beginning great strides have been made, first in our ability to remotely pilot vehicles and subsequently in allowing the vehicles to autonomously control themselves.

Today autonomous vehicles are used in a wide variety of applications including aerobiological sampling [74], gathering in situ measurements of severe storms [18, 19], path planning of autonomous underwater gliders [40, 23], and much more [29, 12, 71, 20]. Recent research has focused on exploiting the synergy of multiple autonomous vehicles to cooperatively accomplish objectives [43, 62, 4, 42, 44, 28]. A cooperating team of vehicles can coordinate data collections and provide persistent coverage of continuous spatiotemporal processes like environmental fields or discrete processes such as moving ground targets. Unmanned platforms are particularly well-suited for

multiagent coordinated missions that require synoptic area coverage with consistent revisit rates. Many algorithms are capable of providing decentralized control of multiple agents with mobility and communication constraints [30, 65, 66, 49, 32, 22, 1].

The motion of an autonomous vehicle in the atmosphere or ocean can be disrupted by unknown flowfields such as winds or currents. These disturbances are difficult to model and may contribute to a significant portion of the vehicle's inertial velocity. Enabling cooperative control in the presence of a temporally and spatially varying flowfield is an ongoing challenge that we partially address in this dissertation. We provide cooperative control algorithms for multiple autonomous vehicles in the presence of 1) a known time-varying and spatially varying flowfield and 2) an unknown uniform or spatially varying flow.

Each vehicle is modeled as a planar, self-propelled particle that travels at unit speed relative to the flow. The flowfield magnitude is assumed to be of moderate intensity; that is, the flow speed does not exceed the vehicles' speed relative to the flow. (Motion coordination in strong, unknown flowfields is outside the scope of this dissertation [16].) This ensures that the vehicles will always maintain forward progress over ground. The particles are subject to a steering control perpendicular to the direction of motion relative to the flowfield. This model, also known as a unicycle model, is well suited to autonomous vehicles such as unmanned underwater vehicles (UUVs) or unmanned aerial vehicles (UAVs), which are continually in motion and operate primarily in a plane.

The steering control is designed to drive the particles into a circular formation

centered at either an arbitrary or prescribed location. We use Lyapunov theory and nonlinear techniques to develop a set of theoretically justified algorithms to cooperatively control multiple autonomous vehicles in the presence of a flowfield. Initially we assume that the flowfield is known and may be temporally and spatially varying. We then relax this assumption and provide observer-based control algorithms which simultaneously estimate the flowfield and use that estimate to stabilize a moving formation. Given a spatially uniform flowfield, each vehicle independently estimates the flow using noisy measurements of its own position. For a spatially varying flowfield, we provide a distributed estimation algorithm comprised of a consensus filter to share information garnered from noisy position measurements, and an information filter to reconstruct the flowfield.

1.1 Contributions of Dissertation

The contributions of this dissertation are the synthesis of theoretically justified control algorithms to cooperatively stabilize vehicles in the presence of a flowfield. Specifically they include:

1. *Multivehicle control algorithms for circular formations in a known, time-varying, and spatially varying flowfield*

    These controls are designed to drive vehicles into a circular formation centered at either a prescribed point or an arbitrary location determined by initial conditions.

2. *Multivehicle coordinated encirclement to a time-splay configuration for a uni-*

form flowfield that rotates in time

A time-splay configuration regulates the temporal distance between particles.

3. *Stabilization of cooperating vehicles to circular formations in a uniform or uniformly rotating flowfield when the vehicles are subject to turn-rate constraints*

   Incorporating a constraint provides more realistic behavior for vehicles with limited turning capacities, such as UAVs which turn by banking the aircraft, but have a limit on how far they can bank before stalling.

4. *Stabilization of circular formations in an estimated uniform flow using only noisy position measurements and knowledge of the vehicle's wind relative heading*

   Each vehicle individual estimates the flow and uses the estimate for motion coordination.

5. *Multivehicle estimation and control for circular formations in an unknown, spatially varying flowfield using noisy position measurements*

   Using a distributed information-consensus filter we estimate the coefficients of a parameterized flowfield. The estimated flowfield and its directional derivative at the vehicle locations are used in a decentralized control law that cooperatively stabilizes vehicles to a moving formation. We require only noisy position measurements to estimate the flow.

6. *Development of accelerating-frame dynamics to provide control algorithms which encircle maneuvering targets*

By accounting for target acceleration, one can follow targets as they execute realistic maneuvers. Simulation results demonstrate the utility of the control algorithms to this application.

7. *Hardware-in-the-loop (HIL) simulations and outdoor flight experiments*

   To compliment the theoretical work we also performed flight experiments on a UAV testbed. An HIL simulator was used to validate our motion coordination control algorithms. Once tested in the HIL simulator outdoor flight experiments were made on multiple UAVs.

1.2   Outline of Dissertation

The dissertation proceeds as follows. In Chapter 2 we explain the Newtonian-particle model used to describe the motion of a fleet of autonomous vehicles in an external flowfield. The model incorporates a constraint on the turn-rate to portray vehicles with limited turning capabilities. The coupling between the course over ground steering and the vehicle's low-level steering control is examined.

Chapter 3 develops Lyapunov-based circular control algorithms for the particle model in a known, time-varying flowfield. Control laws are given to drive particles to a circular formation with either a prescribed or arbitrary center point. We provide algorithms which stabilize circular formations when the vehicles are subject to a turn-rate constraint given a rotating or spatially uniform flowfield. For a uniform flowfield that rotates in time we also introduce a time-splay configuration which regulates the temporal spacing between particles. Regulating the spatial separation

between particles is a first step toward collision avoidance. However, it does not guarantee separation of the particles while they transition to the configuration. Overall collision avoidance is not addressed in this dissertation.

In Chapter 4 and Chapter 5 we relax the assumption that the flowfield is known and instead incorporate estimators into the control algorithms. Chapter 4 focuses on an observer-based algorithm for flowfields that are spatially uniform. We show that this estimator is robust to measurement noise. In Chapter 5 we provide motion coordination algorithms in a unknown spatially varying flowfield. This follows the work in [41] where an information-consensus filter was used as a decentralized estimator of a scalar field.

Chapter 6 applies the control algorithms developed in the previous chapters to the problem of target encirclement. We derive the equations of motion for an accelerating frame and provide performance results for circular configurations in a variety of flowfields induced in a moving reference frame that is attached to the maneuvering target.

In Chapter 7 we show the results from experimental flight tests. We apply the control laws developed in Chapter 3 to Procerus Unicorn UAVs. The modifications needed to employ these algorithms on the UAVs are outlined in this chapter. Hardware-in-the-loop simulations and experimental flight results are given.

Chapter 8 provides a summary of the work and highlights areas for ongoing research.

Chapter 2

Dynamic Vehicle Model in a Flowfield

This chapter presents the dynamical system used to describe an autonomous vehicle. Each vehicle is modeled as a planar, self-propelled particle moving at unit speed relative to a spatially and temporally variable flowfield. This model has been adopted frequently in previous works for a flow-free environment [65, 30, 79]. Each particle is steered by a gyroscopic control force that acts perpendicular to the velocity relative to the flow. The flow-relative steering control, denoted by u, is constrained for many systems. For example, with an unmanned aerial vehicle (UAV) one factor limiting the steering control is the degree which an aircraft can bank without stalling. To model this effect, we place a bound on the turn-rate by saturating u.

In Section 2.1 we provide the turn-rate constrained vehicle model. Section 2.2 derives the relationship between our low-level vehicle control and the inertial steering control.

2.1 Vehicle Model with Turn-Rate Constraint

The positions of N individual particles are denoted as r_k, where $k \in \{1, \ldots, N\}$. The inertial velocity of the kth particle is denoted by $\dot{r}_k$. The particles do not accelerate tangentially to their path and thus move with unit velocity $e^{i\theta_k}$ relative

to the flowfield. The flowfield at r_k and time t is denoted by $f_k(t) = f(r_k, t)$. The equations of motion for particle k are

$$
\begin{aligned}
\dot{r}_k &= e^{i\theta_k} + f_k(t) \\
\dot{\theta}_k &= \text{sat}(u_k; u_{max}),
\end{aligned}
\tag{2.1}
$$

where $u_{max} > 0$ and

$$
\text{sat}(u_k; u_{max}) = \begin{cases} -u_{max} & u_k < -u_{max} \\ u_k & -u_{max} \le u_k \le u_{max} \\ u_{max} & u_k > u_{max}. \end{cases}
\tag{2.2}
$$

For a vehicle with an unbounded turning rate, $u_{max} = \infty$ and the model (2.1) becomes

$$
\begin{aligned}
\dot{r}_k &= e^{i\theta_k} + f_k(t) \\
\dot{\theta}_k &= u_k.
\end{aligned}
\tag{2.3}
$$

Let $\gamma_k = \arg(\dot{r}_k)$ equal the orientation of the inertial velocity of the kth particle and $s_k(t) = s(t, r_k, \theta_k) = |\dot{r}_k|$ denote its magnitude. The particle model without the turn-rate constraint is equivalent to [54]

$$
\begin{aligned}
\dot{r}_k &= s_k(t)e^{i\gamma_k} \\
\dot{\gamma}_k &= \nu_k,
\end{aligned}
\tag{2.4}
$$

where ν_k is the angular rate of change of the inertial-velocity orientation. Note, it is required that $|f_k(t)| < 1$ for all k, t, to ensure $s_k(t) > 0$. This assumption guarantees that the particles will always exhibit forward motion in an inertial reference frame.

8
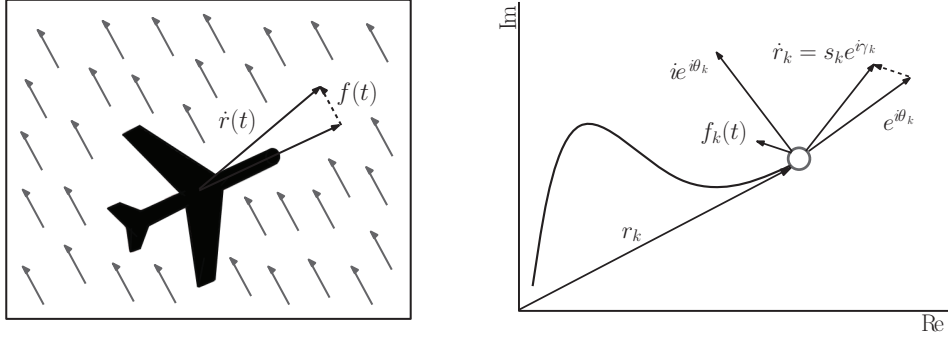
Figure 2.1: The inertial velocity of a particle is the sum of the flow velocity relative to the ground and the velocity of the particle relative to the flow.

Figure 2.1 illustrates the Newtonian particle model for an air vehicle. Figure 2.1(a) shows the dynamics in a flowfield; the inertial velocity is the sum of the velocity relative to the flow plus the velocity of the flow relative to the inertial (ground fixed) frame. Figure 2.1(b) shows the kth particle in the complex plane. The particle is located at r_k and its velocity relative to the flow is $e^{i\theta_k}$. In the presence of a flowfield f_k the inertial velocity of the particle is $\dot{r}_k = e^{i\theta_k} + f_k = s_k(t)e^{i\gamma_k}$. The steering control is applied in the direction $ie^{i\theta_k}$ which is perpendicular to the velocity relative to the flow.

Section 3.1 discusses stabilization of circular formations using the unconstrained model (2.4) in a known flow. In Section 3.2 we show that these results hold when using the turn-rate constrained model (2.1). The remaining chapters also use the unconstrained model, but relax the known-flow assumption.

2.2 Relationship of the Inertial and Flow-Relative Steering Control

The controller design of Chapter 3 focuses on obtaining a suitable inertial steering control ν_k; u_k is seen as the low-level controller used as input for an autonomous vehicle and should be recoverable from ν_k. Figure 2.1 exhibits the following relationship [54] between θ_k and γ_k:[1]

$$\sin \theta_k = s_k(t) \sin \gamma_k - \langle f_k(t), i \rangle \tag{2.5}$$

$$\cos \theta_k = s_k(t) \cos \gamma_k - \langle f_k(t), 1 \rangle, \tag{2.6}$$

which gives

$$\tan \gamma_k = \frac{\sin \theta_k + \langle f_k(t), i \rangle}{\cos \theta_k + \langle f_k(t), 1 \rangle}. \tag{2.7}$$

Differentiating (2.7) with respect to time and substituting in equations (2.5) and (2.6) yields

$$\dot{\gamma}_k = (\cos \theta_k \cos \gamma_k + \sin \theta_k \sin \gamma_k) s_k^{-1}(t) \dot{\theta}_k + \langle \dot{f}_k, i \rangle s_k^{-1}(t) \cos \gamma_k$$

$$- \langle \dot{f}_k, 1 \rangle s_k^{-1}(t) \sin \gamma_k \tag{2.8}$$

$$= (1 - s_k^{-1}(t) \langle e^{i\gamma_k}, f_k(t) \rangle) u_k + s_k^{-1}(t) \langle i e^{i\gamma_k}, \dot{f}_k \rangle \triangleq \nu_k, \tag{2.9}$$

with

$$\dot{f}_k = \frac{\partial f_k}{\partial r_k} \dot{r}_k + \frac{\partial f_k}{\partial t}. \tag{2.10}$$

---

[1]The inner product $\langle x, y \rangle = \mathrm{Re}\{\bar{x}y\}$ is used, where $x, y \in \mathbb{C}$ and $\bar{x}$ is the complex conjugate of x.

Solving for $u_k(t)$ provides the flow-relative steering control as a function of ν_k:

$$u_k(t) = \frac{s_k(t)\nu_k - \langle ie^{i\gamma_k}, \dot{f}_k \rangle}{s_k(t) - \langle e^{i\gamma_k}, f_k(t) \rangle}. \tag{2.11}$$

The preceding equation is well-defined everywhere. Because the denominator satisfies $s_k(t) - \langle e^{i\gamma_k}, f_k(t) \rangle \geq s_k(t) - |f_k(t)| > 0$ [54]. In the following examples $s_k(t)$ and $u_k(t)$ are calculated for a time-varying, spatially uniform flowfield and a time-varying, spatially nonuniform flowfield.

Example 1. Time-varying, spatially uniform flowfield

Let a uniform flow be defined as $f(t) = \eta(t)e^{i\xi(t)}$, where $\eta(t)$ is the magnitude of the flow and $\xi(t)$ is the direction. The k subscript is dropped from $f(t)$ since a uniform flow at time t is identical for all particles. It is assumed that $|\eta(t)| < 1$ for all t to ensure that $s_k(t) > 0$. The inertial speed is

$$s_k(t) = \sqrt{\text{Re}\{(\eta(t)e^{i\xi(t)} + e^{i\theta_k})(\eta(t)e^{-i\xi(t)} + e^{-i\theta_k})\}}$$
$$= \sqrt{1 + (\eta(t))^2 + 2\eta(t)(\cos\theta_k \cos\xi(t) + \sin\theta_k \sin\xi(t))}. \tag{2.12}$$

$s_k(t)$ is expressed as a function of γ_k and $f(t)$ by substituting (2.5) and (2.6) into (2.12) and rearranging the result to obtain the quadratic equation

$$(s_k(t))^2 - 2\eta(t)(\cos\gamma_k \cos\xi(t) + \sin\gamma_k \sin\xi(t))s_k(t) + (\eta(t))^2 - 1 = 0. \tag{2.13}$$

11

Equation (2.13) has the following solution (using the positive root since $s_k(t) > 0$):

$$
\begin{aligned}
s_k(t) &= \eta(t)(\cos\gamma_k\cos\xi(t) + \sin\gamma_k\sin\xi(t)) \\
&\quad + \sqrt{1 + (\eta(t))^2((\cos\gamma_k\cos\xi(t) + \sin\gamma_k\sin\xi(t))^2 - 1)} \quad (2.14) \\
&= \langle e^{i\gamma_k}, f(t)\rangle + \sqrt{1 - \langle ie^{i\gamma_k}, f(t)\rangle^2}. \quad (2.15)
\end{aligned}
$$

$u_k(t)$ is found by substituting $f(t) = \eta(t)e^{i\xi(t)}$ and $\dot{f}(t) = \dot{\eta}(t)e^{i\xi(t)} + i\eta(t)\dot{\xi}(t)e^{i\xi(t)}$ into (2.11) to obtain

$$
u_k(t) = \frac{\nu_k s_k(t) + \dot{\eta}(t)\sin(\gamma_k - \xi(t)) - \eta(t)\dot{\xi}(t)\cos(\gamma_k - \xi(t))}{s_k(t) - \eta(t)\cos(\gamma_k - \xi(t))}. \quad (2.16)
$$

This calculation shows that in order to use ν_k to compute the turn-rate control u_k in a time-varying flowfield the following variables need to be known: 1) the magnitude of the flowfield, $\eta(t)$, 2) the rate of change of the flowfield, $\dot{\eta}(t)$; and 3) the difference between the direction of the flow and the orientation of the inertial velocity, $\gamma_k - \xi(t)$.

Example 2. Time-varying, spatially nonuniform flowfield

For this example let $f_k(t) = \beta_k(t) + i\alpha_k(t)$, where $\beta_k(t) = \beta(t, r_k)$ and $\alpha_k(t) = \alpha(t, r_k)$ are the real and imaginary components of the flowfield. Computing $s_k(t)$ yields

$$
\begin{aligned}
s_k(t) &= \sqrt{\mathrm{Re}\{(e^{i\theta_k} + \beta_k(t) + i\alpha_k(t))(e^{-i\theta_k} + \beta_k(t) - i\alpha_k(t))\}} \\
&= \sqrt{1 - (\beta_k(t))^2 - (\alpha_k(t))^2 + 2s_k(t)(\alpha_k(t)\sin\gamma_k + \beta_k(t)\cos\gamma_k)}. \quad (2.17)
\end{aligned}
$$

Next $s_k(t)$ is expressed as a function of γ_k and $f_k(t)$. Squaring both sides of (2.17) and solving the resulting quadratic equation (using the positive root since $s_k(t) > 0$) gives

$$
\begin{aligned}
s_k(t) &= \alpha_k(t) \sin \gamma_k + \beta_k(t) \cos \gamma_k + \sqrt{1 - (\alpha_k(t) \cos \gamma_k - \beta_k(t) \sin \gamma_k)^2} \\
&= \langle e^{i\gamma_k}, f_k(t) \rangle + \sqrt{1 - \langle i e^{i\gamma_k}, f_k(t) \rangle^2}.
\end{aligned}
\tag{2.18}
$$

To solve for $u_k(t)$ let the position of particle k be $r_k = x_k + i y_k$. The time-derivative of $f_k(t)$ is

$$
\dot{f}_k(t) = \frac{\partial \beta_k}{\partial x_k} \dot{x}_k + \frac{\partial \beta_k}{\partial y_k} \dot{y}_k + \frac{\partial \beta_k}{\partial t} + i \left(\frac{\partial \alpha_k}{\partial x_k} \dot{x}_k + \frac{\partial \alpha_k}{\partial y_k} \dot{y}_k + \frac{\partial \alpha_k}{\partial t} \right).
$$

Substituting $\dot{f}_k$ into (2.11) yields

$$
u_k(t) = \frac{\nu_k s_k(t) - \sin \gamma_k \left(\frac{\partial \beta_k}{\partial x_k} \dot{x}_k + \frac{\partial \beta_k}{\partial y_k} \dot{y}_k + \frac{\partial \beta_k}{\partial t} \right) + \cos \gamma_k \left(\frac{\partial \alpha_k}{\partial x_k} \dot{x}_k + \frac{\partial \alpha_k}{\partial y_k} \dot{y}_k + \frac{\partial \alpha_k}{\partial t} \right)}{s_k(t) - \beta_k(t) \cos \gamma_k - \alpha_k(t) \sin \gamma_k}.
$$

$$
\tag{2.19}
$$

Thus, given the control, ν_k, the orientation of the inertial velocity, γ_k, the flowfield, $f_k(t)$, and the directional derivative $\dot{f}_k(t)$, one can solve for u_k, which is the control input to the vehicle model (2.1).

Chapter 3

Motion Coordination in a Known Flowfield

To operate effectively in real-world environments motion coordination algorithms must account for the complexity of flowfields which may be both temporally and spatially varying. Given a known, time-varying flowfield we provide motion coordination algorithms to steer multiple autonomous vehicles to circular formations.

This chapter builds upon prior coordination algorithms developed for flow-free and time-invariant flowfields. In a flow-free environment with both all-to-all [65] and limited [66] communication topologies Sepulchre et. al. provided constant-speed controllers to generate parallel, circular, and coordinated circular formations. Circular and coordinated circular formations were given in [54] for a time-invariant flowfield. We expand this work to also include time-varying flows.

The circular formations converge to an arbitrary center determined by initial conditions. For many applications it is useful to steer the formation to a specific location. To prescribe the center of our circular formation, we introduce a symmetry-breaking virtual particle. In [39] virtual particles were shown to change the dynamics of a group. Coordinated tracking using a virtual particle was shown when the communication topology is time-varying [9] and only partial state measurements are shared among the group [8]. We follow the work of [66] which used a virtual particle in a flow-free environment to specify the center of a circle.

We use only circles as a formation shape, however related work shows that this pattern can be expanded to convex paths in flow-free [53] and uniform flow [55, 73], closed curves [79], foliums and spirographs [16]. Other formation patterns can be created by allowing the circle center [2] and radius [3] to be time-varying.

We provide coordinated motion where the temporal spacing of the vehicles is regulated. A uniform separation of vehicles traveling around a circle using decentralized steering control was introduced in [65] for no flow. In the absence of a flowfield, the vehicles can be equally spaced both in space and time. Maintaining an equal angular separation in the presence of a flowfield may not be possible with a unit-speed vehicle model. A sliding-mode control algorithm was proposed in [32] that provides coordinated encirclement in a uniform external flowfield, but was only proven to be locally stable. A globally stable Lyapunov-based control design was given in [54].

This chapter proceeds as follows. Section 3.1 discusses circular formations, with both prescribed and non-prescribed centers, and coordinated encirclement in a known time-varying flowfield. In this section we use the unconstrained particle model (2.4). The constrained model is used in Section 3.2 to show that the previous results hold for a known spatially invariant and rotating flowfield.

3.1 Stabilization of a Circular Formation in a Known, Time-varying Flowfield

This section provides decentralized control laws that stabilize a circular formation in a time-varying flowfield. For now the turning-rate constraint is relaxed and it is assumed that the flow is known. Section 3.1.1 provides a control law for model (2.3) to stabilize a circular formation about an arbitrary point in a spatially nonuniform flowfield. In Section 3.1.2, a symmetry-breaking virtual particle is introduced that allows the formation center to be specified. The latter algorithm also enables the particles to follow a constant velocity target. (A method is presented to follow a maneuvering target in Chapter 6.) In Section 3.1.3 a circular-formation control law is provided that regulates the temporal spacing of the particles in a spatially uniform flowfield.

3.1.1 Circular Formation with an Arbitrary Center

A control law is developed that drives the particles into a circular formation about an arbitrary, fixed point. All of the particles in the circular formation travel in the same direction. In the case of a flow-free environment, setting u_k equal to a constant ω_0 will drive the particles about a fixed center point with radius $|\omega_0|^{-1}$. In model (2.3), the center of a circular trajectory is [54]

$$c_k \triangleq r_k + \omega_0^{-1} i \frac{\dot{r}_k}{|\dot{r}_k|} = r_k + \omega_0^{-1} i e^{i\gamma_k}. \tag{3.1}$$

By differentiating (3.1) with respect to time, a steering control ν_k is derived that drives a single particle around a circle in a time-varying flow. This gives

$$\dot{c}_k(t) = s_k(t)e^{i\gamma_k} - \omega_0^{-1}e^{i\gamma_k}\nu_k = (s_k(t) - \omega_0^{-1}\nu_k)e^{i\gamma_k}. \tag{3.2}$$

Equation (3.2) with $\nu_k = \omega_0 s_k(t)$ ensures $\dot{c}_k = 0$, which implies the center is fixed. Particle k will traverse a circle with constant radius $|\omega_0|^{-1} = |c_k(0) - r_k(0)|$.

Next a steering control is proposed that drives all particles to orbit the same center point in the same direction. Let $\boldsymbol{1} \triangleq (1, \ldots, 1)^T \in \mathbb{R}^N$. In a circular formation, $c_k = c_j$ for all pairs j and k, which implies the condition $P\boldsymbol{c} = 0$ [65], where P is the $N \times N$ projection matrix

$$P = \text{diag}\{\boldsymbol{1}\} - \frac{1}{N}\boldsymbol{1}\boldsymbol{1}^T. \tag{3.3}$$

This matrix is equivalent to the Laplacian matrix of an all-to-all communication topology [21]. (Since the intent of this chapter is to focus on the time-varying aspect of the flowfield, all-to-all communication is assumed even though it is possible to relax this constraint to a topology with limited communication [66].)

Following prior work, choose the Lyapunov function [65]

$$S(\boldsymbol{r}, \boldsymbol{\gamma}) \triangleq \frac{1}{2}\langle \boldsymbol{c}, P\boldsymbol{c} \rangle \tag{3.4}$$

where $\boldsymbol{r}$, $\boldsymbol{\gamma}$, and $\boldsymbol{c}$ are the vector representations of the particle's inertial positions, orientations and circular trajectory centers respectively. Note that S is positive

17

definite in the reduced space of relative centers. It is equal to zero only when $\boldsymbol{c} = c_0 \boldsymbol{1}$, for some $c_0 \in \mathbb{C}$. The time derivative of S along solutions of (2.4) is

$$\dot{S} = \sum_{k=1}^{N} \langle \dot{c}_k, P_k \boldsymbol{c} \rangle = \sum_{k=1}^{N} \langle e^{i\gamma_k}, P_k \boldsymbol{c} \rangle (s_k(t) - \omega_0^{-1} \nu_k), \qquad (3.5)$$

where P_k is the kth row of projection matrix P.

The following theorem extends [54, Theorem 3] to incorporate a time-varying flowfield.

Theorem 1. *Let $f_k(t) = f(r_k, t)$ such that $|f_k(t)| < 1$, $\forall\, k, t$. Choosing the control*

$$\nu_k = \omega_0(s_k(t) + K \langle P_k \boldsymbol{c}, e^{i\gamma_k} \rangle), \ K > 0, \omega_0 \neq 0, \qquad (3.6)$$

forces uniform convergence of solutions of model (2.4) to the set of a circular formations with radius $|\omega_0|^{-1}$ and direction determined by the sign of ω_0.

Proof. The potential $S(\boldsymbol{r}, \boldsymbol{\gamma})$ is radially unbounded and positive definite in the (complex) co-dimension one reduced space of relative centers. Under the control (3.6) the time derivative of S along solutions to (2.4) is

$$\dot{S} = -K \sum_{k=1}^{N} \langle P_k \boldsymbol{c}, e^{i\gamma_k} \rangle^2 \leq 0.$$

According to an invariance-like theorem for nonautonomous systems [31, Theorem

18

8.4], the solutions of (2.4) with control (3.6) converge to the set $\{\dot{S} = 0\}$ in which

$$\langle P_k \boldsymbol{c}, e^{i\gamma_k} \rangle = 0, \ \forall \, k. \tag{3.7}$$

In this set, control (3.6) evaluates to $\nu_k = \omega_0 s_k(t)$ and $\dot{c}_k = 0$, which implies each particle traverses a circle with a fixed center. Therefore, $P_k \boldsymbol{c}$ is constant and must be zero for (3.7) to hold. Since the null space of P is spanned by $\boldsymbol{1}$, then (3.7) is satisfied only when $P\boldsymbol{c} = 0$, which implies $c_k = c_j \ \forall \, k, j$. In the co-dimension one reduced space of relative centers $\dot{S} \leq -K \langle P_k \boldsymbol{c}, e^{i\gamma_k} \rangle^2 < 0$ for $k = 1, \ldots, N$ showing that S decreases over the interval $[t, t + \delta] \ \forall \, t \geq 0$, for some $\delta > 0$. This implies the set of circular formations with radius $|\omega_0|^{-1}$ is uniformly asymptotically stable [31, Theorem 8.5]. $\qquad \square$

Figure 3.1 illustrates Theorem 1 for a time-varying, spatially nonuniform flowfield. It shows the convergence of $N = 5$ particles to a circular formation whose center was determined by initial conditions. The flowfield, is generated by the periodic function $f_k = a(t)(\sin(2\pi \omega x_k - \varphi_0) + i \cos(2\pi \omega y_k - \varphi_0))$, where $a(t) = 0.75 \sin(10t)$, $\omega = 1$, and $\varphi_0 = 10$.

3.1.2 Circular Formation with a Prescribed Center

Under control (3.6) the center of the circular formation depends only on the flowfield and the initial conditions of the particles. By introducing a virtual particle (indexed by $k = 0$) and choosing initial conditions $r_0(0)$ and $\gamma_0(0)$ a center point for the formation is prescribed to be $c_0(0) = r_0(0) + i\omega_0^{-1} e^{i\gamma_0(0)}$. The virtual particle has

19

(a) $t = 200$ s $\qquad$ (b) $t = 400$ s $\qquad$ (c) $t = 600$ s
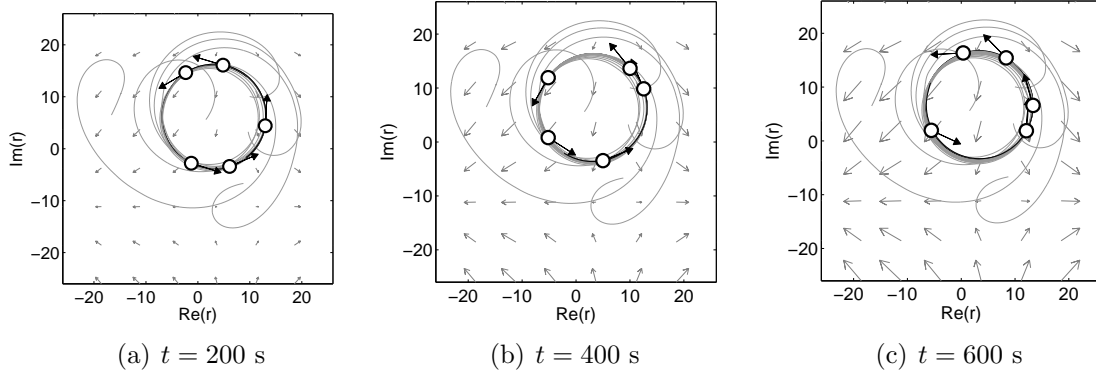
Figure 3.1: Stabilization of a circular formation with an arbitrary center in a time-varying, spatially nonuniform flowfield.

dynamics $r_0(t) = s_0(t)e^{i\gamma_0}$ and $\dot{\gamma}_0 = s_0(t)\omega_0$, which implies $c_0(t) = c_0(0)$ by equation (3.2). This makes possible applications such as encirclement of a moving target, where the formation needs to be directed to a specific location that may be moving with piecewise-constant velocity.

Consider the augmented potential $\tilde{S}(\boldsymbol{r}, \boldsymbol{\gamma}) = S(\boldsymbol{r}, \boldsymbol{\gamma}) + S_0(\boldsymbol{r}, \boldsymbol{\gamma})$ [66] where

$$S_0(\boldsymbol{r}, \boldsymbol{\gamma}) = \frac{1}{2} \sum_{k=1}^{N} a_{k0}|c_k - c_0|^2. \tag{3.8}$$

Value $a_{k0} = 1$ if particle k is informed of the reference center and $a_{k0} = 0$ otherwise. The time-derivative of (3.8) is

$$\dot{\tilde{S}} = \sum_{k=1}^{N} \left(\langle e^{i\gamma_k}, P_k \boldsymbol{c} \rangle + a_{k0} \langle e^{i\gamma_k}, c_k - c_0 \rangle \right) (s_k(t) - \omega_0^{-1} \nu_k). \tag{3.9}$$

The following theorem extends [54, Corollary 3] to incorporate a time-varying flowfield.

20

Theorem 2. *Let $f_k(t) = f(r_k, t)$ satisfy $|f_k(t)| < 1$, $\forall\, k, t$. Choosing the control*

$$\nu_k = \omega_0(s_k(t) + K(\langle e^{i\gamma_k}, P_k c\rangle + a_{k0}\langle e^{i\gamma_k}, c_k - c_0\rangle)),\ K > 0,\ \omega_0 \neq 0, \qquad (3.10)$$

where $a_{k0} = 1$ for at least one $k \in 1, \ldots, N$ and zero otherwise, forces uniform convergence of all solutions of the model (2.4) to the set of circular formations centered on c_0 with radius $|\omega_0|^{-1}$ and direction determined by the sign of ω_0.

Proof. The time-derivative of the augmented potential $\tilde{S}(r, \gamma)$ satisfies

$$\dot{\tilde{S}} = -K\sum_{k=1}^{N}(\langle e^{i\gamma_k}, P_k c\rangle + a_{k0}\langle e^{i\gamma_k}, c_k - c_0\rangle)^2 \leq 0.$$

By an invariance-like principle for nonautonomous systems [31, Theorem 8.4], solutions of (2.4) converge to the set $\{\dot{\tilde{S}} = 0\}$ in which

$$\langle e^{i\gamma_k}, P_k c\rangle + a_{k0}\langle e^{i\gamma_k}, c_k - c_0\rangle = 0 \ \forall\ k. \qquad (3.11)$$

If there exists a j such that $a_{j0} = 0$, then (3.11) reduces to $\langle e^{i\gamma_j}, P_j c\rangle$ and control (3.10) becomes $\nu_j = \omega_0 s_j(t)$. Following the proof of Theorem 1, equation (3.11) holds only when $c_k = c_j$ for all pairs k and j. For the informed particles where $a_{k0} = 1$, (3.11) becomes

$$\langle e^{i\gamma_k}, c_k - c_0\rangle = 0. \qquad (3.12)$$

This condition is satisfied only if $c_k = c_0$, ensuring that all particles will converge to a circular formation around the prescribed center c_0. The trivial case of $a_{k0} = 1$, $\forall\ k$

is addressed in [54, Corollary 1]. The rest of the proof follows from the proof of Theorem 1. □

The numerical results of this control are illustrated in Chapter 6.

3.1.3 Time-splay Circular Formation

In this section, a control algorithm is derived to stabilizes a circular formation in which the temporal spacing between particles is regulated. Because all particles are traveling at unit speed relative to the flowfield the spatial separation between particles may not be controllable. However, the temporal spacing between particles can be adjusted to ensure that any point along the vehicle's trajectory has a consistent revisit rate. A spatially uniform flowfield is assumed to be of the form $f(t) = \eta_0 e^{i\Omega t}$, in which the magnitude η_0 is constant and the direction $\xi(t) = \Omega t$ rotates at a constant rate Ω. (Such a flowfield arises in a reference frame fixed to a constant-speed target that turns at a constant rate.)

Equation (3.2) shows that $\nu_k = \omega_0 s_k(t)$ drives particle k in a fixed circle of radius $|\omega_0|^{-1}$. Consider the change of variables $\gamma_k' = \gamma_k - \Omega t$, which implies

$$\dot{\gamma}_k' = \dot{\gamma}_k - \Omega = \omega_0 s_k(t) - \Omega. \tag{3.13}$$

Using (2.15), the following expression for $s_k(t)$ is obtained, which depends on γ_k' instead of time:

$$s_k(t) = s(\gamma_k') = \eta_0 \cos \gamma_k' + \sqrt{(1 - \eta_0^2 \sin^2 \gamma_k')}. \tag{3.14}$$

For the ensuing calculations to be nonsingular, it is required that (3.13) not have a fixed point, as ensured by the following lemma.

Lemma 1. *Choosing*

$$|\omega_0| > \frac{\text{sgn}(\omega_0)\Omega}{(1 - |\eta_0|)} \quad \text{or} \quad |\omega_0| < \frac{\text{sgn}(\omega_0)\Omega}{(1 + |\eta_0|)} \tag{3.15}$$

ensures that (3.13) does not have a fixed point.

Proof. Requiring $\omega_0 s_k(t) - \Omega \neq 0$ implies

$$\min_{\gamma_k'} s(\gamma_k') > \frac{\Omega}{\omega_0} \tag{3.16}$$

or

$$\max_{\gamma_k'} s(\gamma_k') < \frac{\Omega}{\omega_0}. \tag{3.17}$$

The minimum of $s(\gamma_k')$ in (3.14) is $s(\gamma_k') = 1 - |\eta_0|$, which occurs at $\gamma_k' = \pi$ if $\eta_0 > 0$ and $\gamma_k' = 0$ if $\eta_0 < 0$. Substituting $s(\gamma_k') = 1 - |\eta_0|$ into (3.16) yields $|\omega_0| > \text{sgn}(\omega_0)\Omega/((1 - |\eta_0|))$. The maximum of $s(\gamma_k')$ in (3.14) is $s(\gamma_k') = 1 + |\eta_0|$ which occurs at $\gamma_k' = 0$ if $\eta_0 > 0$ and $\gamma_k' = \pi$ if $\eta_0 < 0$. Substituting $s(\gamma_k') = 1 + |\eta_0|$ into (3.17) yields $\text{sgn}(\omega_0)|\omega_0| < \Omega/((1 + |\eta_0|))$. Therefore, placing conditions (3.15) on $|\omega_0|$ ensures that (3.13) will not have a fixed point. $\square$

Integrating (3.13) by separation of variables yields

$$t = \int_0^{\gamma_k'(t)} \frac{d\gamma'}{\omega_0 s(\gamma') - \Omega}. \tag{3.18}$$

A time-phase variable is introduced to regulate the time separation of the N particles [54]. The time-phase for a time-varying, uniform flow $f(t) = \eta_0 e^{i\Omega t}$ is

$$\psi_k \triangleq \frac{2\pi}{T} \int_0^{\gamma'_k(t)} \frac{d\gamma'}{\omega_0 s(\gamma') - \Omega}, \tag{3.19}$$

where T, the period of a single revolution, is

$$T = \int_0^{2\pi} \frac{d\gamma'}{\omega_0 s(\gamma') - \Omega}. \tag{3.20}$$

The time-derivative of (3.19) is

$$\dot{\psi}_k = \frac{2\pi}{T} \frac{\nu_k - \Omega}{\omega_0 s_k(t) - \Omega}. \tag{3.21}$$

Choosing ω_0 to satisfy (3.15) ensures $\dot{\psi}_k$ is non-singular by Lemma 1. Note (3.21) implies that the control $\nu_k = \omega_0 s_k(t)$ yields a constant time-phase rate, $\dot{\psi}_k = 2\pi/T$. To stabilize a circular formation in which the relative time-phases are regulated, a phase potential is added to the Lyapunov function. The composite potential is [65]

$$V(\boldsymbol{r}, \boldsymbol{\gamma}) = S(\boldsymbol{r}, \boldsymbol{\gamma}) + \frac{T}{2\pi} U(\boldsymbol{\psi}). \tag{3.22}$$

The phase potential $U(\boldsymbol{\psi})$ is a smooth function satisfying the rotational symmetry property $U(\boldsymbol{\psi} + \psi_0 \boldsymbol{1}) = U(\boldsymbol{\psi})$, which implies [65]

$$\sum_{k=1}^N \frac{\partial U}{\partial \psi_k} = 0. \tag{3.23}$$

24

Using (3.21) and (3.23), gives the following time-derivative of the potential (3.22):

$$
\begin{aligned}
\dot{V} &= \sum_{k=1}^{N} \langle e^{i\gamma_k}, P_k \boldsymbol{c} \rangle (s_k(t) - \omega_0^{-1} \nu_k) + \frac{T}{2\pi} \frac{\partial U}{\partial \psi_k} \dot{\psi}_k \\
&= \sum_{k=1}^{N} \left(s_k(t) \langle e^{i\gamma_k}, P_k \boldsymbol{c} \rangle - \frac{\partial U}{\partial \psi_k} \frac{\omega_0 s_k(t)}{\omega_0 s_k(t) - \Omega} \right) \left(\frac{\omega_0 s_k(t) - \nu_k}{\omega_0 s_k(t)} \right). \quad (3.24)
\end{aligned}
$$

The following theorem extends [54, Theorem 5] to incorporate a spatially in-variant, time-varying flowfield.

Theorem 3. *Let $f(t) = \eta_0 e^{i\Omega t}$ be a spatially invariant flowfield satisfying the conditions $\Omega \in \mathbb{R}$ and $|\eta_0| < 1 \; \forall \, t$. Also, let $U(\psi)$ be a smooth, rotationally symmetric phase potential. Choosing the control*

$$
\nu_k = \omega_0 s_k(t) \left(1 + K \left(s_k(t) \langle e^{i\gamma_k}, P_k \boldsymbol{c} \rangle - \frac{\partial U}{\partial \psi_k} \frac{\omega_0 s_k(t)}{\omega_0 s_k(t) - \Omega} \right) \right), \; K > 0, \quad (3.25)
$$

where $\omega_0 \neq 0$ satisfies the constraint in Lemma 1, stabilizes a circular formation with radius $|\omega_0|^{-1}$ and direction determined by the sign of ω_0 in which the time-phase arrangement is a critical point of $U(\boldsymbol{\psi})$.

Proof. Using control (3.25) with potential (3.24) yields

$$
\begin{aligned}
\dot{V} &= -K \sum_{k=1}^{N} \left((s_k(t))^2 \langle e^{i\gamma_k}, P_k \boldsymbol{c} \rangle^2 - 2 \frac{\partial U}{\partial \psi_k} \frac{\omega_0 s_k(t)}{\omega_0 s_k(t) - \Omega} \langle e^{i\gamma_k}, P_k \boldsymbol{c} \rangle \right. \\
&\qquad \left. + \left(\frac{\partial U}{\partial \psi_k} \frac{\omega_0 s_k(t)}{\omega_0 s_k(t) - \Omega} \right)^2 \right) \qquad\qquad\qquad\qquad (3.26) \\
&= -K \sum_{k=1}^{N} \left(s_k(t) \langle e^{i\gamma_k}, P_k \boldsymbol{c} \rangle - \left(\frac{\partial U}{\partial \psi_k} \frac{\omega_0 s_k(t)}{\omega_0 s_k(t) - \Omega} \right) \right)^2 \leq 0 \qquad (3.27)
\end{aligned}
$$

By an invariance-like principle [31, Theorem 8.4], solutions of (2.4) converge to the set $\{\dot{V} = 0\}$ for which

$$
s_k(t) \langle e^{i\gamma_k}, P_k \boldsymbol{c} \rangle - \frac{\partial U}{\partial \psi_k} \frac{\omega_0 s_k(t)}{\omega_0 s_k(t) - \Omega} = 0, \qquad\qquad (3.28)
$$

for $k = 1, ..., N$. By (3.25), in this set, $\nu_k = \omega_0 s_k(t)$. Thus each particle progresses around a circle with a fixed center and radius $|\omega_0|^{-1}$. Also $\dot{\psi}_k = 2\pi/T$, which implies that $U(\boldsymbol{\psi})$ is constant (by (3.23)) and $\partial U/\partial \psi_k = 0 \; \forall \; k$. Constraint (3.28) reduces to

$$
\langle e^{i\gamma_k}, P_k \boldsymbol{c} \rangle = 0. \qquad\qquad (3.29)
$$

The rest of the proof follows the proof of Theorem 1. $\qquad\qquad\square$

Theorem 3 establishes convergence to a critical point of a rotationally symmetric potential $U(\boldsymbol{\psi})$. As an example consider a potential whose minimum corresponds to a time-splay formation [54], in which all of the relative time-phases between con-

(a) $t = 100$ s   (b) $t = 2000$ s   (c) Relative time-phases
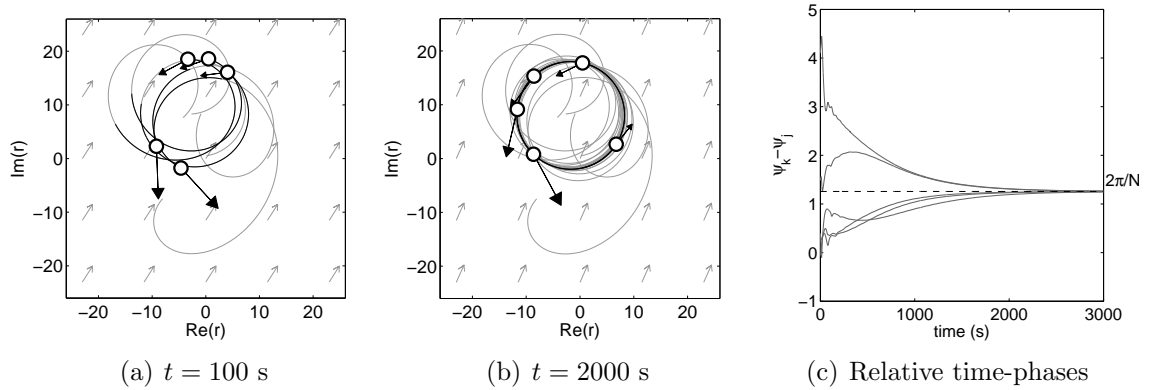
Figure 3.2: Stabilization of a time-splay formation with an arbitrary center in a time-varying, spatially uniform flowfield.

secutive particles around the formation are equal to $2\pi/N$:

$$U^{(M,N)}(\boldsymbol{\psi}) = \sum_{m=1}^{M} K_m U_m, \tag{3.30}$$

where

$$U_m(\boldsymbol{\psi}) = \frac{N}{2}|p_{m\psi}|^2, \; p_{m\psi} \triangleq \frac{1}{mN}\sum_{k=1}^{N} e^{im\psi_k},$$

renders the set of time-splay formations uniformly asymptotically stable, since they are the absolute minimum of $U^{(M,N)}$ when $M = N$. Note that $K_m > 0$ for $m = 1, \ldots, N-1$, and $K_N < 0$.

Figure 3.2 illustrates Theorem 3, showing $N = 5$ particles as they converge to a time-splay configuration for a time-varying, spatially uniform flowfield of the form $f(t) = \eta_0 e^{i\Omega t}$. Setting parameters $\eta_0 = 0.5$ and $\Omega = 0.01$ and choosing $\omega_0 = 0.1$ ensures that the constraint in Lemma 1 is satisfied. Figure 3.2(a) shows the particles as they initially converge to a circle. Figure 3.2(b) shows the particles at time $t = 2000$ after they have converged to a circular formation and an equal temporal

spacing. (The particles have unequal spatial separation because they travel slower when moving against the flowfield and faster when moving with the flowfield). The clustering of particles in the slower speed region ensures equal temporal spacing. Figure 3.2(c) shows convergence of the relative time-phases of sequential particles to $2\pi/N$, indicative of a time-splay configuration.

Introducing a virtual particle as in the previous section enables the center of the time-splay formation to be prescribed, as described in the following corollary.

Corollary 1. *Let $f(t) = \eta_0 e^{i\Omega t}$ be a spatially invariant flowfield satisfying the condition $|\eta_0| < 1$, $\forall$ t. Also, let $U(\psi)$ be a smooth, rotationally symmetric phase potential. Choosing the control*

$$\nu_k = \omega_0 s_k(t) \left(1 + K \left(s_k(t) \left(\langle e^{i\gamma_k}, P_k \boldsymbol{c} \rangle + a_{k0} \langle e^{i\gamma_k}, c_k - c_0 \rangle \right) - \frac{\partial U}{\partial \psi_k} \frac{\omega_0 s_k(t)}{\omega_0 s_k(t) - \Omega} \right) \right),$$

(3.31)

where $K > 0$ and $\omega_0 \neq 0$ satisfies the constraint in Lemma 1 and $a_{k0} = 1$ for at least one $k \in 1, \ldots, N$ and zero otherwise, stabilizes the set of circular formations centered on c_0 with radius $|\omega_0|^{-1}$ and direction determined by the sign of ω_0 in which the time-phase arrangement is a critical point of $U(\boldsymbol{\psi})$.

3.2 Circular Formation with a Bounded Turn-rate Constraint

Physical restrictions on an autonomous vehicle often constrain the turn-rate control that may be applied to a system. In UAVs, a turn-rate constraint can result from the aircraft's maximum bank angle [60]. In the previous sections this bound

was relaxed, allowing for potentially unlimited turn-rate control. In this section it is shown that the previous results are valid even when there is a turn-rate constraint; the constraint imposes a lower bound on the feasible radius of a circular formation in a flowfield.

In terms of the inertial speed $s_k(t)$ and orientation γ_k, model (2.1) is equivalent to

$$
\begin{aligned}
\dot{r}_k &= s_k(t)e^{i\gamma_k} \\
\dot{\gamma}_k &= \text{sat}(\nu_k; \nu_{max}),
\end{aligned}
\tag{3.32}
$$

where $\nu_{max} \triangleq \nu_k(u_{max})$ is a constraint on the steering control induced by the saturation on u_k. The relationship between ν_{max} and u_{max} is defined in Section 3.2.1 for a uniform, time-invariant flowfield and in Section 3.2.2 for a uniform, rotating flowfield.

3.2.1 Turn-Rate Constraint in a Uniform, Time-Invariant Flowfield

The following result establishes the maximum required turn rate for a particle to travel in a circle about a fixed center in a uniform, time-invariant flowfield. (Because of the flow the turn rate changes as the particle travels around the circle).

Lemma 2. *Consider circular motion with radius $|\omega_0|^{-1}$ of a particle in a steady flow $f_k = \beta \in \mathbb{R}$. The maximum required turn rate is*

$$
u_{max} \triangleq \max_{\gamma_k} u(\gamma_k) = |\omega_0|(1 + |\beta|)^2 > 0.
\tag{3.33}
$$

The maximum steering control is

$$\nu_{max} \triangleq \nu(u_{max}) = |\omega_0|(1 + |\beta|). \tag{3.34}$$

Proof. Consider the particle model (2.1). For a uniform, time-invariant flowfield β, the turn-rate control u_k can be determined from (2.16) to be

$$u_k = \frac{\nu_k}{1 - \beta s_k^{-1}(t)\cos\gamma_k}. \tag{3.35}$$

Given a circular control $\nu_k = \omega_0 s_k(t)$ with inertial speed

$$s_k(t) = \beta\cos\gamma_k + (1 - \beta^2\sin^2\gamma_k)^{1/2}, \tag{3.36}$$

the turn rate (3.35) is

$$u_k = u(\gamma_k) = \frac{\omega_0(\beta\cos\gamma_k + (1 - \beta^2\sin^2\gamma_k)^{1/2})^2}{(1 - \beta^2\sin^2\gamma_k)^{1/2}}. \tag{3.37}$$

The maximum turn rate

$$u_{max} = \max_{\gamma_k} u(\gamma_k) = |\omega_0|(1 + |\beta|)^2 \tag{3.38}$$

occurs when $\sin\gamma_k = 0$ and $\beta\cos\gamma_k = |\beta|$, i.e., $\gamma_k = 0$ if $\beta < 0$ or $\gamma_k = \pi$ if $\beta > 0$. Under these conditions (3.36) becomes $s_k(t) = 1 + |\beta|$. The controller ν_k is bounded through its relationship to u_{max}. Substituting $s_k(t) = 1 + |\beta|$ and (3.38) into (3.35)
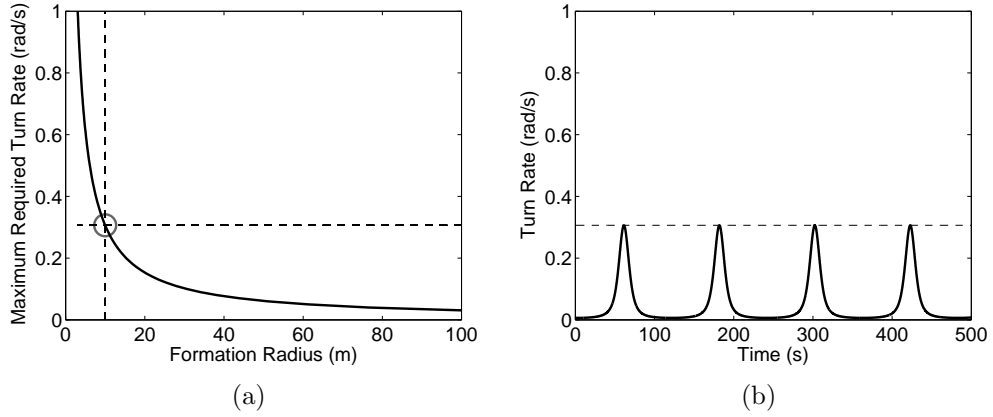
Figure 3.3: (a) Shows the maximum turn rate as a function of formation radius; (b) illustrates the turn rate as a function of time for a particle on a circle of radius $|\omega_0|^{-1} = 10$.

gives

$$\nu_{max} \triangleq \nu(u_{max}) = \frac{u_{max}}{(1 + |\beta|)^2} = |\omega_0|(1 + |\beta|). \tag{3.39}$$

$\square$

Figure 3.3(a) shows the maximum turn rate u_{max} as a function of the formation radius $|\omega_0|^{-1}$ for $\beta = 0.75$. (The maximum turn rate is the value necessary to maintain a circular formation of radius $|\omega_0|^{-1}$ given a spatially uniform flow β). Figure 3.3(b) plots the turn rate for a single particle initialized with a random position and velocity as it converges under control $\nu_k = \omega_0 s_k(t)$ to a circle of radius $|\omega_0|^{-1} = 10$. Note that the particle stays at or below the maximum turn rate as it maintains a circle of the prescribed radius. The following result shows that, even if the steering control is saturated the circular-formation control law is still justified.

Theorem 4. *Consider model (3.32) with $f_k = \beta \in \mathbb{R}$, $u_{max} > 0$, and $\nu_{max} =$*

$\nu_k(u_{max})$. If ω_0 satisfies

$$|\omega_0| < \frac{u_{max}}{(1 + |\beta|)^2},\tag{3.40}$$

then control (3.6) forces convergence of all particles to the set of circular formations with radius $|\omega_0|^{-1}$ and direction determined by the sign of ω_0.

Proof. Consider the Lyapunov function

$$V = \frac{1}{2}\langle \boldsymbol{c}, P\boldsymbol{c}\rangle.\tag{3.41}$$

The time derivative of V along solutions of (3.32) is

$$\dot{V} = \sum_{k=1}^{N}\langle P_k\boldsymbol{c}, e^{i\gamma_k}\rangle(s_k(t) - \omega_0^{-1}\nu_k).\tag{3.42}$$

Using control (3.6), observe that

$$\langle e^{i\gamma_k}, P_k\boldsymbol{c}\rangle = \frac{\nu_k - s_k(t)\omega_0}{K\omega_0},\tag{3.43}$$

which implies

$$\dot{V} = -\sum_{k=1}^{N}\frac{(s_k(t) - \omega_0^{-1}\nu_k)^2}{K} = -\frac{1}{K\omega_0^2}\sum_{k=1}^{N}\frac{(\omega_0 s_k(t) - \nu_k)^2}{K} \leq 0 \,\forall\, \nu_k.\tag{3.44}$$

When $-\nu_{max} \leq \nu_k \leq \nu_{max}$, $\dot{V} \leq 0$; otherwise, $\dot{V}$ is strictly less than zero. Applying the invariance principle, solutions of (2.4) converge to the largest invariant set for

which

$$\langle P_k \boldsymbol{c}, e^{i\gamma_k} \rangle = 0. \tag{3.45}$$

In this set, (3.6) evaluates to $\nu_k = s_k(t)\omega_0$ and $\dot{c}_k = 0$, which implies that the particles travels in a circle with a fixed center. $P_k \boldsymbol{c}$ is constant and must evaluate to zero. Because P is spanned by $\boldsymbol{1}$, this condition is only satisfied when $P\boldsymbol{c} = 0$, which implies $c_k = c_j \forall\, k, j$. The formation radius (3.40) satisfies (3.38) in Lemma 2, ensuring that the control will drive all particles to a set of asymptotically stable circular formations with radius $|\omega_0|^{-1}$. $\square$

By introducing a virtual particle, as was done in Theorem 2, one can similarly establish stabilization of a circular formation with a bounded turn rate at a prescribed center point.

Corollary 2. *Consider model (3.32) where $f_k = \beta \in \mathbb{R}$, $u_{max} > 0$, and $\nu_{max} = \nu_k(u_{max})$. If ω_0 satisfies*

$$|\omega_0| < \frac{u_{max}}{(1 + |\beta|)^2}, \tag{3.46}$$

then control (3.10) forces convergence to the set of circular formations centered on c_0 with radius $|\omega_0|^{-1}$ and direction determined by the sign of ω_0.

Figure 3.4 compares a system of particles that conform to the u_{max} constraint (3.38) with one that does not. By violating (3.38), the particles do not have the turn-rate control necessary to maintain a circular formation of the chosen radius. This is illustrated in Figure 3.4(a), using a bound of $u_{max} = 0.1$. The particles fail to maintain a circular radius of $|\omega_0|^{-1} = 10$, i.e., the solution does not converge to
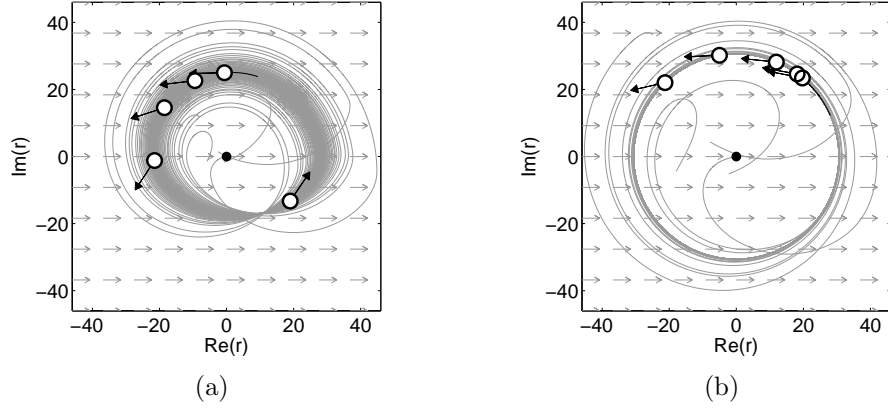
Figure 3.4: Effects of a bounded turning control, $u_{max} = 0.35$, in a spatially uniform flowfield with $\beta = 0.75$. (a) Circular formation is unobtainable with radius $|\omega_0|^{-1} = 10$. (b) Stable circular formation with radius $|\omega_0|^{-1} = 30.6$.

a circular formation. Figure 3.4(b) shows convergence to a circular formation with radius $|\omega_0|^{-1} = 30.6$, the smallest permissible radius for $u_{max} = 0.1$, according to Corollary 2.

3.2.2 Turn-Rate Constraint in a Uniform, Rotating Flowfield

This section shows that the previous results hold for a spatially invariant, rotating flow, $f(t) = \eta_0 e^{i\Omega t}$.

Lemma 3. *Consider circular motion of a particle with radius $|\omega_0|^{-1}$ and flowfield $f(t) = \eta_0 e^{i\Omega t}$. The maximum turn rate of the particle required to maintain a circular formation is*

$$u_{max} \triangleq \max_{\gamma_k} u(\gamma_k) = \begin{cases} |\omega_0|(1 + |\eta_0|)^2 - |\eta_0||\Omega| & \text{if } 2|\omega_0| > |\Omega|; \\ |\omega_0|(1 - |\eta_0|)^2 + |\eta_0||\Omega| & \text{if } 2|\omega_0| \leq |\Omega|. \end{cases} \tag{3.47}$$

The maximum steering control is

$$\nu_{max} \triangleq \nu(u_{max}) = \begin{cases} |\omega_0|(1 + |\eta_0|) & \text{if } 2|\omega_0| > |\Omega|; \\ |\omega_0|(1 - |\eta_0|) & \text{otherwise.} \end{cases} \qquad (3.48)$$

Proof. From (2.16), it is seen that the turn-rate control u_k for a particle with dynamics (2.1) in a rotating flowfield, $f(t) = \eta_0 e^{i\Omega t}$, is

$$u_k = u(\gamma_k') = \frac{s_k(t)\nu_k - \Omega\eta_0 \cos(\gamma_k')}{s_k(t) - \eta_0 \cos(\gamma_k')}, \qquad (3.49)$$

where $\gamma_k' = \gamma_k - \Omega t$. The inertial speed $s_k(t)$, is determined by (2.15):

$$s_k(t) = s(\gamma_k') = \eta_0 \cos(\gamma_k') + (1 - \eta_0^2 \sin(\gamma_k')^2)^{\frac{1}{2}}. \qquad (3.50)$$

Substituting the circular control $\nu_k = \omega_0 s_k(t)$ into (3.49) and finding the extrema with respect to γ_k' yields critical points at $\gamma_k' = 0$ and $\gamma_k' = \pi$, which implies

$$u_k(0) = \omega_0(1 + \eta_0)^2 - \eta_0\Omega \qquad (3.51)$$

and

$$u_k(\pi) = \omega_0(1 - \eta_0)^2 + \eta_0\Omega. \qquad (3.52)$$

Either (3.51) or (3.52) is a maximum point depending on the values of η_0, Ω and ω_0. If $\eta_0 > 0$ then $u_k(0) > u_k(\pi)$ when $2\omega_0 > \Omega$. If $\eta_0 < 0$ then $u_k(0) > u_k(\pi)$ when $2\omega_0 < \Omega$ leading to (3.47). Under these conditions, (3.50) becomes $s_k(t) = 1 \pm |\eta|$

and substituting $s_k(t)$ and (3.47) into (3.49) gives (3.48). $\qquad\square$

Theorem 5. *Consider model (3.32) with $f(t) = \eta_0 e^{i\Omega t}$, $|\eta_0| < 1 \; \forall \; t$, and $u_{max} > 0$. If ω_0 satisfies*

$$\begin{aligned}
|\omega_0| &< (u_{max} + |\eta_0||\Omega|)/(1 + |\eta_0|)^2 \quad \text{if} \;\; 2|\omega_0| > |\Omega|; \\
|\omega_0| &< (u_{max} - |\eta_0||\Omega|)/(1 - |\eta_0|)^2 \quad \text{if} \;\; 2|\omega_0| \leq |\Omega|.
\end{aligned} \tag{3.53}$$

then the control (3.6) with ν_{max} given by (3.48) forces uniform convergence of solutions to model (3.32) to the set of circular formations with radius $|\omega_0|^{-1}$ and direction determined by the sign of ω_0.

The proof of Theorem 5 follows the proof of Theorem 4. Since $f(t)$ is time-varying, uniform asymptotic stability is established by the invariance-like principle as in Theorem 1. The following theorem shows that stabilization of a time-splay formation is possible even with a bounded turn rate, thereby extending Theorem 3.

Theorem 6. *Consider model (3.32) with the spatially invariant, rotating flowfield $f = \eta_0 e^{i\Omega t}$ and $|\eta_0| < 1 \; \forall \; t$. Also, let $U(\psi)$ be a smooth, rotationally symmetric phase potential. With ω_0 such that it satisfies both the constraint in Lemma 1 and*

$$\begin{aligned}
|\omega_0| &< (u_{max} + |\eta_0||\Omega|)/(1 + |\eta_0|)^2 \quad \text{if} \;\; 2|\omega_0| > |\Omega|; \\
|\omega_0| &< (u_{max} - |\eta_0||\Omega|)/(1 - |\eta_0|)^2 \quad \text{if} \;\; 2|\omega_0| \leq |\Omega|.
\end{aligned} \tag{3.54}$$

The control (3.25) and ν_{max} given by (3.48) forces uniform convergence of solutions to the model (3.32) to the set of circular formations with radius $|\omega_0|^{-1}$ and direction determined by the sign of ω_0.

Proof. Using the control (3.25), observe that

$$\frac{\nu_k - \omega_0 s_k(t)}{K \omega_0 s_k(t)} = s_k(t) \langle e^{i\gamma_k}, P_k c \rangle - \frac{\partial U}{\partial \psi_k} \frac{\omega_0 s_k(t)}{\omega_0 s_k(t) - \Omega}. \tag{3.55}$$

Using the Lyapunov function (3.22) substitute (3.55) into (3.24) to obtain

$$\dot{V} = \frac{1}{K \omega_0^2} \sum_{k=1}^{N} \frac{(\nu_k - \omega_0 s_k(t))^2}{(s_k(t))^2} \leq 0 \; \forall \; \nu_k. \tag{3.56}$$

$\dot{V}$ is strictly less than zero except when $-\nu_{max} \leq \nu_k \leq \nu_{max}$. In this interval $\dot{V} \leq 0$.

This case is covered by Theorem 3. The rest of the proof follows from Lemma 3 and

the proof of Theorem 3. □

Chapter 4

Motion Coordination in an Estimated Uniform Flowfield

This chapter provides cooperative control algorithms which operate in an unknown, uniform flowfield. Each vehicle individually estimates the flow using an observer-based methodology, which requires only noisy position measurements of the vehicle.

Many approaches exist for estimation of unknown, uniform flowfields. Petrich, et al. mapped a uniform flowfield with an added singular point to improve navigation of shallow water underwater autonomous vehicles. They parameterize the flowfield and use only a sparse set of GPS measurements in the estimation algorithm. All vehicle measurements were shared at a centralized node [57]. Another centralized approach given in [15] used information automatically broadcast by airplanes. The estimation fit a circle to north and east components of ground speeds taken from multiple airplanes with diverse headings but identical airspeed. The circle offset gives an estimate of the direction and magnitude of the flow. Similar approaches are given for a single plane which uses multiple measurements throughout the flight to determine the longitudinal component [13] and the 3D estimate [56] of the wind. Langelaan, et al. computed a 3D wind estimate and the wind acceleration using sensors typically found on a small UAV [36].

Also for a single vehicle [37] uses Gaussian process regression to create a global

map of the wind field based upon local observations. The wind field consisted of a static field with added thermal bubbles. Using a cost function the vehicle then balances exploration, improving the map estimate, with exploitation, using the wind to gain energy for the vehicle.

In the relative frame between the vehicles and circle center, a uniform flowfield is equivalent to a formation center moving in the opposite direction. Methods used to estimate the constant velocity of a target can equivalently be used to estimate a uniform flowfield. Summers et al. account for a constant-velocity moving target using adaptive estimates to drive cooperative vehicles in a loiter circle [70]. Burger and Pettersen enable curved trajectory following of surface vehicles using a conditional integrator to eliminate constant disturbances for vehicle formations [5].

This chapter proceeds as follows. Section 4.1 and 4.2 present methods to stabilize circular formations with an arbitrary or prescribed center point in an unknown, uniform flowfield. In Section 4.3 a time-splay formation is stabilized in a uniform, rotating flow. In these sections it is assumed that each particle knows its measured position, r_k, and orientation, θ_k, although a dynamic estimate of position, $\hat{r}_k$, is used to estimate the flow. In Section 4.4 we relax the assumption that we know the exact position and use only a noisy measurement.

Given an estimated flow, $\hat{f}_k(t) = \hat{f}(t, r_k)$, the estimated inertial velocity obeys

$$
\begin{aligned}
\dot{\hat{r}}_k &= \hat{s}_k(t)e^{i\hat{\gamma}_k} \\
\dot{\hat{\gamma}}_k &= \nu_k,
\end{aligned}
\tag{4.1}
$$

39

where $\hat{s}_k(t)$ and $\hat{\gamma}_k$ are the magnitude and phase, respectively, of the estimated inertial velocity for particle k.

4.1 Stabilization of Circular Formations with an Arbitrary Center

In this section a control law is developed to drive particles in a circular formation about an arbitrary, fixed point in the presence of an estimated, uniform, time-invariant flowfield. The control law works by dynamically estimating the flow and using the estimate in the control law.

Let $z_{1,k} = \hat{r}_k - r_k$ and $z_{2,k} = \hat{f}_k - f_k$ denote the estimation errors for particle k. Consider the estimator dynamics

$$
\begin{aligned}
\dot{\hat{r}}_k &= e^{i\theta_k} + \hat{f}_k - K_1(\hat{r}_k - r_k) \\
\dot{\hat{f}}_k &= -K_2(\hat{r}_k - r_k).
\end{aligned}
\tag{4.2}
$$

This yields

$$
\begin{aligned}
\dot{z}_{1,k} &= e^{i\theta_k} + \hat{f}_k - K_1(\hat{r}_k - r_k) - e^{i\theta_k} - f_k = -K_1 z_{1,k} + z_{2,k} \\
\dot{z}_{2,k} &= -K_2(\hat{r}_k - r_k) = -K_2 z_{1,k}.
\end{aligned}
$$

In matrix form, the estimator dynamics for particle k are

$$
\begin{bmatrix} \dot{z}_{1,k} \\ \dot{z}_{2,k} \end{bmatrix} = \underbrace{\begin{bmatrix} -K_1 & 1 \\ -K_2 & 0 \end{bmatrix}}_{\triangleq A} \begin{bmatrix} z_{1,k} \\ z_{2,k} \end{bmatrix}.
\tag{4.3}
$$

Lemma 4. *Choosing gains $K_2 > 0$ and $K_1 = 2\sqrt{K_2} > 0$ in the error dynamics (4.3) exponentially stabilizes the origin $z_{1,k} = z_{2,k} = 0 \, \forall \, k$.*

Proof. The eigenvalues of A are $\lambda = (-K_1 \pm \sqrt{K_1^2 - 4K_2})/2$. Choosing $K_1 = 2\sqrt{K_2}$ results in $\lambda = -K_1$ with multiplicity two. $\square$

The following is a result of Lemma 4.

Lemma 5. *The matrix A defined in (4.3) is negative definite and the quadratic form*

$$Q_k(A) \;=\; \begin{bmatrix} z_{1,k} & z_{2,k} \end{bmatrix} \begin{bmatrix} -K_1 & 1 \\ -K_2 & 0 \end{bmatrix} \begin{bmatrix} z_{1,k} \\ z_{2,k} \end{bmatrix} \tag{4.4}$$

$$= \; -K_1 z_{1,k}^2 - K_2 z_{1,k} z_{2,k} + z_{1,k} z_{2,k} \leq 0 \tag{4.5}$$

is equal to zero only when $z_{1,k} = z_{2,k} = 0$ for $k \in \{1, \ldots, N\}$.

Let $\hat{c}_k$ be the estimated center,

$$\hat{c}_k = \hat{r}_k + \omega_0^{-1} i e^{i \hat{\gamma}_k}. \tag{4.6}$$

and consider the candidate Lyapunov function

$$\hat{S}(\hat{\boldsymbol{r}}, \hat{\boldsymbol{\gamma}}) \triangleq \frac{1}{2} \langle \hat{\boldsymbol{c}}, P\hat{\boldsymbol{c}} \rangle + \frac{1}{2} \left(||\boldsymbol{z}_1||^2 + ||\boldsymbol{z}_2||^2 \right), \tag{4.7}$$

where $\boldsymbol{z}_1 = [z_{1,1}, z_{1,2}, ..., z_{1,N}]^T$, $\boldsymbol{z}_2 = [z_{2,1}, z_{2,2}, ..., z_{2,N}]^T$ and $\hat{\boldsymbol{c}}$ is the vector of center points defined by (4.6). $\hat{S}$ is equal to zero when $\hat{\boldsymbol{c}} = c_0 \boldsymbol{1}$, $c_0 \in \mathbb{C}$, and all estimation

errors are zero. The time derivative of $\hat{S}$ along solutions of (4.1) and (4.3) is

$$
\begin{aligned}
\dot{\hat{S}} &= \sum_{k=1}^{N} (\langle \dot{\hat{c}}_k, P_k \hat{\boldsymbol{c}} \rangle + \dot{z}_{1,k} z_{1,k} + \dot{z}_{2,k} z_{2,k}) \\
&= \sum_{k=1}^{N} \left[\langle e^{i\hat{\gamma}_k}, P_k \hat{\boldsymbol{c}} \rangle (\hat{s}_k(t) - \omega_0^{-1} \nu_k) - \underbrace{z_{1,k}(K_1 z_{1,k} - z_{2,k}) - z_{2,k}(K_2 z_{1,k})}_{=Q_k(A)} \right] \quad (4.8)
\end{aligned}
$$

The following theorem extends Theorem 1 to the case of an estimated, uniform, time-invariant flowfield.

Theorem 7. *Let $f_k(t) = \beta \in \mathbb{R}$, where $|\beta| < 1$, be an unknown time-invariant flowfield. Also, let $\hat{r}_k$ and $\hat{f}_k$ evolve according to (4.2) with $K_2 > 0$ and $K_1 = 2\sqrt{K_2}$. Choosing the control*

$$
\nu_k = \omega_0(\hat{s}_k(t) + K \langle P_k \hat{\boldsymbol{c}}, e^{i\hat{\gamma}_k} \rangle), \quad K > 0, \quad (4.9)
$$

forces convergence of solutions of model (4.1) to the set of circular formations with radius $|\omega_0|^{-1}$ and direction determined by the sign of ω_0.

Proof. Substituting (4.9) into (4.8) shows that the time-derivative of the potential $\hat{S}(\hat{\boldsymbol{r}}, \hat{\boldsymbol{\gamma}})$ satisfies

$$
\dot{\hat{S}} = \sum_{k=1}^{N} \left(-K \langle P_k \hat{\boldsymbol{c}}, e^{i\hat{\gamma}_k} \rangle^2 + Q_k(A) \right) \leq 0. \quad (4.10)
$$

Using the invariance principle, all of the solutions of (2.4) with controller (4.9)

42

converge to the largest invariant set where

$$- K \langle P_k \hat{\boldsymbol{c}}, e^{i\hat{\gamma}_k} \rangle^2 + Q_k(A) = 0, \ \forall \, k. \tag{4.11}$$

By Lemma 5 condition (4.11) is satisfied only when both $Q_k(A) = 0$ and $\langle P_k \hat{\boldsymbol{c}}, e^{i\hat{\gamma}_k} \rangle = 0$ independently. $Q_k(A) = 0$ implies that estimated values $\hat{r}_k$ and $\hat{f}_k$ equal the measured values, r_k and f_k. Values $\hat{\gamma}_k$ and $\hat{s}_k(t)$ are functions of $\hat{f}_k$ and θ_k. This implies that $\hat{\gamma}_k$ and $\hat{s}_k(t)$ approach their measured values and, by (4.6), $\hat{c}_k$ converges to c_k. The condition, $\langle P_k \hat{\boldsymbol{c}}, e^{i\hat{\gamma}_k} \rangle = 0$ is satisfied for all k only when $P_k \hat{\boldsymbol{c}}$ is constant and equal to zero. Since the null space of P is spanned by $\boldsymbol{1}$ this implies $\hat{c}_k = \hat{c}_j \ \forall \, k, j$. In this set, control (4.9) evaluates to $\nu_k = \omega_0 \hat{s}_k(t)$ and $\dot{\hat{c}}_k = 0$ which implies that each particle converges to circular motion around the same fixed center. $\square$

4.2 Stabilization of Circular Formations with a Prescribed Center

Under the control (4.9) the center of the circular formation depends only on the initial conditions of the particles and the flowfield. As with the case of the known flowfield, introducing a symmetry-breaking virtual particle (indexed by $k = 0$) will prescribe a center point for the formation. Consider the augmented potential $\tilde{S}(\hat{\boldsymbol{r}}, \hat{\boldsymbol{\gamma}}) = \hat{S}(\hat{\boldsymbol{r}}, \hat{\boldsymbol{\gamma}}) + \hat{S}_0(\hat{\boldsymbol{r}}, \hat{\boldsymbol{\gamma}})$, where

$$\hat{S}_0(\hat{\boldsymbol{r}}, \hat{\boldsymbol{\gamma}}) = \frac{1}{2} \sum_{j=1}^{N} a_{j0} |\hat{c}_j - c_0|^2 \tag{4.12}$$

and $\hat{c}_k$ is defined by (4.6). Taking the time-derivative of (4.12) along solutions of (4.1) and (4.3) gives

$$\dot{S} = \sum_{j=1}^{N} \left[\left(\langle e^{i\hat{\gamma}_j}, P_j \hat{c} \rangle + a_{j0} \langle e^{i\hat{\gamma}_j}, \hat{c}_j - c_0 \rangle \right) \left(\hat{s}_j(t) - \omega_0^{-1} \nu_j \right) \right.$$
$$\left. + \underbrace{z_{1,j}(-K_1 z_{1,j} + z_{2,j}) + z_{2,j}(-K_2 z_{1,j})}_{=Q_j(A)} \right]. \tag{4.13}$$

Theorem 8. *Let $f_k(t) = \beta \in \mathbb{R}$, where $|\beta| < 1$, be an unknown time-invariant flow. Also, let $\hat{r}_k$ and $\hat{f}_k$ evolve according to (4.2) with $K_2 > 0$ and $K_1 = 2\sqrt{K_2}$. Choosing the control*

$$\nu_k = \omega_0 (\hat{s}_k(t) + K(\langle e^{i\hat{\gamma}_k}, P_k \hat{c} \rangle + a_{k0} \langle e^{i\hat{\gamma}_k}, \hat{c}_k - c_0 \rangle)), \quad K > 0, \tag{4.14}$$

forces convergence of solutions of model (4.1) to the set of circular formation centered at c_0 with radius $|\omega_0|^{-1}$ and direction determined by the sign of ω_0.

Proof. Substituting the controller (4.14) into (4.13) shows that the time-derivative of the augmented potential $\tilde{S}(\hat{r}, \hat{\gamma})$ satisfies

$$\dot{S} = \sum_{j=1}^{N} \left((-K \langle e^{i\hat{\gamma}_j}, P_j \hat{c} \rangle + a_{j0} \langle e^{i\hat{\gamma}_j}, \hat{c}_j - c_0 \rangle)^2 + Q_j(A) \right) \leq 0.$$

According to the invariance principle, all solutions of (2.4) with controller (4.14) converge to the largest invariant set where

$$\langle P_j \hat{c}, e^{i\hat{\gamma}_j} \rangle^2 + a_{j0} \langle e^{i\hat{\gamma}_j}, \hat{c}_j - c_0 \rangle + Q_k(A) = 0, \ \forall \ j. \tag{4.15}$$

(a) $t = 20$ s   (b) $t = 1000$ s   (c) Error dynamics, $k = 3$
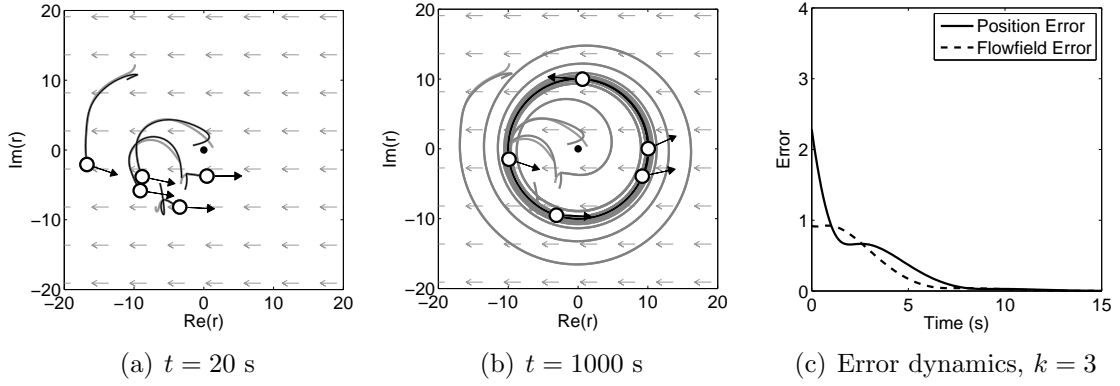
Figure 4.1: Stabilization of circular formation in uniform flowfield $f = -0.8$ with a prescribed center point $c_0 = 0$.

By Lemma 5, $Q_k(A) = 0$ only when the estimated $\hat{r}_k$ and $\hat{f}_k$ values have converged to their corresponding measured values. The convergence of these estimated values also implies that $\hat{s}_k(t)$, $\hat{\gamma}_k$ and $\hat{c}_k$ converge to their measured values. The remaining terms in (4.15) become $\langle P_j \boldsymbol{c}, e^{i\gamma_j} \rangle^2 + a_{j0} \langle e^{i\gamma_j}, c_j - c_0 \rangle$ and must be equal to zero independently of $Q_k(A)$. Following the proof of Theorem 2 this occurs only when $c_k = c_0$ and the controller (4.14) becomes $\nu_k = s_k(t)\omega_0$. Therefore, all of the particles will converge to the set of circular formations with radius $|\omega_0|^{-1}$ and center c_0. $\square$

Figure 4.1 illustrates Theorem 8 with estimator gains $K_2 = 0.2$ and $K_1 = 2\sqrt{K_2} = 0.894$ and a uniform flowfield $f = -0.8$. Figures 4.1(a) and 4.1(b) show tracks of the estimated (darker track) and actual (lighter track) particle positions at 20 and 1000 seconds respectively, as they converge to a circular formation about the prescribed center point, $c_0 = 0$. Figure 4.1(c) shows convergence to zero of estimator errors in the position and the flow for particle $k = 3$.

4.3 Time-splay Formation with a Rotating Flowfield

We now derive a control law to stabilize particles to a time-splay formation in an estimated, spatially invariant, rotating flowfield. (A rotating flowfield is defined to be a uniform flowfield whose direction is rotating in time.) Without speed control it may not be possible to regulate the spatial separation of particles, but it is possible to regulate the temporal separation in an estimated flowfield as shown next.

Given a uniform time-varying flowfield $f = \eta_0 e^{i\Omega t}$, choose $z_{1,k} = \hat{r}_k - r_k$ and $z_{2,k} = \hat{f}_k - f_k$. The rotational rate, Ω, is assumed to be known; the flow speed, η_0, and initial orientation are unknown. Consider the estimator dynamics

$$
\begin{aligned}
\dot{\hat{r}}_k &= e^{i\theta_k} + \hat{f}_k - K_1(\hat{r}_k - r_k) \\
\dot{\hat{f}}_k &= -K_2(\hat{r}_k - r_k) + \Omega i \hat{f}_k.
\end{aligned}
\tag{4.16}
$$

Taking the derivative of the error and plugging in (4.16) yields

$$
\begin{aligned}
\dot{z}_{1,k} &= e^{i\theta_k} + \hat{f}_k - K_1(\hat{r}_k - r_k) - e^{i\theta_k} - f_k = -K_1 z_{1,k} + z_{2,k} \\
\dot{z}_{2,k} &= -K_2 z_{1,k} + \Omega i z_{2,k}.
\end{aligned}
$$

The estimator dynamics for particle k are

$$
\begin{bmatrix} \dot{z}_{1,k} \\ \dot{z}_{2,k} \end{bmatrix} = \underbrace{\begin{bmatrix} -K_1 & 1 \\ -K_2 & \Omega i \end{bmatrix}}_{\triangleq B} \begin{bmatrix} z_{1,k} \\ z_{2,k} \end{bmatrix}.
\tag{4.17}
$$

Lemma 6. *Choosing gains $K_1 > |\Omega|$ and $K_2 = (K_1^2 - \Omega^2)/4$ in the error dynamics (4.17) exponentially stabilizes the origin $z_{1,k} = z_{2,k} = 0$ for $k = [1, \ldots, N]$.*

Proof. The eigenvalues of B are

$$
\begin{aligned}
\lambda &= \frac{-(K_1 - \Omega i) \pm \sqrt{(K_1 - \Omega i)^2 - 4(-K_1\Omega i + K_2)}}{2} \\
&= \frac{-K_1 + \Omega i \pm \sqrt{(K_1^2 - \Omega^2 - 4K_2) + (2K_1\Omega)i}}{2}.
\end{aligned}
$$

The real part is given by

$$
\mathrm{Re}(\lambda) = \frac{-K_1 \pm \mathrm{Re}\left(\sqrt{(K_1^2 - \Omega^2 - 4K_2) + (2K_1\Omega)i}\right)}{2}. \tag{4.18}
$$

To evaluate the real part of the square root term, which contains a complex number, observe that

$$
\mathrm{Re}(\sqrt{a + bi}) = \mathrm{Re}(\sqrt{\rho e^{\varphi i}}) = \sqrt{\rho} \cos \frac{\varphi}{2},
$$

with $\rho = \sqrt{a^2 + b^2}$ and $\cos \varphi = a/\rho$. Using the half-angle formula for $\cos \varphi = \sqrt{(1 + \cos 2\varphi)/2}$, the real part of square root becomes

$$
\mathrm{Re}(\sqrt{a + bi}) = \sqrt{\rho}\sqrt{\left(\frac{1 + \frac{a}{\rho}}{2}\right)} = \sqrt{\frac{\rho + a}{2}}. \tag{4.19}
$$

Evaluating (4.19) for (4.18) yields

$$
\mathrm{Re}(\lambda) = \frac{-K_1}{2} \pm \frac{\sqrt{\sqrt{(K_1^2 - \Omega^2 - 4K_2)^2 + 4K_1^2\Omega^2} + (K_1^2 - \Omega^2 - 4K_2)}}{2\sqrt{2}},
$$

47

which is the real portion of the eigenvalues of matrix B.

Letting $K_1 > |\Omega|$ and $K_2 = (K_1^2 - \Omega^2)/4$ results in $\mathrm{Re}(\lambda) = (-K_1 \pm \sqrt{K_1 \Omega})/2$.

$K_1 > |\Omega|$, which implies $\mathrm{Re}(\lambda) < 0$. $\qquad\qquad\qquad\qquad\qquad\qquad\qquad\qquad\square$

The following result is a consequence of Lemma 6

Lemma 7. *Matrix B defined in (4.17) is negative definite and the quadratic form*

$$
Q_k(B) \triangleq \begin{bmatrix} z_{1,k} & z_{2,k} \end{bmatrix} \begin{bmatrix} -K_1 & 1 \\ -K_2 & \Omega i \end{bmatrix} \begin{bmatrix} z_{1,k} \\ z_{2,k} \end{bmatrix} = -K_1 z_{1,k}^2 - K_2 z_{1,k} z_{2,k} + z_{1,k} z_{2,k} + \Omega i z_{2,k}^2 \leq 0
$$

(4.20)

is only equal to zero when $z_{1,k} = z_{2,k} = 0 \ \forall \ k$.

The estimator dynamics (4.17) are used to stabilize a time-splay formation for a flowfield with known rotation rate $\Omega(t)$. Consider the Lyapunov function

$$
\hat{V}(\hat{\boldsymbol{r}}, \hat{\boldsymbol{\gamma}}) = \frac{1}{2}\langle \hat{\boldsymbol{c}}, P\hat{\boldsymbol{c}} \rangle + \frac{T}{2\pi}U(\hat{\boldsymbol{\psi}}) + \frac{1}{2}\left(||\boldsymbol{z}_1||^2 + ||\boldsymbol{z}_2||^2\right),
$$

(4.21)

where $\hat{\boldsymbol{c}}$ is the vector of estimated center points defined by (4.6). Taking the time-derivative along solutions of (4.1) and (4.17) yields

$$
\dot{\hat{V}} = \sum_{k=1}^{N}\left[\left(\hat{s}_k(t)\langle e^{i\hat{\gamma}_k}, P_k\hat{\boldsymbol{c}}\rangle - \frac{\partial U}{\partial \hat{\psi}_k}\frac{\omega_0 \hat{s}_k(t)}{\omega_0 \hat{s}_k(t) - \Omega}\right)\left(\frac{\omega_0 \hat{s}_k(t) - \nu_k}{\omega_0 \hat{s}_k(t)}\right) + \right.
$$

$$
\left. \underbrace{z_{1,k}(-K_1 z_{1,k} + z_{2,k}) + z_{2,k}(-K_2 z_{1,k} + \Omega i z_{2,k})}_{=Q_k(B)}\right].
$$

(4.22)

The following result extends Theorem 3 to incorporate an estimated, spatially invariant, rotating flow.

Theorem 9. *Let $f(t) = \eta_0 e^{i\Omega t}$ be an unknown spatially invariant flowfield satisfying the condition $|\eta_0| < 1$, $\forall\, t$. Also, let $U(\hat{\boldsymbol{\psi}})$ be a smooth, rotationally symmetric phase potential. Let $\hat{r}_k$ and $\hat{f}_k$ evolve according to (4.16) with $K_1 > |\Omega|$ and $K_2 = (K_1^2 - \Omega^2)/4$. Choosing the control*

$$\nu_k = \omega_0 \hat{s}_k(t) \left(1 + K\left(\hat{s}_k(t)\langle e^{i\hat{\gamma}_k}, P_k \hat{\boldsymbol{c}}\rangle - \frac{\partial U}{\partial \hat{\psi}_k} \frac{\omega_0 \hat{s}_k(t)}{\omega_0 \hat{s}_k(t) - \Omega}\right)\right), \; K > 0, \quad (4.23)$$

where $\omega_0 \neq 0$ satisfies the constraint in Lemma 1, stabilizes the set of circular formations with radius $|\omega_0|^{-1}$ and direction determined by the sign of ω_0 in which the time-phase arrangement is a critical point of $U(\hat{\boldsymbol{\psi}})$.

Proof. Using control (4.23) with potential (4.22) yields

$$\dot{V} = \sum_{k=1}^{N} \left(-K\left(\hat{s}_k(t)\langle e^{i\hat{\gamma}_k}, P_k \hat{\boldsymbol{c}}\rangle - \left(\frac{\partial U}{\partial \hat{\psi}_k} \frac{\omega_0 \hat{s}_k(t)}{\omega_0 \hat{s}_k(t) - \Omega}\right)\right)^2 + Q_k(B)\right) \leq 0.$$

By an invariance-like principle [31, Theorem 8.4], solutions of (2.4) converge to the set $\{\dot{V} = 0\}$ for which

$$-K\left(\hat{s}_k(t)\langle e^{i\hat{\gamma}_k}, P_k \hat{\boldsymbol{c}}\rangle - \frac{\partial U}{\partial \hat{\psi}_k} \frac{\omega_0 \hat{s}_k(t)}{\omega_0 \hat{s}_k(t) - \Omega}\right)^2 + Q_k(B) = 0, \; \forall\, k. \quad (4.24)$$

According to Lemma 7, both terms in (4.24) must equal zero and $Q_k(B) = 0$ only when the estimated $\hat{r}_k$ and $\hat{f}_k$ values have converged to their corresponding measured values. The convergence of these estimated values along with the known value θ_k

(a) $t = 20$ s   (b) $t = 3000$ s   (c) Error Dynamics, $k = 3$
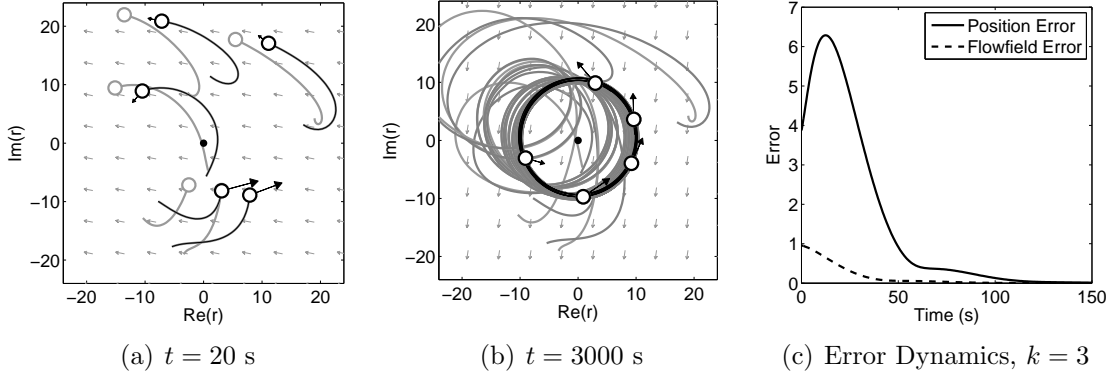
Figure 4.2: Stabilization of a circular time-splay formation centered at $c_0 = 0$ in an estimated rotating flowfield, $f(t) = \eta_0 e^{i\Omega t}$, with $\eta_0 = 0.5$ and $\Omega = -0.01$.

also implies that $\hat{s}_k(t)$, $\hat{\gamma}_k$ and $\hat{c}_k$ converge to their measured values. The rest of the proof follows from the proof of Theorem 3 and 7. $\square$

Figure 4.2 illustrates Theorem 9. The simulation uses estimator gains $K_1 = 0.1$ and $K_2 = (K_1^2 - \Omega^2)/4$. The rotating flowfield parameters are $\eta = 0.5$, $\Omega = -0.01$, and $\omega_0 = .1$ which satisfies Lemma 1. Figures 4.2(a) and 4.2(b) show tracks of the estimated (darker track) and actual (lighter track) particle positions at 20 and 3000 seconds respectively as they converge to a time-splay formation about the prescribed center point, $c_0 = 0$. Figure 4.2(c) shows convergence of the estimator errors to zero for a single particle, $k = 3$. The initial conditions for all particles are set randomly. In this simulation the initial estimated flowfield started in the opposite direction as the actual flowfield causing the measured and estimated positions to temporarily diverge as seen by the peak in Figure 4.2(c).

4.4 Flowfield Estimation Using Noisy Position Measurements

In this section we show that the observer-based control law from Section 4.2 stabilizes particles to a circular formation even with noisy measurements of the particle position.

Let the position measurement at time t be $\tilde{r}_k(t) = r_k(t) + g_k(t)$, where $g_k(t)$ is a (bounded) error term, such as arises when navigating underwater or by GPS. With the measurement error the error dynamics (4.2) become

$$
\begin{aligned}
\dot{\hat{r}}_k &= e^{i\theta_k} + \hat{f}_k - K_1(\hat{r}_k + g_k - r_k) \\
\dot{\hat{f}}_k &= -K_2(\hat{r}_k + g_k - r_k).
\end{aligned}
\tag{4.25}
$$

In matrix form the estimator-error dynamics represent a perturbed system:

$$
\begin{bmatrix} \dot{z}_{1,k} \\ \dot{z}_{2,k} \end{bmatrix} = \underbrace{\begin{bmatrix} -K_1 & 1 \\ -K_2 & 0 \end{bmatrix}}_{\triangleq B} \begin{bmatrix} z_{1,k} \\ z_{2,k} \end{bmatrix} - g_k \begin{bmatrix} K_1 \\ K_2 \end{bmatrix}.
\tag{4.26}
$$

Choosing $Q \in \mathbb{R}^{2\times 2}$ to be the identity matrix, the solution to the Lyapunov equation $FB + B^T F = -Q$ is

$$
F = \begin{bmatrix} \frac{(K_2+1)}{2K_1} & -\frac{1}{2} \\ -\frac{1}{2} & \frac{(K_2+K_1^2+1)}{2K_1K_2} \end{bmatrix}.
\tag{4.27}
$$

Let $c_1 = \lambda_{min}(F)$, $c_2 = \lambda_{max}(F)$, $c_3 = -\lambda_{min}(Q) = 1$, and $c_4 = 2\lambda_{max}(F)$, where λ represents the matrix eigenvalue, and let $\boldsymbol{z}_k = [z_{1,k}, z_{2,k}]^T$. We have the following result based on nonvanishing perturbation stability [31, Chapter 9].

Lemma 8. *Consider the perturbed error dynamics (4.26) and bounded perturbation*

$$|g_k \max(K_1, K_2)| \leq \delta < \frac{c_3}{c_4}\sqrt{\frac{c_1}{c_2}}x\epsilon, \tag{4.28}$$

with $0 < \epsilon < 1$ and $\boldsymbol{z}_k(t)$ in domain $D = \{\boldsymbol{z}_k(t) \in \mathbb{C}^2 \mid ||\boldsymbol{z}_k(t)|| < x\}$. For all $||\boldsymbol{z}_k(t_0)|| < \sqrt{\frac{c_1}{c_2}}x$ the solution to (4.26) will obey

$$||\boldsymbol{z}_k(t)|| \leq \sqrt{\frac{c_2}{c_1}}e^{\zeta(t-t_0)}||\boldsymbol{z}(t_0)||, \tag{4.29}$$

where

$$\zeta = \frac{(1-\epsilon)c_3}{2c_2} \tag{4.30}$$

and $||\boldsymbol{z}_k(t)||$ is ultimately bounded by

$$||\boldsymbol{z}_k(t)|| \leq \frac{c_4}{c_3}\sqrt{\frac{c_2}{c_1}}\frac{\delta}{\epsilon}. \tag{4.31}$$

Proof. With candidate Lyapunov function $V(\boldsymbol{z}_k) = \boldsymbol{z}_k^T F \boldsymbol{z}_k$, the unperturbed system satisfies

$$
\begin{aligned}
c_1||\boldsymbol{z}_k(t)||^2 &\leq V(\boldsymbol{z}_k) \leq c_2||\boldsymbol{z}_k(t)||^2 \\
\frac{\partial V}{\partial \boldsymbol{z}_k} &\leq -c_3||\boldsymbol{z}_k(t)||^2 \\
\left\|\frac{\partial V}{\partial \boldsymbol{z}_k}\right\|^2 &\leq c_4||\boldsymbol{z}_k(t)||^2,
\end{aligned}
$$

where $c_1 = \lambda_{min}(F)$, $c_2 = \lambda_{max}(F)$, $c_3 = -\lambda_{min}(Q) = 1$, and $c_4 = 2\lambda_{max}(F)$ [31,

Example 9.1]. With positive gains K_1, K_2 the origin of the unperturbed system (4.3) is exponentially stable by Lemma 4. By [31, Lemma 9.2] the perturbed system will follow (4.29) and be ultimately bounded by (4.31). □

Lemma 8 shows that the ultimate bound of the perturbed error dynamics (4.26) is proportional to δ^2, which is related to the measurement noise by (4.28). Next we use this result to extend Theorem 7 to incorporate noisy position measurements.

Theorem 10. *Let $f_k = \beta \in \mathbb{R}$ satisfy $|\beta| < 1$. Also, let $\hat{r}_k$ and $\hat{f}_k$ evolve according to (4.25) with perturbation g_k bounded by $|g_k| \le \delta/\max(K_1, K_2)$ and positive gains K_1, K_2, and K_3. The distance between solutions of model (4.1) with the control (4.9) and the set of circular formations with radius $|\omega_0|^{-1}$ and direction determined by the sign of ω_0 is ultimately bounded with ultimate bound proportional to δ^2.*

Proof. Consider the candidate Lyapunov function (4.7), whose time derivative along closed-loop solutions of (4.1) is

$$
\begin{aligned}
\dot{\hat{S}} &= \sum_{k=1}^{N} (\langle \dot{\hat{c}}_k, P_k \hat{c} \rangle + \dot{z}_{1,k} z_{1,k} + \dot{z}_{2,k} z_{2,k}) \\
&= \sum_{k=1}^{N} \Big[\langle e^{i\hat{\gamma}_k}, P_k \hat{c} \rangle (\hat{s}_k - \omega_0^{-1} \nu_k) - z_{1,k}(K_1 z_{1,k} - z_{2,k} + K_2 z_{2,k}) \\
&\qquad - g_k(z_{1,k} K_1 + z_{2,k} K_2) \Big].
\end{aligned}
$$

53

Choosing control (4.9) and ultimate bound (4.31) from Lemma 8 gives gives

$$\dot{S} = \sum_{k=1}^{N} \Bigg(- K_3 \langle P_k \hat{\boldsymbol{c}}, e^{i\hat{\gamma}_k} \rangle^2 - z_{1,k}(K_1 z_{1,k} + z_{2,k} + K_2 z_{2,k})$$

$$- g_k(z_{1,k}K_1 + z_{2,k}K_2) \Bigg)$$

$$\leq \sum_{k=1}^{N} \Bigg(- K_3 \langle P_k \hat{\boldsymbol{c}}, e^{i\hat{\gamma}_k} \rangle^2 + K_1 \|\boldsymbol{z}_k\|^2 + \frac{1}{2}(K_2 + 1)\|\boldsymbol{z}_k\|^2$$

$$+ g_k \sqrt{K_1^2 + K_2^2} \|\boldsymbol{z}_k\|^2 \Bigg)$$

$$\leq \sum_{k=1}^{N} \Bigg(- K_3 \langle P_k \hat{\boldsymbol{c}}, e^{i\hat{\gamma}_k} \rangle^2 + \left(K_1 + \frac{1}{2}(K_2 + 1) + \delta \sqrt{K_1^2 + K_2^2} \right) \|\boldsymbol{z}_k\|^2 \Bigg)$$

$$\leq \sum_{k=1}^{N} \Bigg(- K_3 \langle P_k \hat{\boldsymbol{c}}, e^{i\hat{\gamma}_k} \rangle^2$$

$$+ \underbrace{\left(K_1 + \frac{1}{2}(K_2 + 1) + \delta \sqrt{K_1^2 + K_2^2} \right) \left(\frac{\delta c_4}{\epsilon c_3} \sqrt{\frac{c_2}{c_1}} \right)^2}_{\triangleq b} \Bigg), \qquad (4.32)$$

where we used the inequalities $z_{1,k}K_1 + z_{2,k}K_2 < \sqrt{K_1^2 + K_2^2}\|\boldsymbol{z}_k\|^2$ and $2z_{1,k}z_{2,k} < \|\boldsymbol{z}_k\|^2$. The term $-K_3 \langle P_k \hat{\boldsymbol{c}}, e^{i\hat{\gamma}_k} \rangle^2 \leq 0$ is equal to zero only when $c_k = c_j$ for all pairs k and j, which implies each particle steers to a circular formation around the same fixed center. Let Ω be the set where $c_k = c_j$ for all pairs k and j, which implies $\nu_k = \omega_0 \hat{s}_k$ and $\dot{\hat{c}}_k = 0$. In Ω, $\dot{S}$ is negative definite when $K_3 \langle P_k \hat{\boldsymbol{c}}, e^{i\hat{\gamma}_k} \rangle^2 > b$. Thus solutions are attracted to within b of Ω. □

Figure 4.3 illustrates Theorem 10 for a uniform flowfield $\beta = -0.5$ and position measurements perturbed by zero mean Gaussian noise (and not truncated as required by Lemma 8) with standard deviation σ. Figure 4.3(a) shows a circular formation of $k = 5$ particles. The red tracks indicate the noisy position measure-

(a) $t = [0, 250]$ s.

(b) $t = [0, 250]$ s.
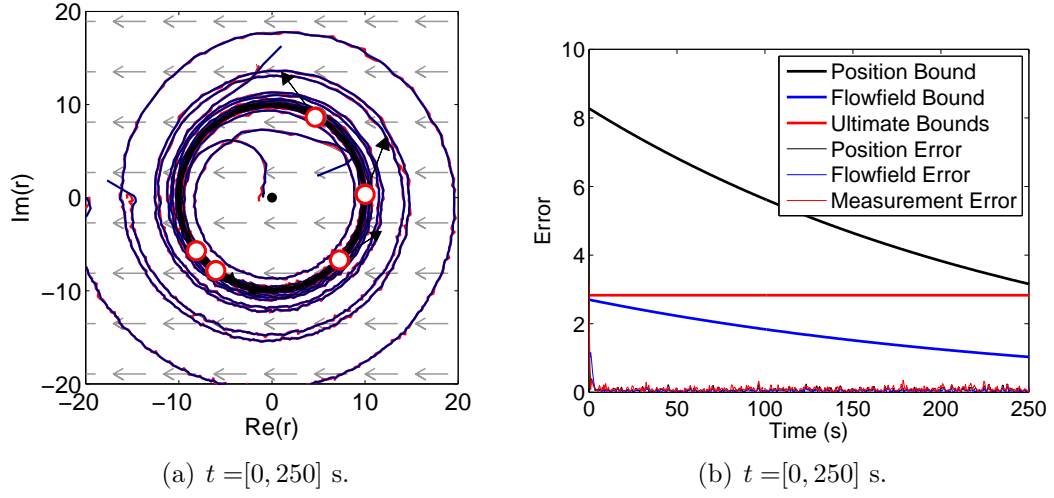
Figure 4.3: Stabilization to a circular formation in an unknown uniform flowfield with noisy position measurements.

ments and the blue tracks show the actual particle position. With $K_1 = 2.83$ and $K_2 = 2$, the constants in Lemma 8 become $c_1 = 0.204$, $c_2 = 1.298$, $c_3 = 1$, and $c_4 = 2.6$. Choosing $\epsilon = 0.99$ gives ultimate bound $b = 2.83$. A large ϵ value (less than one) increases the bounding exponential, but decreases the overall bound b.

Figure 4.3(b) shows the evolving errors for particle $k = 3$ as well as their bounding exponential functions and ultimate bound. The position error $z_{1,k} = \hat{r}_k - r_k$ with $\|z_{1,k}(t_0)\| = 3.2875$ is bounded by $24.1586 e^{-0.0051t}$ (black line). The flowfield error $z_{2,k} = \hat{f}_k - f_k$ with $\|z_{2,k}(t_0)\| = 1.1726$ is bounded by $2.518 e^{-0.0051t}$ (blue line). Both errors are ultimately bounded by $b = 2.83$ (red line).

Chapter 5

Motion Coordination in an Estimated Nonuniform Flowfield

In this chapter we provide decentralized control algorithms that enable motion coordination in an unknown, spatially varying flowfield by simultaneously estimating the flow and using that estimate to steer multiple vehicles to a circular formation. We parameterize the flowfield into a set of weighted basis functions. The coefficients of the basis functions are estimated with a decentralized information-consensus filter. The information filter is used to reconstruct the flowfield. The consensus filter enables sharing of data among the vehicles given a limited communication topology.

The inter-vehicle communication constraints may be directed, provided they are strongly connected and balanced [59]. (A strongly connected graph ensures that a communication path that obeys edge direction may be found between any vehicle to any other vehicle. The communication graph is balanced if for each vehicle the number of incoming connections is equal to the number of outgoing connections.) The estimated flowfield and its directional derivative at the vehicle locations are fed into a decentralized control law that cooperatively stabilizes vehicles to a moving formation. We require only noisy position measurements to estimate the flowfield.

Research shows that distributed control of many vehicles with communication constraints may be achieved using consensus filters [48, 59]. Lynch et al. use a consensus filter to estimate spatially varying environmental fields such as temperature

[41]. The scalar-field estimate is coupled with a gradient control to move the vehicles into sampling positions that minimize the estimation uncertainty. For a connected undirected graph [48] or a strongly connected and balanced digraph [59] a consensus filter asymptotically convergences to the average of the consensus inputs.

A consensus filter was used in combination with an information filter by Casbeer and Beard to estimate a system's dynamic state [11]. Their work shows that when the consensus filter did not converge prior to estimating the state, the decentralized error covariance estimates were conservative, and the estimated state was similar to the one obtained with the centralized estimator. Olfati-Saber also provided decentralized Kalman filter formulations [46, 50, 45, 47], developed techniques applicable to a heterogeneous group of sensors [46], and established the properties of stability for the information-consensus filter [47].

We follow the work of [41] where a combination information and consensus filter is used to estimate a global scalar field in a distributed manner. Background information on distributed estimation is provided in Section 5.1. The algorithm for consensus-based flowfield estimation and motion coordination is presented in four stages. Section 5.2 outlines the overall approach using a centralized information filter and noisy flow measurements. It also assumes that the flowfield basis vectors are known. Section 5.3 replaces the centralized filter with a decentralized information-consensus filter. Section 5.4 replaces the flow measurements with noisy position measurements. Finally, Section 5.5 relaxes the assumption that the flowfield structure is known by the information filter and instead uses an orthogonal set of cosine basis vectors in the flowfield estimation.

5.1 Background: Distributed Estimation Using an Information-Consensus Filter

This section summarizes the work of Lynch et al. [41] in which an information filter and a consensus filter were used to estimate a scalar environmental field from measurements collected by multiple vehicles. The environmental field f_k at position r_k is [41]

$$f_k = f(r_k) = \sum_{n=1}^{l} a_n \psi_n(r_k), \tag{5.1}$$

where $\boldsymbol{\psi}(r_k) \triangleq \boldsymbol{\psi}_k = [\psi_1(r_k), \psi_2(r_k), ..., \psi_l(r_k)]^T$ is the matrix of known basis vectors evaluated at r_k and $\boldsymbol{a} = [a_1, a_2, ..., a_l]^T$ is the matrix of flowfield coefficients to be estimated.

Although Lynch et al. allow the coefficients to be time-varying, here we assume that the coefficients are constant, i.e., $\dot{a}_n = 0$ for all n, and estimate them using noisy linear measurements. Each measurement $\tilde{f}_k$ is corrupted by Gaussian, zero-mean measurement noise v_k with variance $R_k \in \mathbb{C}$, so that [41]

$$\tilde{f}_k = \boldsymbol{\psi}_k^T \boldsymbol{a} + v_k. \tag{5.2}$$

The information filter is a variation of the Kalman filter that propagates forward the inverse of the error covariance [67]. Let $M = E[(\boldsymbol{a} - \hat{\boldsymbol{a}})(\boldsymbol{a} - \hat{\boldsymbol{a}})^T]$ be the coefficient error covariance.[1] The inverse error covariance $M^{-1} \triangleq I$ is called the information matrix and $\mathbf{i} = I\hat{\boldsymbol{a}}$ is the information measurement [41]. The informa-

---

[1] $E[\cdot]$ is the expected value of $[\cdot]$.

tion filter equations are obtained by substituting $M = I^{-1}$ and $\hat{a} = I^{-1}\mathbf{i}$ into the standard Kalman filter equations [67].

For this work we implemented a discrete form of the information filter. Let t be the current time and Δt the time step. The superscript $^{(-)}$ denotes the prior estimates and $^{(+)}$ denotes the updated estimates. The information filter equations are simplified under the assumption that the state a is constant and does not have process noise. These conditions imply that the predicted information covariance and information state at time t are equal to the prior values, i.e., $I^-(t) = I^+(t - \Delta t)$ and $\mathbf{i}^-(t) = \mathbf{i}^+(t - \Delta t)$. The measurement-update equations for particle k are [67, 41]

$$
\begin{aligned}
I_k^+ &= I_k^- + \boldsymbol{\psi}_k R_k^{-1} \boldsymbol{\psi}_k^T \\
\mathbf{i}_k^+ &= \mathbf{i}_k^- + \boldsymbol{\psi}_k R_k^{-1} \tilde{f}_k.
\end{aligned}
$$

Rewriting these equations using $C_k \triangleq \boldsymbol{\psi}_k R_k^{-1} \boldsymbol{\psi}_k^T$ and $\boldsymbol{y}_k \triangleq \boldsymbol{\psi}_k R_k^{-1} \tilde{f}_k$ yields [41]

$$
\begin{aligned}
I_k^+ &= I_k^- + C_k \\
\mathbf{i}_k^+ &= \mathbf{i}_k^- + \boldsymbol{y}_k.
\end{aligned}
\tag{5.3}
$$

The matrix C_k and vector $\boldsymbol{y}_k$ represent the information gained from particle k in a single update measurement. The estimated coefficients $\hat{a}_k$ for particle k are obtained from the information matrix using $\hat{a}_k = I_k^{-1}\mathbf{i}_k$ [41]. An advantage of using the information filter is that measurement updates are added to the predicted information matrix and information measurement [11], rather than performing the matrix multiplications and inversion of a standard Kalman filter. Multiple mea-

surements may be incorporated in a single update step using the following sums:
[41]

$$C \triangleq \sum_{k=1}^{N} C_k = \sum_{k=1}^{N} \boldsymbol{\psi}_k R_k^{-1} \boldsymbol{\psi}_k^T \tag{5.4}$$

and

$$\boldsymbol{y} \triangleq \sum_{k=1}^{N} \boldsymbol{y}_k = \sum_{k=1}^{N} \boldsymbol{\psi}_k R_k^{-1} \tilde{f}_k. \tag{5.5}$$

The measurement-update equations that incorporate the information from all particles are

$$\begin{aligned} I^+ &= I^- + C \\ \mathbf{i}^+ &= \mathbf{i}^- + \boldsymbol{y}, \end{aligned} \tag{5.6}$$

with the estimated coefficients $\hat{\boldsymbol{a}} = I^{-1}\mathbf{i}$. Note that the measurement variance R_k is embedded in the information update of C_k and $\boldsymbol{y}_k$, making it easy to share information among heterogeneous sensors in a group [11].

A centralized information filter can be used directly to estimate $\hat{\boldsymbol{a}}$ when all-to-all communication is available. When all-to-all communication is not available, the information filter is supplemented by a consensus filter. The consensus filter approximates the average value of an input parameter and converges to the true average as long as the (directed) vehicle communication topology is strongly connected and balanced [59], i.e., a communication link exists between all vehicles and the in-degree is equal to the out-degree of each communication node. The information-consensus filter allows vehicle k to approximate C and $\boldsymbol{y}$ using information from its neighbor set $\mathcal{N}_k$. Let $C_{(i,j),k}$ indicate the entry in the ith row and jth column of C_k. Likewise $y_{n,k}$ is the nth entry of vehicle k's measurement vector. The proportional-integral

(PI) consensus filter is [41]

$$\begin{aligned}
\dot{\tau}_k &= \xi(\tau_{0,k} - \tau_k) - K_P \sum_{j \in \mathcal{N}_k} (\tau_k - \tau_j) + K_I \sum_{j \in \mathcal{N}_k} (\eta_k - \eta_j) \\
\dot{\eta}_k &= -K_I \sum_{j \in \mathcal{N}_k} (\tau_k - \tau_j),
\end{aligned} \tag{5.7}$$

where $\tau_{0,k}$ is particle k's input to the estimated value. That is, $\tau_{0,k} = C_{(i,j),k}$ where $i, j = 1, \ldots, l$ or $\tau_{0,k} = y_{n,k}$ where $n = 1, \ldots, l$. $\xi > 0$ determines how much the consensus filter relies upon its own input relative to the inputs from other connected particles. τ_k is the consensus variable, i.e., the approximate average of $C_{(i,j),k}$ or $y_{n,k}$, η_k is an integrator variable, and K_P and K_I are the proportional and integral gains, respectively. The sums in (5.7) are computed for all the particles in the neighbor set of k, where $j \in \mathcal{N}_k$ indicates that vehicle k receives communication from vehicle j.

In the following sections we provide a distributed algorithm that uses (5.6) and (5.7) to estimate a spatially varying flowfield. The flowfield is estimated using (5.6) with inputs C and $\boldsymbol{y}$ approximated with the consensus filter (5.7).

5.2 Stabilization of Circular Formations and Centralized Flowfield Estimation Using an Information Filter

Figure 5.1(a) illustrates the design of a centralized information filter that estimates a spatially varying flowfield. The flowfield f_k is approximated by a set of basis functions as in (5.2), where the basis vector is known and the flowfield coefficients are estimated. At each time step, each vehicle measures the local flowfield at its

(a) Centralized architecture
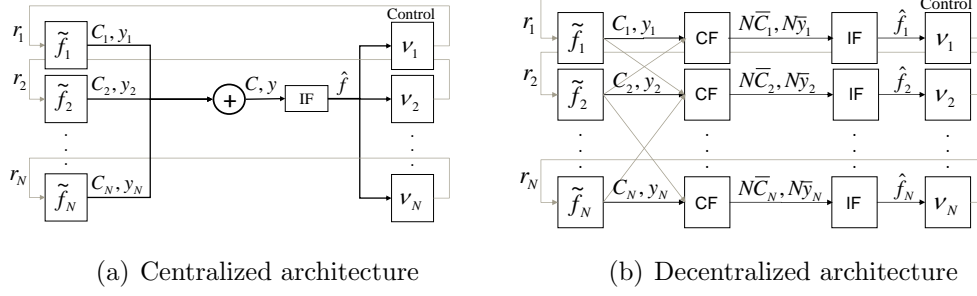

(b) Decentralized architecture

Figure 5.1: Flowfield estimation and multivehicle control architecture with (a) centralized information filter and (b) decentralized information-consensus filter.

position r_k. Equations (5.4) and (5.5) are used to obtain C and y, which represent the information gained from the local flowfield measurement. A centralized information filter uses C and $\boldsymbol{y}$ to compute the global flowfield estimate $\hat{f}$. The estimate $\hat{f}$ (and its directional derivative) are fed into each particle's steering controller. This process is repeated at each time step and the global flowfield estimate improves from the additional measurements.

Table 5.1 summarizes the centralized estimation and control algorithm.

Table 5.1: Centralized Information Filter Cooperative Control Algorithm

Input: Basis vectors $\boldsymbol{\psi}$, sensor variances R_k, and circle formation radius $|\omega_0|^{-1}$
At each time t, particle $k = 1, \ldots, N$:

1: Takes a noisy flowfield measurement $\tilde{f}_k$

2: Evaluates the basis vectors $\boldsymbol{\psi}(r_k) = \boldsymbol{\psi}_k = [\psi_1(r_k), \psi_2(r_k), ..., \psi_l(r_k)]^T$

3: Computes the information matrix $C_k = \boldsymbol{\psi}_k R_k^{-1} \boldsymbol{\psi}_k^T$ and information measurement $\boldsymbol{y}_k = \boldsymbol{\psi}_k R_k^{-1} \tilde{f}_k$

4: Shares its covariance matrix and measurement vector with all other particles and computes C and $\boldsymbol{y}$ using C_j and $\boldsymbol{y}_j$, $j = 1, \ldots, N$

5: Updates prior information matrix I^- and measurement $\mathbf{i}^-$ using (5.6)

6: Computes the estimated flowfield $\hat{f} = \boldsymbol{\psi}_k \hat{\boldsymbol{a}} = \boldsymbol{\psi}_k I^{-1} \mathbf{i}$ and control ν_k using (4.9)

We propose the following result.

Proposition 1. *Let $f(r_k) = \sum_{n=1}^{l} a_n \psi_n(r_k)$ be a spatially varying, time invariant flowfield where the $\psi_n(r_k)$ are known basis vectors and the coefficients a_n are unknown. The algorithm described in Table 5.1 forces convergence of solutions of model (4.1) to the set of circular formations with radius $|\omega_0|^{-1}$ and direction determined by the sign of ω_0.*

Proposition 1 is justified because the estimation portion of Table 5.1 is separate from the control dynamics. Due to the stability properties of the information filter [47], the flowfield estimate will improve independently from the steering control. The control becomes more accurate as the estimated flowfield converges to the true flowfield. Once the flowfield is estimated, Theorem 1 shows that steering control (4.9) drives all particles to a circular formation with the same center point and radius.

Figure 5.2 illustrates the results of numerical simulations of the centralized information filter. The flowfield is modeled using a series of sines and cosines, $f_k = a_1 \sin(\text{Re}(r_k)) + a_2 \cos(\text{Im}(r_k)) + a_3 \sin(2\text{Re}(r_k))i + a_4 \cos(2\text{Im}(r_k))i$ with coefficients $a_1 = 0.5$, $a_2 = 0.5$, $a_3 = 0.5$, and $a_4 = 0.5$. The basis vectors are $\psi_1 = \sin(\text{Re}(r_k))$, $\psi_2 = \cos(\text{Im}(r_k))$, $\psi_3 = \sin(2\text{Re}(r_k))i$, and $\psi_4 = \cos(2\text{Im}(r_k))i$. The stabilized formation of $N = 15$ particles is shown in Figure 5.2(a) after a simulation time of $t = 200$ seconds. The tracks indicate that after a short transient the particles converge to the final formation. Figure 5.2(b) shows the error between the estimated and actual coefficients for $k = 15$. Despite being fed noisy flowfield measurements,

(a) $t = [0, 200]$ s.

(b) Flowfield coefficient errors, $k = 15$.
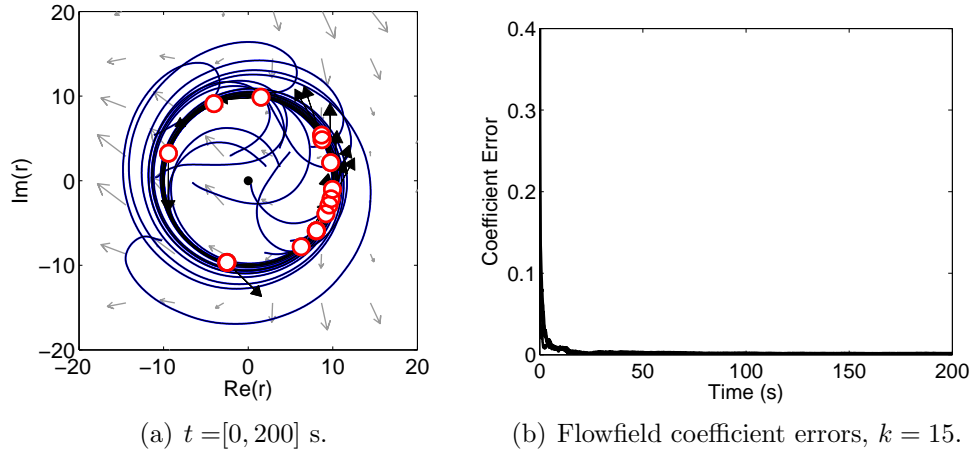
Figure 5.2: Stabilization of a circular formation in an estimated, spatially varying flowfield using a centralized information filter.

the coefficient errors rapidly converge to zero.

5.3 Stabilization of Circular Formations and Consensus-based Flowfield Estimation Using Flow Measurements

In this section we use an information-consensus filter to estimate a spatially varying flowfield in a decentralized architecture depicted in Figure 5.1(b). Each particle uses the PI consensus filter introduced in Section 5.1 to calculate $\bar{C}_k$, the approximate average of matrix (5.4), and $\bar{\boldsymbol{y}}_k$, the approximate average of measurement vector (5.5). $\bar{C}_k$ and $\bar{\boldsymbol{y}}_k$ are multiplied by the number of particles N to approximate C and $\boldsymbol{y}$, which are used in each particle's information filters to generate estimates of the flowfield coefficients. Each particle may have different coefficient estimates due to variances in the approximate average of the covariance and measurement matrix. Table 5.2 describes the distributed algorithm. Note steps 1 and 2 are identical to the centralized version.

64

Table 5.2: Decentralized Information-Consensus Filter Cooperative Control Algorithm 1

Input:	Known basis vectors $\boldsymbol{\psi}$, sensor variances R_k, circle formation radius $|\omega_0|^{-1}$, and a strongly connected and balanced communication topology

At each time step, particle $k = 1, \ldots, N$:

1: Takes a noisy flowfield measurement $\tilde{f}_k$

2: Evaluates the basis vector: $\boldsymbol{\psi}(r_k) = \boldsymbol{\psi}_k = [\psi_1(r_k), \psi_2(r_k), ..., \psi_l(r_k)]^T$

3: For $n = 1, \ldots, p$, where p is the number of consensus filter iterations, repeat:

    3a: Use the consensus filter (5.7) to estimate the components of C and $\boldsymbol{y}$

4: Updates the approximate prior information matrix I^- and measurement $\mathbf{i}^-$ using (5.6) and determines the estimated coefficients $\hat{a}_k = I^{-1}\mathbf{i}$

5: Computes the estimated flowfield $\hat{f}_k = \boldsymbol{\psi}_k \hat{a}_k = \boldsymbol{\psi}_k I^{-1}\mathbf{i}$ and control ν_k using (4.9)

The estimated coefficients are fed into a control law that drives each particle to a circular formation. To ensure fast convergence, multiple consensus updates are performed for every steering control command. The information-consensus filter runs as a separate process for each vehicle, completing as many as $p = 10$ consensus iterations between measurement updates. We propose the following result.

Proposition 2. *Let $f(r_k) = \sum_{n=1}^{l} a_n \psi_n(r_k)$ be a spatially varying, time invariant flowfield where the $\psi_n(r_k)$ are known basis vectors and the coefficients a_n are unknown. The algorithm described in Table 5.2 forces convergence of solutions of model (4.1) to the set of a circular formations with radius $|\omega_0|^{-1}$ and direction determined by the sign of ω_0.*

As with Proposition 1, Proposition 2 is justified because estimation of the flowfield is independent of the motion coordination. The combined consensus-estimation filter behaves like Table 5.1 when the consensus filter is given time to converge to the

average. Convergence of the consensus filter is assured for strongly connected and balanced communication topologies [59]. Once the flowfield is known all particles are driven to a circular configuration as proven in Theorem 1.

Figure 5.3 illustrates the result of numerical simulations of the decentralized information-consensus filter with $N = 15$. Figure 5.3(a) shows the particle circular formation after 250 seconds. The flowfield is identical to the one used in the centralized example. The particles have a strongly connected and balanced topology, communicating with only four neighbors, such that particle k receives communication directly from particles $k - 2$, $k - 1$, $k + 1$ and $k + 2$, modulus N. We set $K_I = 0.05$, $K_P = 0.5$, $\xi = .01$, and sensor variance $R_k = .01$. Figure 5.3(b) shows the error in the coefficient estimates converges to zero for particle $k = 15$. Note the error values for the consensus filter take longer to converge than in the centralized implementation; the imperfect estimates of C and $\boldsymbol{y}$ increase the duration of the transient.

(a) $t = [0, 250]$ s.
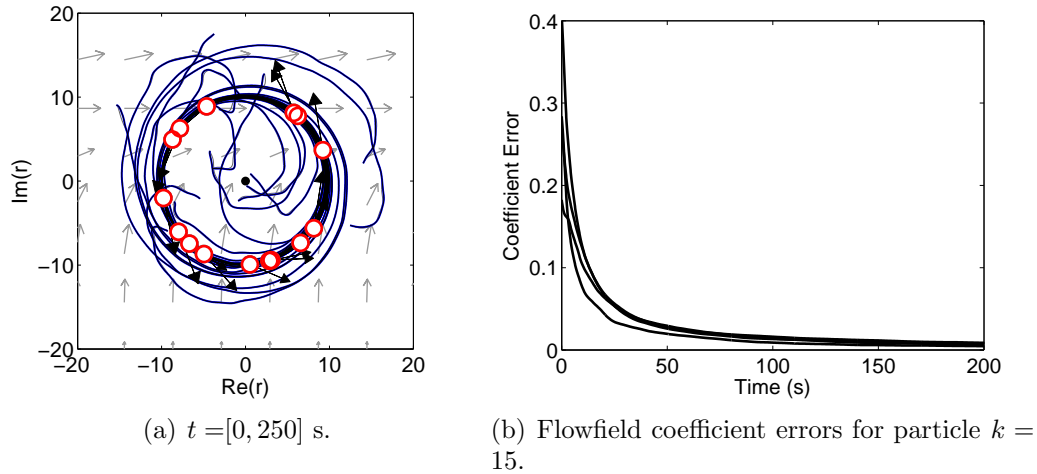
(b) Flowfield coefficient errors for particle $k = 15$.

Figure 5.3: Stabilization of a circular formation in an estimated spatially varying flowfield using a decentralized information-consensus filter.

5.4 Stabilization of Circular Formations and Consensus Based Flow-field Estimation Using Noisy Position Measurements

In this section we relax the assumption that each particle measures the local flowfield and instead require only noisy position measurements. Let $m_k(t)$ be the change in position from $t - \Delta t$ to t, subject to bounded measurement error $g_k(t)$:

$$m_k(t) = r_k(t) + g_k(t) - r_k(t - \Delta t) - g_k(t - \Delta t). \tag{5.8}$$

Using $\dot{r}_k(t) = \lim_{\Delta t \to \infty} (r_k(t) - r_k(t - \Delta t))/\Delta t$ in (5.8) yields

$$m_k(t) \approx \dot{r}_k \Delta t + g_k(t) - g_k(t - \Delta t)$$

$$m_k(t) \approx [e^{i\theta_k(t)} + f_k(t)]\Delta t + g_k(t) - g_k(t - \Delta t).$$

For a sufficiently small Δt, we assume θ_k is constant. The approximate local flowfield measurement $\tilde{f}_k(t)$ at time t is

$$\tilde{f}_k(t) = \frac{m(t)}{\Delta t} - e^{i\theta_k(t)} + \frac{g_k(t) - g_k(t - \Delta t)}{\Delta t}. \tag{5.9}$$

Δt must be chosen to be small enough so that θ can be considered constant, but not so small that the position measurement error dominates (5.9). In order to approximate a local flowfield we need to know the orientation of the velocity relative to the flow θ_k. (The speed relative to the flow is one by assumption.)

Table 5.3 presents the information-consensus filter algorithm utilizing noisy

Table 5.3: Decentralized Information-Consensus Filter Cooperative Control Algorithm 2

| **Input:** | Basis vector $\boldsymbol{\psi}$, sensor variances R_k, circle formation radius $|\omega_0|^{-1}$, and strongly connected and balanced communication topology |

At each time step t, each particle $k = 1, \ldots, N$:

1: Takes a noisy position measurement $\tilde{r}_k$

2: Use the difference between the previous and current position measurement to approximate the local flowfield measurement using (5.9)

3: Evaluates the basis vector at the measured position: $\boldsymbol{\psi}(\tilde{r}_k) \triangleq \tilde{\boldsymbol{\psi}}_k = [\psi_1(\tilde{r}_k), \psi_2(\tilde{r}_k), ..., \psi_l(\tilde{r}_k)]^T$

4: For $n = 1, \ldots, p$, where p is the number of consensus filter iterations, repeat:

    4a: Use the consensus filter to estimate the components of C and $\boldsymbol{y}$

5: Updates the approximate prior information matrix I^- and measurement $\mathbf{i}^-$ using (5.6) and determines the estimated coefficients $\hat{\boldsymbol{a}}_k = I^{-1}\mathbf{i}$

6: Computes the estimated flowfield $\hat{f}_k = \boldsymbol{\psi}_k \hat{a}_k = \boldsymbol{\psi}_k I^{-1}\mathbf{i}$ and control ν_k using (4.9)

position measurements. Note that steps 3–6 are identical to Table 5.2, steps 2–5.

Figure 5.4 illustrates the architecture of the algorithm. We propose the following result.

Proposition 3. *Let $f(r_k) = \sum_{n=1}^{l} a_n \psi_n(r_k)$ be a spatially varying flowfield where the $\psi_n(r_k)$ are known basis vectors and the coefficients a_n are unknown. Using the algorithm described in Table 5.3 forces convergence of solutions of model (4.1) to the set of a circular formations with radius $|\omega_0|^{-1}$ and direction determined by the sign of ω_0.*

When the time step is sufficiently small to ensure that the local flowfield is approximately uniform, then (5.9) is an adequate replacement for the noisy flowfield measurement of Table 5.2. Otherwise, the justification of Proposition 3 follows that
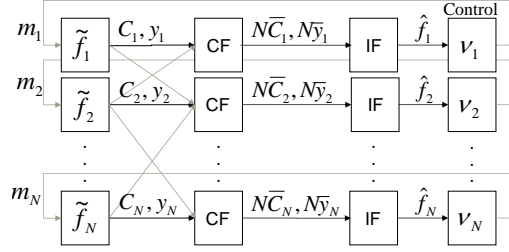
Figure 5.4: Flowfield estimation and multivehicle control architecture with decentralized information-consensus filter driven by noisy position measurements.

of Proposition 2.

Figure 5.5 illustrates the results of simulating the decentralized information-consensus algorithm using noisy position measurements. Each particle approximates the local flowfield using (5.9) and uses that approximation in an information-consensus filter to estimate the global flowfield. The flowfield model is identical to the previous examples. In this simulation we use an undirected, time-varying topology where communication is available between particles only when the distance between them is sufficiently small (less than 12). Figure 5.5(b) shows the error in the estimated flowfield coefficients, for particle $k = 15$. Using noisy position measurements to approximate the local flowfield increases the time it takes to estimate the flowfield coefficients, but the algorithm still converges to a circular formation.

5.5 Stabilization of Circular Formations and Consensus Based Flowfield Estimation with an Arbitrary Flowfield Structure

The requirement that the information filter know the underlying basis vectors which compose the flow may be too restrictive for many applications. We would like

69

(a) $t = [0, 750]$ s.
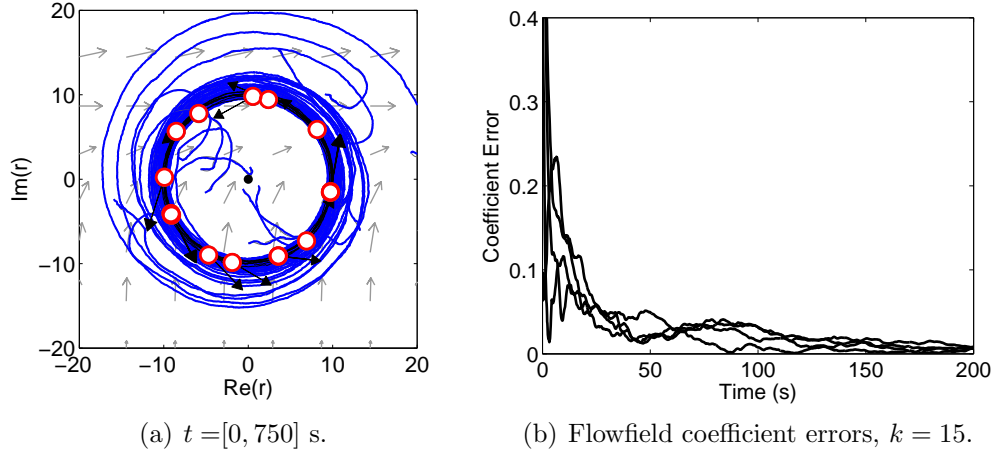
(b) Flowfield coefficient errors, $k = 15$.

Figure 5.5: Stabilization of a circular formation in an estimated spatially varying flowfield using an information-consensus filter driven by noisy position measurements.

to estimate the flowfield without need of any a prior information. In this example we show it is possible to estimate an arbitrary flowfield using a series of 2D cosine basis functions. The cosine functions replace the known basis vectors within the information-consensus filter framework provided in the previous sections. The cosine functions for the real and imaginary axis are

$$
\begin{aligned}
\psi_n(\mathrm{Re}(\boldsymbol{r}_k)) &= \cos\left(\frac{\pi n}{X}\mathrm{Re}(\boldsymbol{r}_k)\right) \\
\psi_m(\mathrm{Im}(\boldsymbol{r}_k)) &= \cos\left(\frac{\pi m}{Y}\mathrm{Im}(\boldsymbol{r}_k)\right)
\end{aligned}
$$

with X and Y representing the flowfield boundary in the real and imaginary directions of the complex plane. Let the new basis vector be

$$
\boldsymbol{\psi}(r_k) \triangleq [\psi_0(\mathrm{Re}(r_k))\psi_0(\mathrm{Im}(r_k)), ..., \psi_0(\mathrm{Re}(r_k))\psi_m(\mathrm{Im}(r_k)), ..., \psi_n(\mathrm{Re}(r_k))\psi_m(\mathrm{Im}(r_k))] \tag{5.10}
$$

The total number of basis vectors and coefficients is $l = m \times n$. We assume that the flowfield is within the span of a finite number of cosine basis vectors and therefore may be estimated exactly. However in simulation we show an example where this requirement is relaxed. As before the flowfield is defined with (5.1).

We generate a flowfield using random variables to weight coefficients in the Fourier domain. The inverse transform of the coefficients yields the global flowfield. We use the decentralized information-consensus filter presented in Section 5.4 to estimate a flowfield over a 50×50 region in the complex plane. Figure 5.6 illustrates the result of steering multiple vehicles to a circular formation in a flowfield estimated using vector (5.10). We estimated $l = 10$ coefficients. For this example we increase the number of consensus iterations completing as many as $p = 40$ iterations between measurement steps. Note that the information-consensus algorithm is computationally intense and does not scale well when estimating a large number of coefficients or completing a high number of consensus iterations. Figure 5.6(a) shows the circular formation with the actual (gray arrows) and estimated (gold arrows) flowfield as background vectors. Figure 5.6(b) depicts the percent flowfield error between the actual and estimated flowfield for particle $k = 15$. The estimated flow is not perfect since the flowfield can only be estimated perfectly using an infinite number cosine basis vectors. Errors are especially high toward the edges of the region. However, the estimated flowfield was accurate enough to provide good convergence of particles to the circular formation.

(a) $t = [0, 750]$ s.
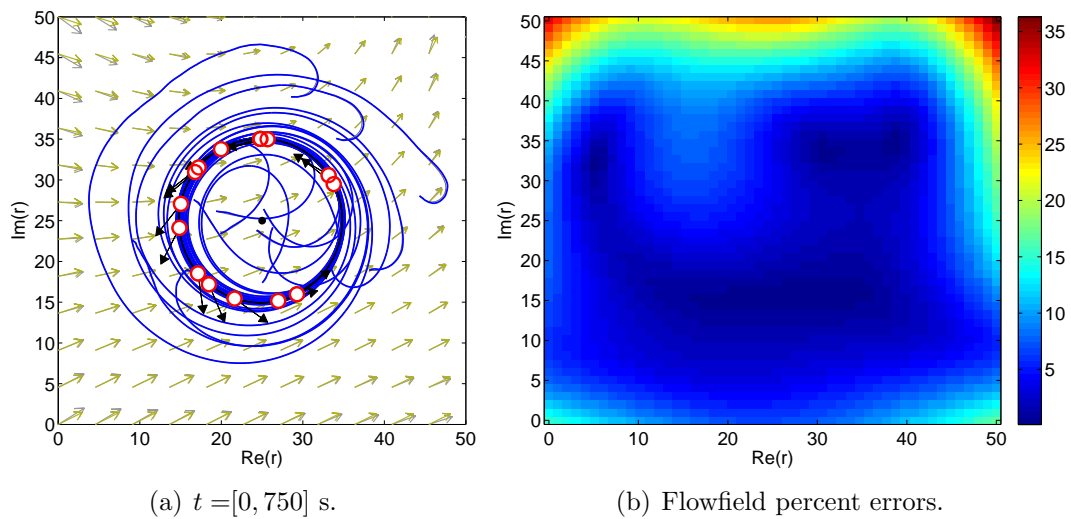
(b) Flowfield percent errors.

Figure 5.6: Stabilization of a circular formation in an estimated spatially varying flowfield using a decentralized information-consensus filter with unknown flowfield basis vectors.

Chapter 6

Application Example: Coordinated Encirclement of a Maneuvering

Target

Autonomous vehicles have been used successfully in operations and experiments for target tracking and convoy protection applications [26, 69, 64, 38]. In this chapter we show the applicability of the control laws developed in Chapter 3 and 4 to these applications by providing coordinated encirclement of a maneuvering target.

Target tracking with cooperating autonomous vehicles has been studied extensively in past research, both for stationary [4, 24, 76] and moving [77, 33, 35] targets. Frew *et al.* show collaborative encirclement of a constant-velocity target while regulating the angular separation between two vehicles [25]. In [70] this was expanded to include an unlimited number of vehicles. In both works, the desired distance from the target is governed using Lyapunov-based guidance vector fields. The spatial separation is preserved using a variable-speed controller. Each vehicle adjusts its speed to maintain the correct angular separation with the vehicle directly ahead of it. In [81] this approach was expanded to also create formations with equal temporal spacing.

A temporal spacing target tracking algorithm using a unit speed vehicle model was provided by Klein. The vehicles successfully follow a constant velocity target,

but the algorithm restricts the number of vehicles in the formation [35]. For an unlimited number of vehicles, Kingston proposed a sliding-mode algorithm that encircles moving targets [32].

Another approach used to develop decentralized cooperative tracking algorithms is to choose vehicle trajectories that optimize the potential information gain of the system [27, 52, 75]. This is an appealing approach when working with many vehicles because the total information of the system is equal to the linear combination of the information of the individuals. Using the Fisher information matrix Ousingsawat and Campbell combine individual vehicle information in a cost function to determine optimal vehicle paths for the reconnaissance of stationary targets [51]. Zhou *et al.* extend this approach to track a moving target with a team of mobile vehicles [80]. Each vehicle uses a nonlinear, range-only measurement model.

In this work we do not implement a specific sensor model for our vehicles, though other literature addresses this topic (e.g. cameras [17, 7, 76], GMTI Sensor [68, 34], radar [6, 61], multi-static radar [10, 78]). Instead we assume each autonomous vehicle measures the relative distance between itself and the target. The target is not restricted to a constant velocity, but is assumed to be accelerating. We also initially assume that the acceleration is known. However, in an application example we partially relax this assumption by discretizing the track of an accelerating target into constant velocity segments and using the control algorithms of Chapter 4 to estimate the velocity of each segment.

In this chapter we will first derive the dynamics for each unmanned vehicle (Section 6.1). These are defined in terms of an accelerating reference frame $\mathcal{B}$ with
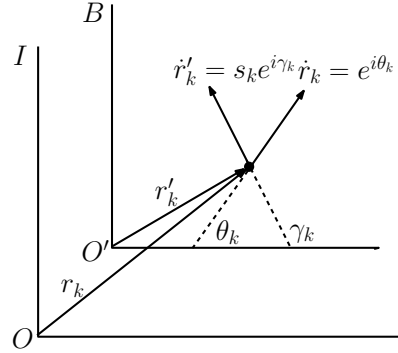
74

Figure 6.1: Relationship between inertial frame $\mathcal{I}$ and accelerating frame $\mathcal{B}$ with path trajectories.

its origin fixed to the target. We then illustrate target encirclement with three examples. In Section 6.2 a target is considered that is continuously accelerating and decelerating between two points along a fixed track. The magnitude of the velocity is always changing, but the target does not deviate from the path. Section 6.3 illustrates the coordinated encirclement of a target that is traversing a circle of fixed radius and thus constantly changing its velocity direction while maintaining a fixed magnitude. For this flowfield the time-phase parameter is used to regulate the temporal spacing of the particles. Section 6.4 depicts encirclement of a target driving through an urban environment. The target path was captured using a GPS receiver attached to a car and includes typical traffic behavior such as turns and stops. This example shows the utility of the algorithms developed in Chapter 4 to encircle a target in an estimated flowfield. Additionally, a turning-rate constraint is imposed on the vehicles as discussed in Section 3.2. All of the examples illustrate basic maneuvers of a mobile ground vehicle.

6.1 Accelerating Frame Dynamics

This section derives the equations of motion for a particle traveling in an accelerating, non-rotating reference frame $\mathcal{B}$ with origin O' fixed to the target. O' moves with respect to the inertial frame $\mathcal{I}$ with a velocity and acceleration equal to the target velocity. Two path frames are utilized for particle k as shown in Figure 6.1. With no external flowfield, the kinematics in the inertial frame (2.3) are

$$\dot{r}_k = e^{i\theta_k} \tag{6.1}$$

$$\ddot{r}_k = \dot{\theta}_k i e^{i\theta_k}. \tag{6.2}$$

The steering control is $\dot{\theta}_k = u_k$. Let r'_k be the position of the particle k relative to O'. The inertial kinematics relative to O' are

$$\dot{r}'_k \triangleq s_k(t)e^{i\gamma_k}$$

$$\ddot{r}'_k = \dot{s}_k(t)e^{i\gamma_k} + s_k(t)\dot{\gamma}_k i e^{i\gamma_k}. \tag{6.3}$$

$s_k(t)$ and γ_k are the magnitude and orientation of $\dot{r}'_k$. Let $r_{O'}$ be the position of O' with respect to O. By vector addition we have

$$\ddot{r}'_k = \ddot{r}_k - \ddot{r}_{O'}. \tag{6.4}$$

The velocity and acceleration between frames $\mathcal{I}$ and $\mathcal{B}$ is defined to be $\dot{r}'_O = v_O = v_x + iv_y$ and $\ddot{r}'_O = a_O = a_x + ia_y$, respectively. To find the equations of motion

for the particle k in frame $\mathcal{B}$, substitute (6.2) and (6.3) into (6.4), which yields

$$\dot{s}_k(t)e^{i\gamma_k} + s_k(t)\dot{\gamma}_k ie^{i\gamma_k} = u_k ie^{i\theta_k} - a_x - ia_y. \tag{6.5}$$

From Figure 6.1 and Euler's formula, observe that

$$ie^{i\theta_k} = \sin(\gamma_k - \theta_k)e^{i\gamma_k} + \cos(\gamma_k - \theta_k)ie^{i\gamma_k} \tag{6.6}$$

$$a_x = a_x(\cos\gamma_k e^{i\gamma_k} - \sin\gamma_k ie^{i\gamma_k}) \tag{6.7}$$

$$a_y = a_y(\sin\gamma_k e^{i\gamma_k} + \cos\gamma_k ie^{i\gamma_k}). \tag{6.8}$$

Substituting (6.6)–(6.8) into (6.5) yields

$$\dot{s}_k(t) = u_k \sin(\gamma_k - \theta_k) - a_x \cos\gamma_k - a_y \sin\gamma_k \tag{6.9}$$

$$\dot{\gamma}_k = \frac{1}{s_k(t)}\left(u_k \cos(\gamma_k - \theta_k) + a_x \sin\gamma_k - a_y \cos\gamma_k\right) \triangleq \nu_k. \tag{6.10}$$

Solving (6.10) for u_k and substituting into (6.9) gives

$$\dot{s}_k(t) = (s_k(t)\nu_k - a_x \sin\gamma_k + a_y \cos\gamma_k)\tan(\gamma_k - \theta_k) - a_x \cos\gamma_k - a_y \sin\gamma_k. \tag{6.11}$$

To eliminate θ_k from (6.11) we use

$$s_k(t)e^{i\gamma_k} = e^{i\theta_k} - v \tag{6.12}$$

$$s_k(t)e^{i(\gamma_k - \theta_k)} = 1 - ve^{-i\theta_k}. \tag{6.13}$$

Equating the real and imaginary parts of (6.12) and (6.13) yields

$$s_k(t) \cos \gamma_k = \cos \theta_k - v_x$$

$$s_k(t) \sin \gamma_k = \sin \theta_k - v_y$$

and

$$
\begin{aligned}
s_k(t) \cos(\gamma_k - \theta_k) &= 1 - v_x \cos \theta_k - v_y \sin \theta_k \\
&= 1 - v_x(v_x + s_k(t) \cos \gamma_k) - v_y(v_y + s_k(t) \sin \gamma_k) \\
s_k(t) \sin(\gamma_k - \theta_k) &= v_x \sin \theta_k - v_y \cos \theta_k \\
&= v_x s_k(t) \sin \gamma_k - v_y s_k(t) \cos \gamma_k \\
\tan(\gamma_k - \theta_k) &= \frac{v_x s_k(t) \sin \gamma_k - v_y s_k(t) \cos \gamma_k}{(1 - v_x^2 - v_y^2 - v_x s_k(t) \cos \gamma_k - v_y s_k(t) \sin \gamma_k)}. \quad (6.14)
\end{aligned}
$$

Substituting (6.14) into (6.11) yields

$$
\begin{aligned}
\dot{s}_k(t) &= \frac{(s_k(t)\nu_k - a_x \sin \gamma_k + a_y \cos \gamma_k)(v_x s_k(t) \sin \gamma_k - v_y s_k(t) \cos \gamma_k)}{1 - v_x^2 - v_y^2 - v_x s_k(t) \cos \gamma_k - v_y s_k(t) \sin \gamma_k} \\
&\quad - a_x \cos \gamma_k - a_y \sin \gamma_k \quad\quad (6.15)
\end{aligned}
$$

The kinematics for a particle motion relative to O' is obtained by integrating (6.15) and substituting it into (6.3). The trajectory for particle k in the inertial frame O is

$$r_k(t) = r_k'(t) + \frac{1}{2}(a_x + ia_y)t^2 + (v_x(0) + iv_y(0))t.$$

(a) Inertial frame   (b) Target frame, $t = 400$ s (c) Target frame, $t = 600$ s
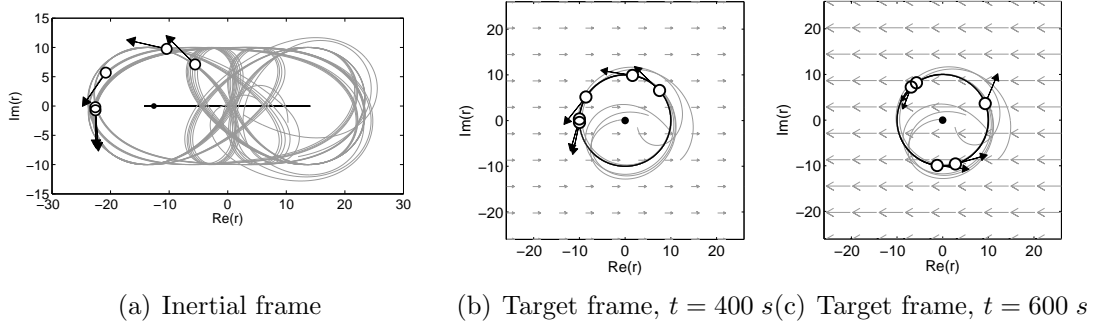
Figure 6.2: Encirclement of a maneuvering target that is accelerating along a single trackline.

6.2   Coordinated Encirclement of a Variable Speed Target

This example replicates a target that is accelerating between two points along a single trackline. Since the target velocity only varies in magnitude, it can be aligned with the real axis of an inertial frame without loss of generality. This scenario is illustrated using control (3.10) and target acceleration

$$a_x(t) = \begin{cases} \frac{-4l}{T}, & \mathrm{mod}(t, T) < \frac{T}{2} \\[2mm] \frac{4l}{T}, & \mathrm{mod}(t, T) \geq \frac{T}{2}, \end{cases} \tag{6.16}$$

where T and l represent the period and the maximum amplitude of the velocity, respectively. The target speed is greatest in the middle of the track and slows down to reverse direction at the edges.

Figure 6.2 illustrates the encirclement result of a target traversing with a period $T = 150$ seconds and a maximum velocity equal to 75% of the particle's velocity ($l = 0.75$). Figure 6.2(a) shows the simulated results in an inertial reference frame. The target is aligned with the real axis and travels left and right without

79

turning. In this figure it is not apparent that the particles converge to a circular formation. However, this is readily seen in the target-centered frame as illustrated in Figures 6.2(b) and 6.2(c). The target-centered figures illustrate the velocity by using the equivalent spatially uniform flowfield at that instance in time. Figure 6.2(b) shows the formation at $t = 400$ seconds; figure 6.2(c) shows the formation at $t = 600$ seconds, when the target is traveling at its maximum velocity of $l = 0.75$. Both target-centered figures show that the particle quickly converges to the target and then maintains a circular configuration centered around it.

6.3 Coordinated Encirclement of a Turning Target

This example illustrates the behavior of multiple vehicles as they follow a target performing a constant-rate turn of radius ρ. The target acceleration is $a_O(t) = (\eta_0^2/\rho)ie^{i2\pi t/T}$ with fixed speed η_0 and a constantly changing direction of motion. Figure 6.3 illustrates the results of using control algorithm (3.10) with speed $\eta_0 = 0.5$ (50% of the particle's velocity) and radius of curvature $\rho = 39.79$. The period of time it takes the target to traverse the circle is $T = 500$ seconds. Figure 6.3(a) illustrates the results in the inertial frame, showing the target track as it travels in a circle and the resulting particle tracks. Figures 6.3(b) and 6.3(c) display the simulation results in a target-fixed frame at $t = 400$ and $t = 800$ seconds, respectively. In these figures the particles quickly converge to a circular formation and maintain that formation even as the target accelerates.

The turning-target scenario is also used to illustrate control law (3.25), which
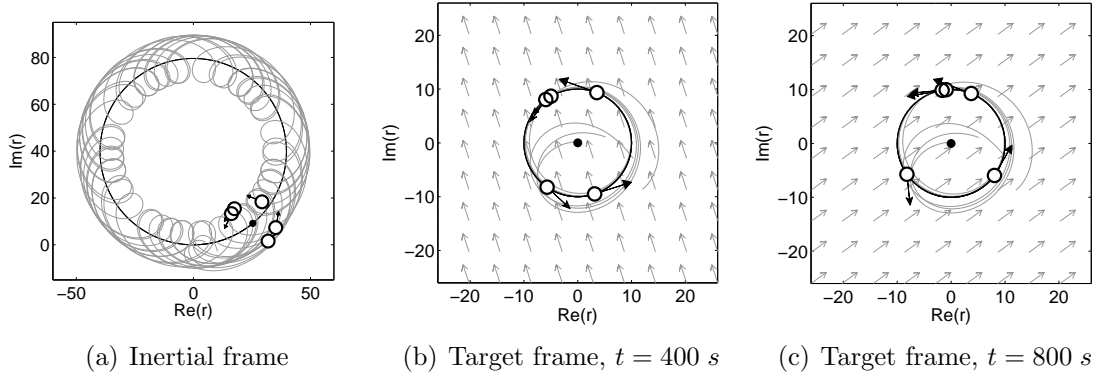
(a) Inertial frame   (b) Target frame, $t = 400\ s$ (c) Target frame, $t = 800\ s$

Figure 6.3: Encirclement of a maneuvering target that is turning at a constant rate.

(a) Inertial frame   (b) Target frame, $t = 800\ s$ (c) Target frame, $t = 1000\ s$
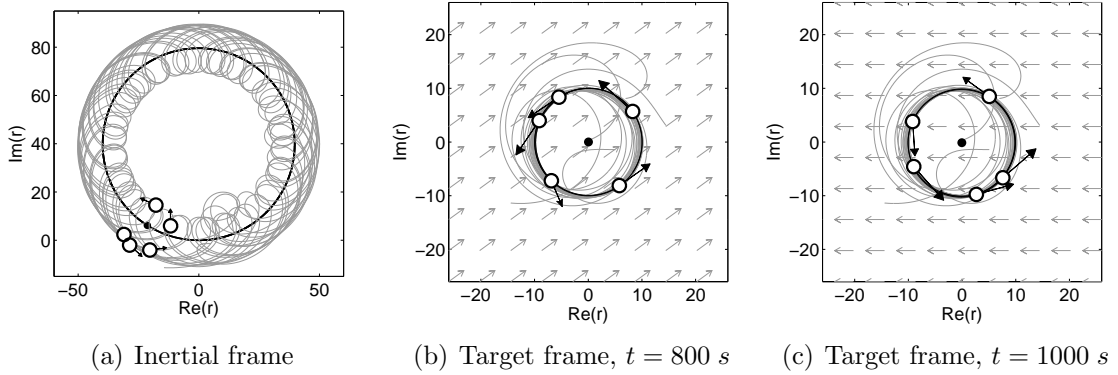
Figure 6.4: Coordinated encirclement of a maneuvering target that is turning at a constant rate.

drives the particles to a time-splay formation. Figure 6.4 illustrates this example with $N = 5$ particles centered on a target circling at an angular rate of $\Omega = 2\pi/T$, period $T = 500$ seconds, and target speed, $\eta_0 = 0.5$. Setting $\omega_0 = 0.1$ satisfies the requirement in Lemma 1. Figure 6.4(a) depicts the target and particles in the inertial frame. Figures 6.4(b) and 6.4(c) show the convergence to the time-splay configuration in the target-centered reference frame at $t = 800$ and $t = 1000$ seconds. These figures show that the particles converge to a time-splay formation even as the target accelerates.

6.4 Coordinated Encirclement of an Urban Target

In this example the work of Sections 4.2 and 3.2 are combined to encircle a maneuvering target moving with an unknown velocity. Control algorithm (4.14) is used to estimate the velocity of the target. Additionally, a bounded turn-rate constraint is placed on the autonomous vehicles. The combined particle model for this simulation is

$$\dot{\hat{r}}_k = \hat{s}_k(t)e^{i\hat{\gamma}_k}$$

$$\dot{\hat{\gamma}}_k = \text{sat}(\nu_k; \nu_{max}).$$

A set of GPS waypoints is used to model realistic behavior of a vehicle traveling in an urban environment. The vehicle tracks were collected during a twenty-minute interval while driving through a Washington, D.C. suburb. The track included stops, turns, and other kinematic behavior typical in urban traffic. The maximum velocity of the target was 18.23 m/s (approx. 40 miles/hr). It is assumed that the optimal velocity of the autonomous vehicles is 35 m/s. The velocity of the target and autonomous vehicles are normalized such that the autonomous vehicles travel at unit speed. (The normalized target velocity is 52% of the platform speed.) A turn-rate of $u_{max} = 0.23$ rad/s is imposed on the vehicles, which corresponds to a UAV maximum bank angle of 40° [77]. Following (3.38) from Lemma 2 a formation radius of $|\omega_0|^{-1} = 10$ was chosen.

Figure 6.5 illustrates the results from the urban-traffic scenario. Figure 6.5(a)

(a) Target route   (b) Inertial frame   (c) Target frame, $t = 1350 \ s$
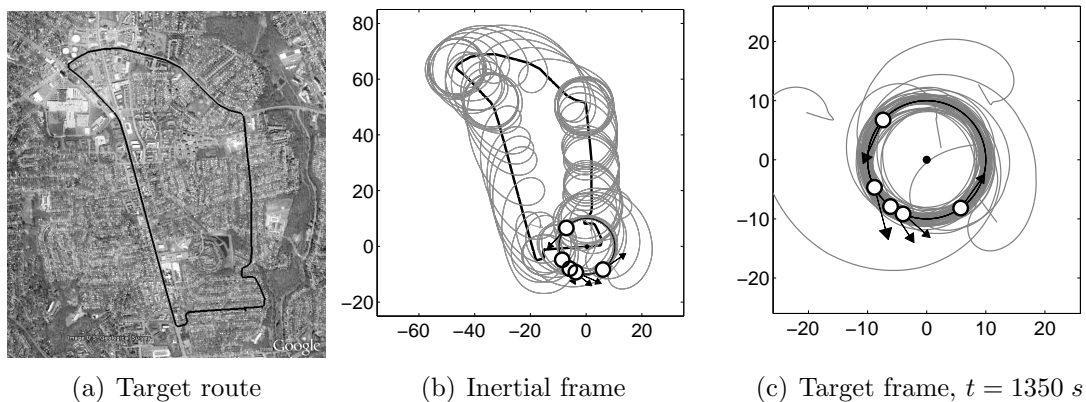
Figure 6.5: Coordinated encirclement of a target moving through urban traffic.

displays the GPS waypoints on a street map of the area. The movement of the target-fixed frame was generated from these waypoints by converting the GPS latitude and longitude points into a topocentric North-East-Down (NED) coordinate frame centered on the starting location. In this frame, the distances between the waypoints and their associated timestamps were used to determine the velocity of the target vehicle. The target velocity is piecewise constant because it is constructed out of a discrete set of waypoints and does not consider acceleration. Discontinuities of the velocity are especially pronounced when the vehicle turns sharply as both the direction and magnitude may change suddenly. Although the velocity of the target is being estimated, the vehicles are able to measure the relative position between itself and the target. Figure 6.5(b) displays both the target and vehicle tracks in the inertial frame. (The distance units are based upon the normalized speed of the ground vehicle.) The figure shows separations in the vehicle tracks that correspond to the velocity of the target. When the target is traveling quickly the cyclic tracks are spaced farther apart than in the slower moving parts of the track. Points at

83

which the target is stopped (due to traffic lights) are evident by the track circle over that point. Figure 6.5(c) shows the circular formation in the target-fixed frame for the twenty minute time interval. This figure highlights the effect of the velocity discontinuities on the formation: particles exhibit a period of transient behavior after each maneuver, before converging to a circular formation.

Chapter 7

Experimental Results: Motion Coordination on an Unmanned Aerial Vehicle Testbed

In this chapter the control algorithms developed in Chapters 3 are implemented on two Procerus Unicorn UAVs. The Unicorn (pictured in Figure 7.1) is a hand launchable, delta wing air vehicle that comes in various sizes. UAVs with 48 and 60 inch wingspans were used for these experiments. Each UAV uses a Kestral autopilot and is commanded from the ground station, Virtual Cockpit, with a wireless serial connection. A secondary connection between Virtual Cockpit and Matlab is used to execute the algorithms by sending bank angle commands. Figure 7.2 illustrates the UAV experiment architecture. As shown, the ground station may control multiple vehicles simultaneously. State information from each UAV is sent to the ground station at regular intervals and then forwarded on to the Mat-

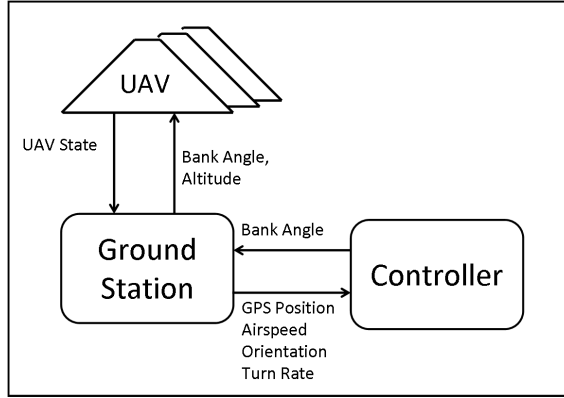Figure 7.1: Two Procerus UAVs with 60 inch wingspans.

Figure 7.2: UAV flight experiment architecture for multiple UAVs.

lab control module. The controller uses a unique identification number tied to the autopilot to differentiate between aircrafts. This ID is present in all communication packets, including the navigation and telemetry packets which are used to calculate the aircraft's desired roll angle. The roll angle is the only command input we send to the autopilot. The autopilot automatically controls the altitude and airspeed.

Figure 7.3 shows the communication chain for the experimental setup. The control commands are executed in Matlab which sends/receives information from the ground station using TCP/IP packets. Commands are converted to a binary stream in Virtual Cockpit and sent wirelessly to the vehicle's autopilot through a com box. The autopilot receives then executes the command using PID loops. Vehicle state information is directed through the same communication chain in the opposite direction.

The remainder of this chapter discusses the results from flight experiments and the process taken to setup the experimental testbed. The equipment used for these experiments was borrowed from the Johns Hopkins University Applied Physics Laboratory. Section 7.1 shows how we convert the turn-rate from the control algorithms
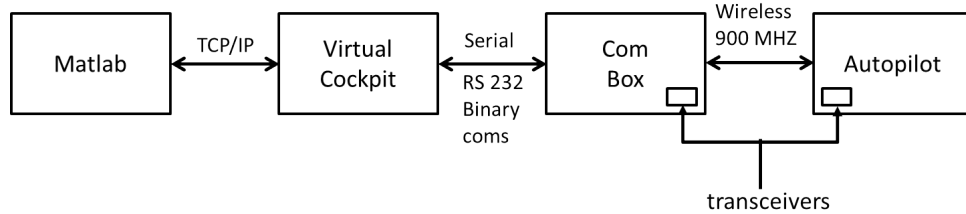
Figure 7.3: Flight experiment communication diagram.

of Chapters 3 into a roll command for the autopilot. Prior to flight, we incorporated the UAVs into a hardware-in-the-loop (HIL) simulator to test our algorithms using a high fidelity model. HIL simulation results are given in Section 7.2. The outdoor flight test results are shown in Figure 7.3.

7.1 Constant Velocity Dynamic Model

In this section we explain the implementation used to apply the control algorithms of Chapters 3 to flying UAVs. The UAVs steer using coordinated turns determined by the bank angle. We assume the UAVs are traveling at constant, non-unit speed v_0 (although the control algorithms update when the air speed of the vehicle changes) and maintain a fixed altitude. As is done in previous work [14, 3, 40], the speed is incorporated into the particle model (2.1) as follows

$$
\begin{aligned}
\dot{r}_k &= v_0 e^{i\theta_k} + f_k = s_k e^{i\gamma_k} \\
\dot{\nu}_k &= \dot{\gamma}_k.
\end{aligned}
\tag{7.1}
$$

These experiments assume a uniform flowfield of moderate strength (i.e. $|\eta(t)| < v_0$) defined as $f(t) = \eta(t)e^{i\xi(t)}$, where $\eta(t)$ is the magnitude of the flow and $\xi(t)$ is

the direction. The inertial speed is

$$
\begin{aligned}
s_k(t) &= \sqrt{\mathrm{Re}\{(\eta(t)e^{i\xi(t)} + v_0 e^{i\theta_k})(\eta(t)e^{-i\xi(t)} + v_0 e^{-i\theta_k})\}} \\
&= \sqrt{v_0^2 + (\eta(t))^2 + 2\eta(t)v_0(\cos\theta_k \cos\xi(t) + \sin\theta_k \sin\xi(t))}. \quad (7.2)
\end{aligned}
$$

$s_k(t)$ is expressed as a function of γ_k and $f(t)$ by substituting (2.5) and (2.6) into (7.2) and rearranging the result to obtain the quadratic equation

$$
(s_k(t))^2 - 2\eta(t)(\cos\gamma_k \cos\xi(t) + \sin\gamma_k \sin\xi(t))s_k(t) + (\eta(t))^2 - v_0^2 = 0. \quad (7.3)
$$

Solving (7.3) for $s_k(t)$ (using the positive root since $s_k(t) > 0$) yields

$$
\begin{aligned}
s_k(t) &= \eta(t)(\cos\gamma_k \cos\xi(t) + \sin\gamma_k \sin\xi(t)) \\
&\quad + \sqrt{v_0^2 + (\eta(t))^2((\cos\gamma_k \cos\xi(t) + \sin\gamma_k \sin\xi(t))^2 - 1)} \quad (7.4) \\
&= \langle e^{i\gamma_k}, f(t)\rangle + \sqrt{v_0^2 - \langle ie^{i\gamma_k}, f(t)\rangle^2}. \quad (7.5)
\end{aligned}
$$

Substituting (7.5) into (2.11) determines the steering control input for the UAV.

Each UAV is commanded by changing the desired bank angle. To convert the steering control, u_k, into a roll command we assume the UAV will execute a coordinated turn (i.e. no side slip, constant airspeed, and level altitude). The equation which relates a bank angle to a turn-rate for a coordinated turn is [58, Chapter 5], [77]

$$
u_k = v_0^{-1} g \tan\phi_k \quad (7.6)
$$

where ϕ_k is the airplane roll and g is the gravitational constant. Note that this equation holds true even in the presence of wind [58, 63]. Inverting (7.6) gives the roll command,

$$\phi_k = \tan^{-1}\left(\frac{u_k v_0}{g}\right). \tag{7.7}$$

The assumptions made in order to derive this equation do not generally hold for either aircraft flight or HIL simulations. To compensate for errors in the calculated roll we also incorporate a PID control on the turn-rate error, $z_k = u_k - \tilde{u}_k$, where $\tilde{u}_k$ is the measured turn-rate as given by the autopilot. The PID control ensures the desired turn-rate u_k is achieved. The gap between the desired and actual turn-rate can cause a large deviation when driving a UAV to a circle (HIL experimentation shows a 10 meter error when commanding 50 meter radius circle). The correcting PID term is

$$\phi_{P,k} = K_P z_k + K_D \dot{\tilde{z}}_k + K_I \int_0^t z_k(\tau)\,\mathrm{d}\tau, \tag{7.8}$$

where t is the current time. $\tilde{z}_k(t) = \alpha(z_k(t - \Delta t)) + (1 - \alpha)(z_k(t))$ is the error after a first-order smoothing. α is a gain determining how much we trust the current measurement. We smooth the measurement prior to differentiating to reduce the impact of noise. $\dot{\tilde{z}}_k$ is calculated using the difference between concurrent values and the time difference of packet updates. (The simulator does not provide timestamps with packet updates so we compute the time difference using the ground station system time.) The desired bank angle sent to the autopilot is

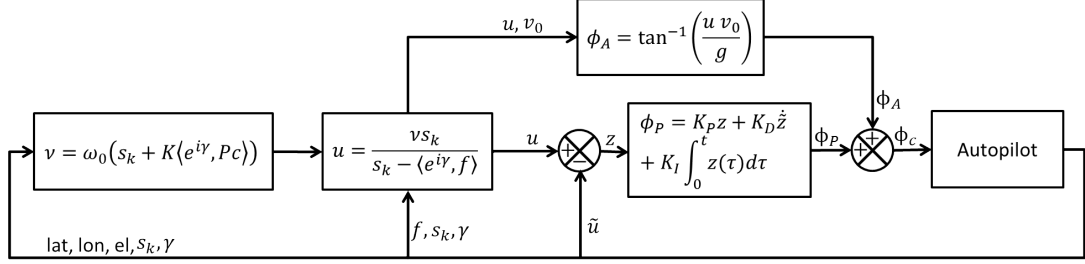$$\phi_{C,k} = \phi_{A,k} + \phi_{P,k} \tag{7.9}$$

Figure 7.4: Feedback control loop to steer UAV into a circle using bank angle commands.

where $\phi_{A,k}$ is the approximate roll command (7.7).

The bank angle control loop for a non-prescribed center point is given in Figure 7.4. The autopilot outputs the UAV position, ground speed s_k, and course heading which is used to compute the inertial steering control ν_k. This value is used with the known wind (as estimated by the autopilot) to compute u_k. The approximate bank angle (7.7) and correcting term (7.8) are feed back to the autopilot.

UAVs have a maximum maintainable bank angle before they stall. For a desired radius we find the maximum bank angle needed to converge to a circle by extending the analysis done in Section 3.2.1. Assuming a uniform, time-invariant flowfield $f_k = \eta \in \mathbb{R}$, circle radius $|\omega_0|^{-1}$, and constant airspeed $v_0 > 0$, then the maximum required turn-rate (see (3.38)) is

$$u_{max} = \frac{|\omega_0|(v_0 + |\eta|)^2}{v_0} > 0. \tag{7.10}$$

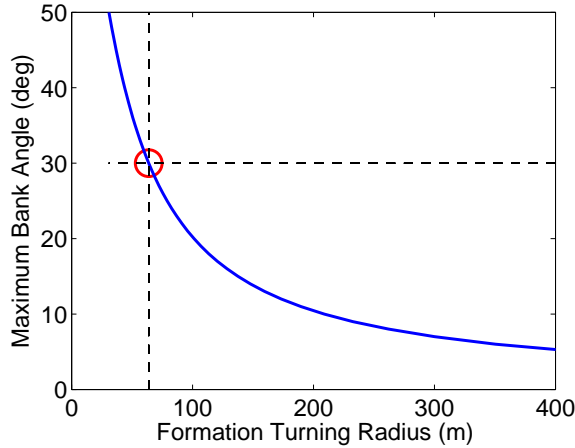Substituting (7.10) into (7.7) gives the maximum required bank angle to achieve a

90

Figure 7.5: Maximum turn radius as a function of bank angle.

desired radius of $|\omega_0|^{-1}$,

$$\phi_{max} = \tan\left(\frac{|\omega_0|(v_0 + |\eta|)^2}{g}\right)^{-1} > 0. \tag{7.11}$$

Figure 7.5 shows the relationship between the maximum bank angle and the minimum possible turn radius $|\omega_0|^{-1}$ given an airspeed of $v_0 = 14 \ m/s$ and $\eta = 5 \ m/s$. Relationship (7.11) only holds when (7.6) is exact. HIL simulations and flight experiments show that (7.6) is an approximation that degrades at higher bank angles. Figure 7.6 quantifies the bank angle approximation. In an HIL experiment a UAV was commanded to a set of discrete bank angles ranging from $0°$ to $30°$ in one degree increments. After an initial transient, we measured the turn-rate and compared it to the bank angle approximation (7.6). The results show that the approximation is closest for low bank angles and diverges as the angle increases. The test was repeated with a simulated wind of 2 m/s and 5 m/s and gave the same results (also shown in Figure 7.6, but occluded by measurements with zero wind).
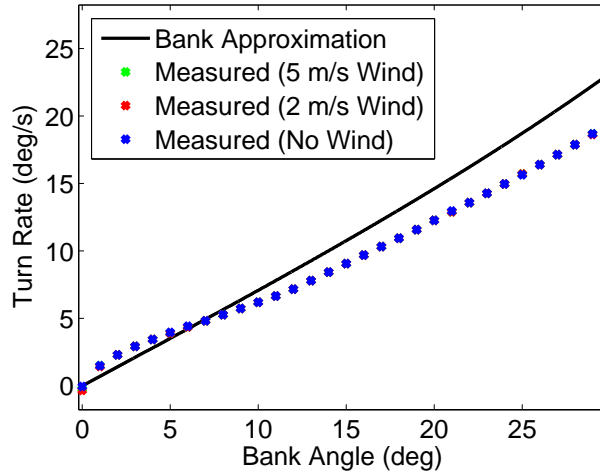
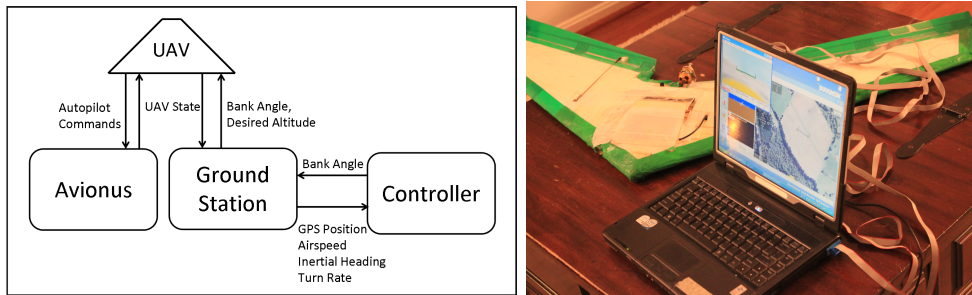Figure 7.6: Relationship between turn-rate and bank angle.

Figure 7.7: Architecture of hardware-in-the-loop configuration.

7.2   Hardware-in-the-Loop Simulation

An HIL simulator was used to test the control algorithms. Figure 7.7 illustrates the simulation architecture and shows its setup for a single vehicle. It resembles the experimental configuration, but with the addition of the Avionus module. Avionus is a flight simulator that takes the UAV actuator commands and uses them to determine state parameters. The simulated state is fed back to the UAV and subsequently sent to the ground station either through a serial connection or wireless transceiver. The HIL simulator allows testing of control algorithms on UAV hardware prior to flying.

The HIL simulation provides a good testing environment, but has some key differences when compared with outdoor flight. They include:

1. HIL incorporates Avionus, a software program which provides a linear 6-DOF model of the aircraft. In flight the aircraft dynamics will differ from the model.

2. The simulation has less noise due to projecting forward the exact position according to the model.

3. The communication chain differs slightly with the simulator and flight configurations. Figure 7.8 shows the communication diagram for the HIL simulator. The chain follows that of a flight configuration (Figure 7.3), but has an addition link to Avionus.

4. State information is less likely to be dropped or delayed in the HIL simulation. In both the HIL simulations and outdoor experiments information can be lost or delayed both connecting to the ground station through the wireless transceiver and between the ground station and Matlab module. In our testing we had fewer communication difficulties during simulation experiments than outdoor flight tests.

5. HIL simulates a known, spatially-invariant wind rather than the time varying and spatially varying wind of the real world. In our control algorithms we use the autopilot's estimate of the wind which is based upon the difference between GPS velocity and airspeed. The estimate is only assumed to be correct after the UAV computes the speed difference for the full range of headings. Variable
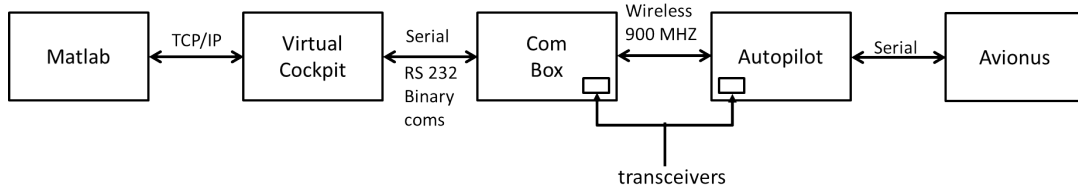
Figure 7.8: HIL communication diagram.

winds and gusts will not be measured in the UAVs estimates.

Using the HIL simulator we tested control algorithms (3.6) and (3.10) to steer vehicles to circular formations with prescribed and non-prescribed centers. We first tested (3.6) to drive two UAVs to a circle of radius 150 meters and center point determined by initial conditions. Figure 7.9 illustrates the result. We used PID values $K_P = .2$, $K_D = .2$, and $K_I = 1$ and did not simulate wind. Figure 7.9(a) gives the trajectories of the two aircraft along with the final instantaneous circle center and trajectory (dashed lines). When the simulation started the aircraft were traveling in nearly perpendicular directions, however, they quickly adjusted and converged to a circular formation. Figure 7.9(b) gives the desired and measured turn-rates for each aircraft. With no wind the desired turn-rate settles to a constant value and the measured turn-rate quickly follows. Figure 7.9(c) gives an error value by measuring the distance between the two UAV's instantaneous circle centers as determined by (3.1). This measure incorporates error in both the UAV position and orientation. After a short duration (approx. 100 seconds) the UAVs converge to the same center point giving a mean error of under 2 meters (1.3% of the circle radius) for the rest of the flight.

The second HIL test also used control (3.6), but added a 2 m/s easterly wind

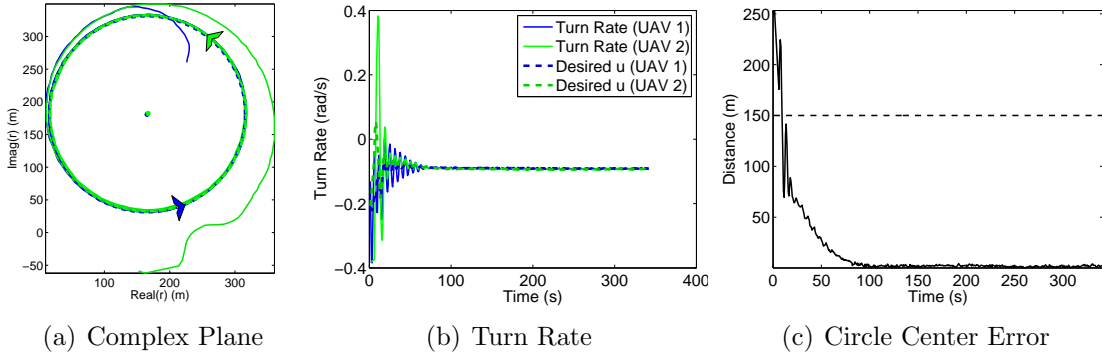| (a) Complex Plane | (b) Turn Rate | (c) Circle Center Error |

Figure 7.9: Controlling to a 150 meter non-prescribed center circle (no wind).

while driving the vehicles to a 150 meter radius circular formation of unprescribed center location. Figure 7.10 illustrates the result. With wind the trajectories of the two aircraft (Figure 7.10(a)) take longer to converge and have a larger error between the circle centers (Figure 7.10(c)). Also depicted in Figure 7.10(a) is the wind magnitude and direction at intervals along the trajectories (gray arrows). Figure 7.10(b) gives the desired and measured turn-rates for each aircraft. The desired turn-rate is not constant, but oscillates as it progresses around the circle. The measured turn-rate fluctuates significantly in the presence of a wind. After the initial convergence toward a common circle (approx. 100 seconds) the UAVs maintain a mean error of 10 meters between instantaneous centers, 6.7% of the circle radius.

We next tested control algorithm (3.10) to steer two vehicles to circular formations with 150 meter radii and prescribed center locations for both wind and no wind conditions. Without wind (Figure 7.11) the UAVs converge well to the circle center. The distance from the prescribed circle center for each UAV is shown in Figure 7.11(c). After 100 seconds, the mean error from the prescribed circle center is 2.6 meters for the first UAV and 1.4 meters for the second (1.7% and 0.9% of the
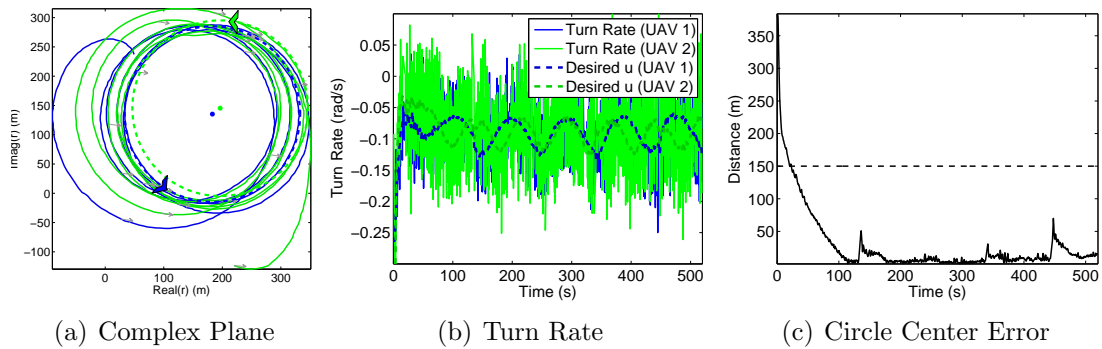
(a) Complex Plane   (b) Turn Rate   (c) Circle Center Error

Figure 7.10: Controlling to a 150 meter non-prescribed center circle (2 m/s east wind).

(a) Complex Plane   (b) Turn Rate   (c) Circle Center Error
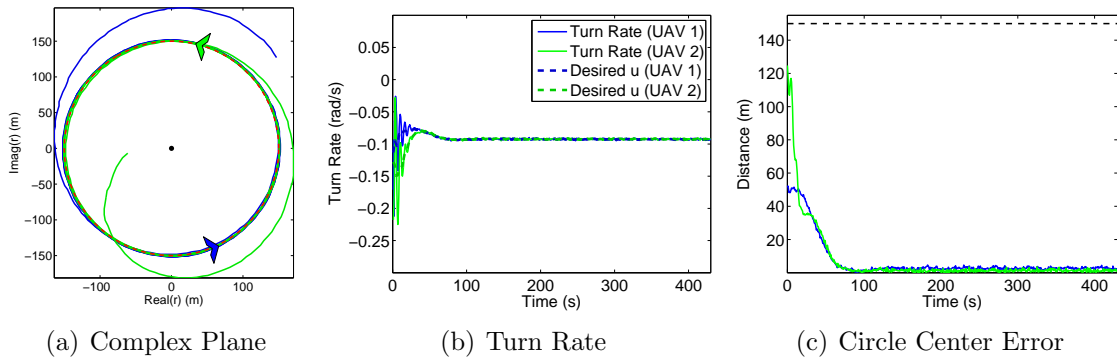
Figure 7.11: Controlling to a 150 meter prescribed center circle (no wind).

circle radius respectively). The desired turn-rates converge well to the measured turn-rates as depicted in Figure 7.11(b).

With wind the vehicles have greater difficulty converging to the desired circle center. Figure 7.12 shows the trajectories of two vehicles in a 5 m/s east wind. The mean error from the circle center is 7.2 meter and 12.3 meter for the first and second UAVs (4.8% and 8.2% of the circle radius). Each UAV has a desired turn-rate which oscillates as it progresses through the circle. In wind the measured turn-rate fluctuates significantly as the UAVs try to maintain a constant speed and fixed altitude.

(a) Complex Plane   (b) Turn Rate   (c) Circle Center Error

Figure 7.12: Controlling to a 150 meter prescribed center circle (5 m/s east wind).

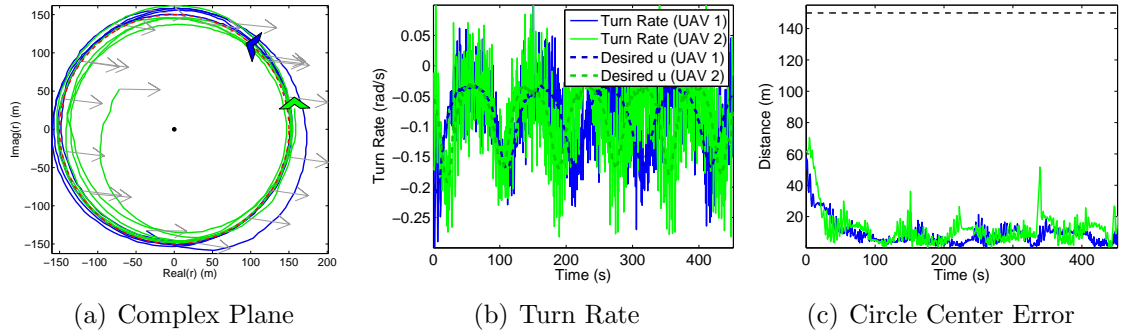In Figure 7.13 we illustrate coordinated encirclement of a prescribed circle with radius 100 meters using control (3.25) with a uniform flow, i.e. $\Omega = 0$. In this simulation the second UAV (green trajectory track) is traveling with a slightly faster airspeed than the first UAV (blue trajectory track). To maintain the splay state, the slower vehicle steers to a smaller circle radius. Figure 7.13(d) shows the phase difference between the vehicles. The vehicles do not converge perfectly to the desired separation (shown in the dashed line), keeping a 3% error in the phase differences. Figure 7.13(c) gives a mean circle distance error of 12 meters for the first UAV and 14 for the second UAV. To implement control (3.25) we had to continuously recalculate the progress of each UAV around the circle. This is due to the vehicles's constantly changing air speed and wind estimate which effect the orbit period. When deriving the continuous simulation examples found in Section 3.1.3 it was observed that we needed low error tolerances in the ODE algorithm to get the time-splay configuration to converge. In simulation updates occur for the position approximately 3 times per second. This frequency may be to slow to drive the vehicles to the splay state.

97

(a) Complex Plane

(b) Turn Rate

(c) Circle Center Error

(d) Time Phase
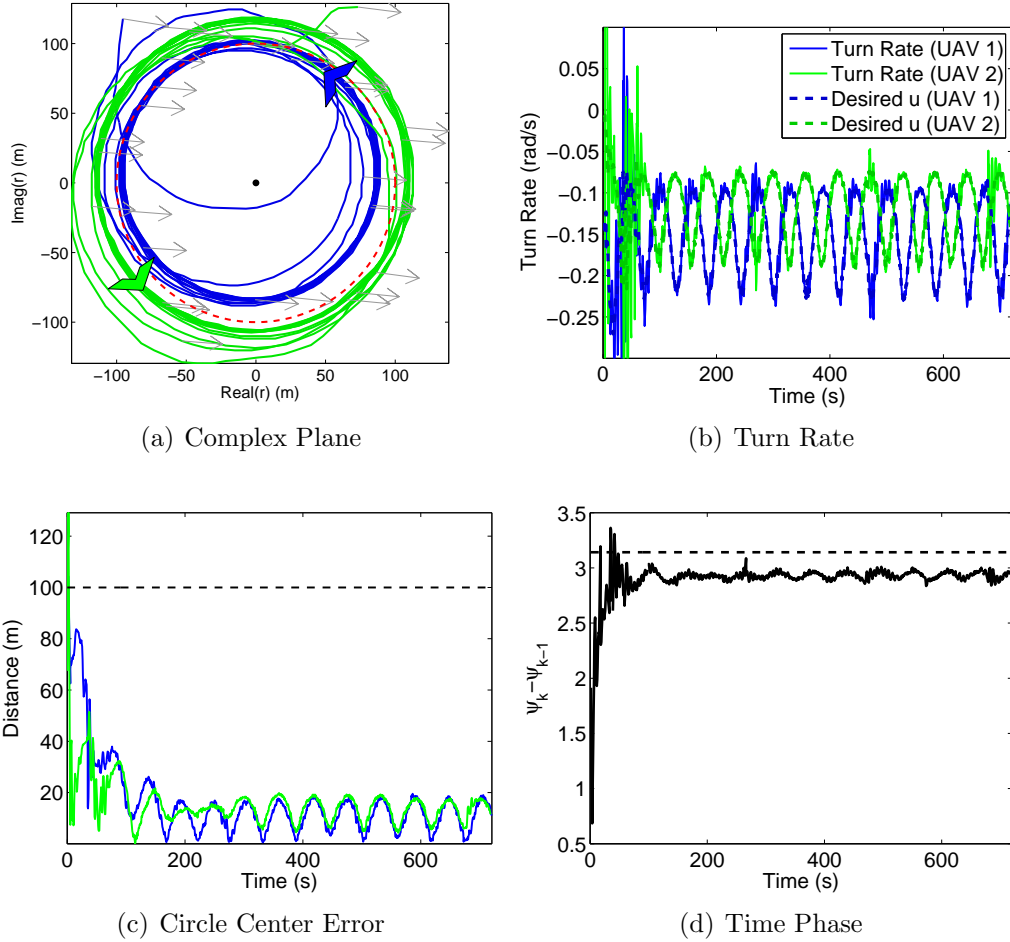
Figure 7.13: Coordinated encirclement to a 100 meter prescribed center circle (3 m/s east wind).

7.3 Experimental Results

In this section we present the results from outdoor flight experiments. Test data was gathered on two separate flight days. The first day we flew a single 48 inch wingspan Unicorn UAV. On the second flight day we flew two UAVs each having 60 inch wingspans. An additional flight day was attempted (prior to the second day), but it was unsuccessful due to reliance on inconsistently populated data. In order to improve the accuracy of the PID term, the control algorithm was altered (after the first flight day) to use the UAV's GPS timestamp rather the ground station's

system time. Unfortunately, this value is not always set in the navigation packet and resulted in erroneous roll commands to be sent to the autopilot. Representative results from the successful flight days will be presented in the following sections.

7.3.1 First UAV Flight Day

Preliminary tests were made on a single aircraft to vet the control algorithms. The tests were made using a Procerus Unicorn with 48 inch wingspan. Figure 7.14 shows ground preparations made prior to the flight and Figure 7.15 shows the UAV while in flight. Weather conditions were good with measured winds ranging from 1.5-6.0 m/s. We tested control (3.10) steering the vehicle to prescribed circle centers. In Figure 7.16 we show a vehicle orbiting a 60 meter radius circle. Around 2.5 minutes into the flight we lost communication with the aircraft for 11 seconds (dashed line in Figure 7.16(a)). When communication returned the aircraft had lost airspeed and altitude which it regained while reconverging to the circular formation. In Figure 7.16(b) we show the error distance between the UAV's instantaneous cir-

(a) Levi DeVries performs a pre-flight test on the UAV.

(b) Jon Castelli connects the hardware components prior to flight.

Figure 7.14: Preparing UAVs for flight outdoor tests.

Figure 7.15: Procerus Unicorn UAV in flight.

(a) Complex Plane

(b) Circle Center Error
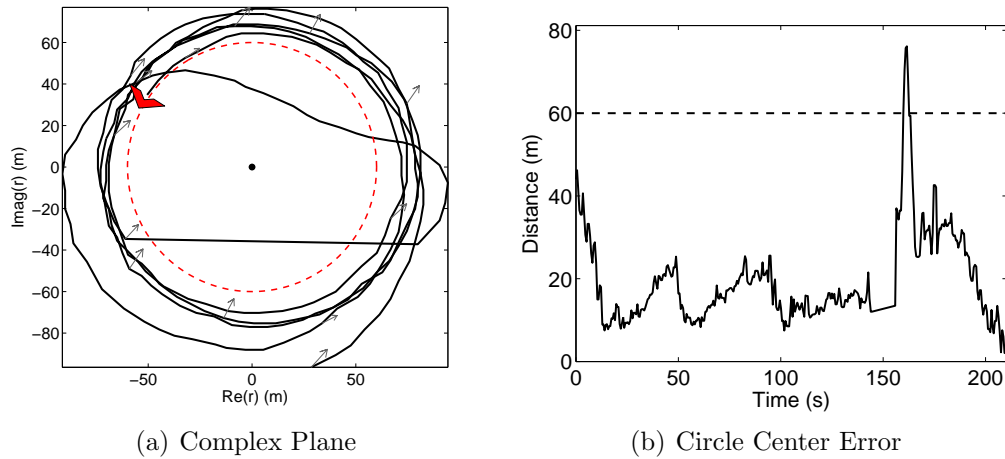
Figure 7.16: Controlling to a 60 meter prescribed center circle (variable wind approx. 1.5 m/s magnitude and north-northeast direction).

cle center and the desired circle center. The dashed line provides a reference of the desired circle radius. For the entire flight the mean error distance was 19.4 meters or 32% of the circle radius. Prior to the communication loss the error was 14.8 meters (25%).

Figure 7.17 depicts a second flight test. In this example we steer the UAV to a circular formation of 70 meters in the presence of a stronger wind (approx. 5 m/s). The flight trajectory is depicted in Figure 7.17(a) and the circle center error in Figure 7.17(b). The mean error for the UAV flight was 14.6 meters (21% of radius
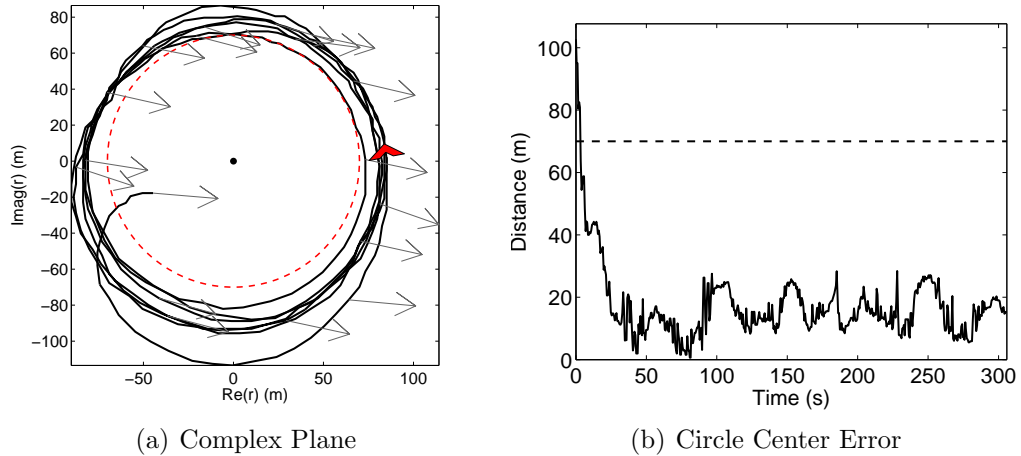
(a) Complex Plane

(b) Circle Center Error

Figure 7.17: Controlling to a 75 meter prescribed center circle (variable winds averaging 5 m/s in an east-southeast direction).

circle).

7.3.2 Second UAV Flight Day

On the second flight day we used two Unicorn UAVs to test control (3.10) steering the vehicle to prescribed circle centers and coordinated control (3.25) which drives the vehicles to a time-splay formation. Wind conditions were stronger ranging from 3-6 m/s (approx. 7-13 miles/hour) with occasional gusts (as noted from the ground) throughout all flights. We commanded each UAV to different altitudes to ensure they would not collide. They were commanded to maintain a 14 m/s airspeed. A different antenna was used in these flight tests which ameliorated the communication problems experienced during the first day.

The first test was made using a single UAV (depicted with blue trajectory tracks) using control (3.10) to drive the vehicle to a prescribed circle center with radius of 150 meters. The flight lasted for approximately 5 minutes with variable

101

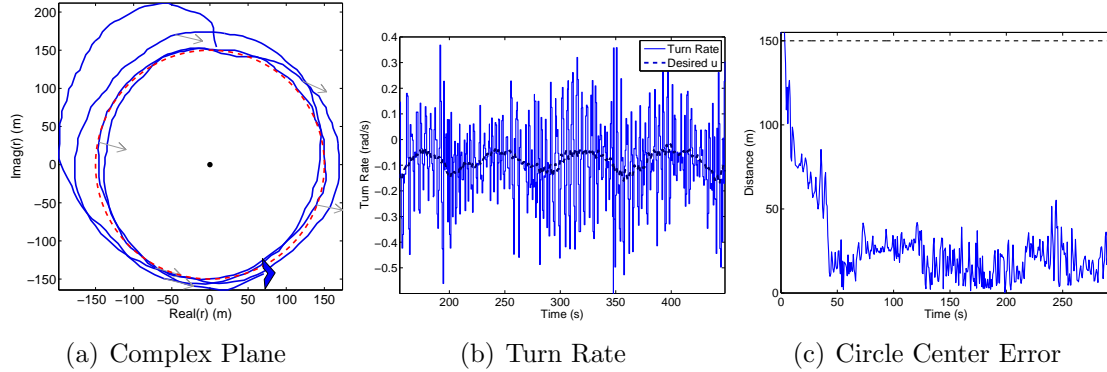| (a) Complex Plane | (b) Turn Rate | (c) Circle Center Error |

Figure 7.18: Controlling to a 150 meter prescribed center circle (variable 3-4 m/s south-southeast wind).

winds ranging from 3-4 m/s blowing in a east-southeast direction. Figure 7.18 illustrates the result. The UAV converged to the circle and made three additional loops as shown in Figure 7.18(a). The measured verses desired turn rate for the UAV is shown in Figure 7.18(b). The error between the UAVs instantaneous circle center and the desired circle center is shown in Figure 7.18(c). After the initial convergence which took approximately 50 seconds, the UAV maintains a mean error of 27 meters or 13% of the circle radius.

A second UAV was launched to show cooperative control of two vehicles. The second vehicle (depicted with green trajectory tracks) vehicle did not perform well. It had trouble maintaining both its desired altitude and airspeed. The airspeed oscillated with a high frequency, but averaged 14.5 m/s. The altitude fluctuated with occasional drops of 15+ meters. Figure 7.19 shows the trajectories of the two vehicles. The measured turn rate is noisy, but the desired turn rate for each vehicle follows the cyclic pattern needed to maintain a circle. The error between the first vehicle's instantaneous circle center and the desired circle center is 26 meters or 17% of the circle radius. As expected from the poorer performance of the second

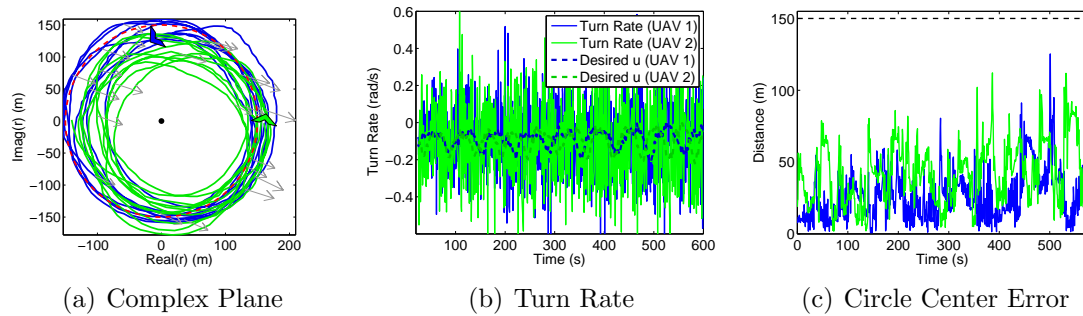(a) Complex Plane   (b) Turn Rate   (c) Circle Center Error

Figure 7.19: Encirclement to a 150 meter prescribed center circle (3 m/s east wind).

vehicle, the mean error is 42 meters (28%). This test flight lasted approximately 10 minutes and displayed highly variable winds measured between 3-5 m/s directed to the southeast. Note that the winds are measured by the UAVs using the airspeed and GPS velocity over a wide range of headings. It is not expected that the UAVs will measure wind gusts or high frequency changes.

We also used algorithm (3.25) to illustrate coordinated control (Figure 7.20). Figure 7.20(a) shows the trajectories of the two vehicles. When the algorithm starts they are positioned in approximately the same location. They then separate and endeavor to maintain the correct spacing along the path. The gains for the control were chosen with a stronger pull towards the correct separation rather than converging to the circular formation. With the two UAVs traveling at different speeds this is difficult to maintain. However, as Figure 7.20(d) shows, the UAVs are able to oscillate about the correct separation with a mean error of 14% error in phase. Figure 7.20(c) shows the circle center error. UAV 1 has a mean circle center error of 43 meters, 43% of the 100 meter radius. UAV 2 has a mean error of 53 meters. Wind varied between 3-6 m/s in an east-southeast direction over the 9 minute test.
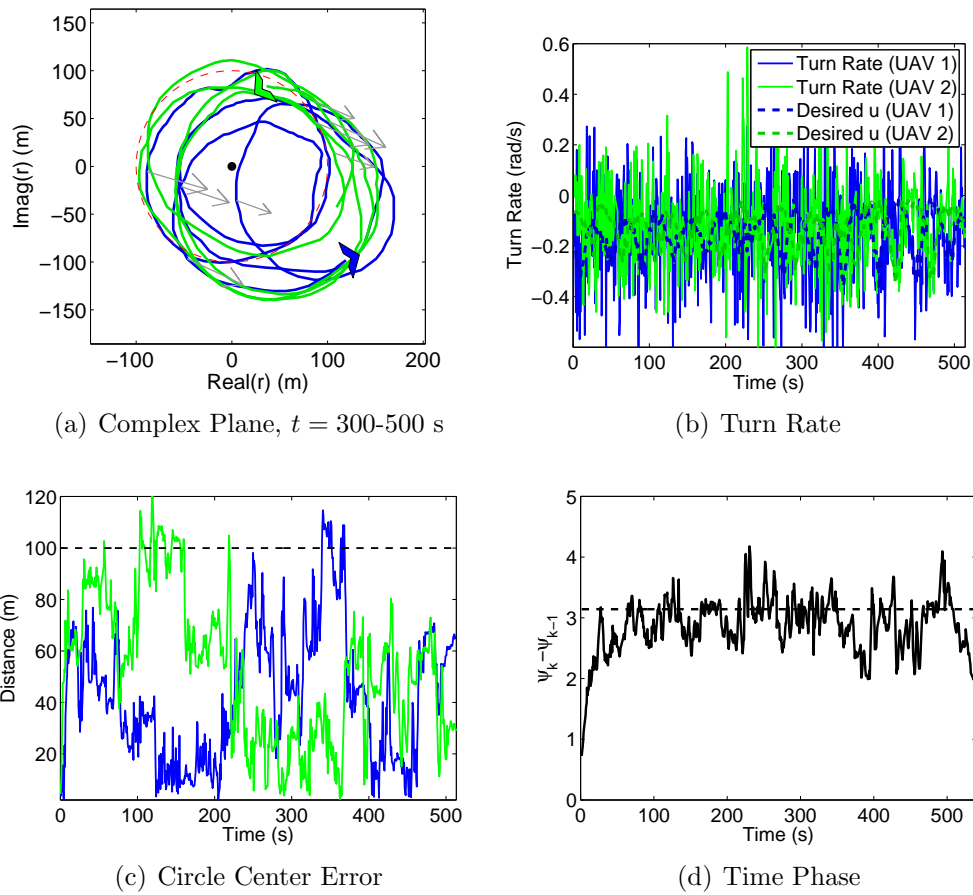
(a) Complex Plane, $t = 300\text{-}500$ s

(b) Turn Rate

(c) Circle Center Error

(d) Time Phase

Figure 7.20: Coordinated encirclement to a 100 meter prescribed center circle (4 m/s east wind).

104

Chapter 8

Conclusions and Suggestions for Future Work

Cooperative control improves the capability of unmanned vehicles to gather information, track targets, and perform various autonomous missions. The decentralized algorithms presented in this dissertation regulate vehicle formations in a spatiotemporal flowfield of moderate strength.

Given a known and time-varying flowfield, we provide an algorithm to steer vehicles to a circular formation determined by the initial conditions of the vehicles. A symmetry-breaking virtual particle is introduced to generate formations with a prescribed center location. For a time-varying and spatially uniform flowfield, an algorithm is provided to stabilize a circular formation in which the temporal spacing between particles is regulated. It is also shown that including a turning-rate bound on the vehicles does not alter the main results.

For unknown flowfields observer-based control algorithms are presented which simultaneously estimate the flowfield and use that estimate to stabilize a moving formation. Initially, we provide an approach for uniform flowfields where each vehicle independently estimates the flow using noisy measurements of its own position. We then present a distributed estimation algorithm comprised of a consensus filter to share information garnered from noisy position measurements, and an information filter to reconstruct a spatially varying flowfield.

Numerical simulations illustrate the capability to cooperatively encircle maneuvering targets that turn, accelerate, and operate in an urban environment. HIL simulations and flight experiments show that the algorithms can be adapted to UAVs. Each UAV inputs a roll command which is derived from the steering control of our motion coordination algorithms using a bank angle approximation and PID correction term. The HIL simulations show good performance for circular formations with prescribed and non-prescribed circle centers and time-splay formation. Flight experiments were also conducted with UAVs showing that the vehicle successfully encircled a prescribed center location.

There are a number of potential areas in which this work can be extended. Expanding the information-consensus filter to incorporate time-varying basis coefficients would provide estimation in time-varying as well as spatially varying flowfields. Additionally, a more efficient representation of the flowfield could be determined. Using an orthogonal set of basis vectors to describe a flow requires an arbitrarily large number of coefficients to be estimated. It is likely that only a sparse set of these basis functions are needed to represent the flow. Reducing the number of coefficients would drastically improve the runtime performance of the consensus filter.

Much improvement could be made in implementing the motion coordination algorithms on UAVs and analyzing the flight results. An examination of the full aircraft model would provide insight into the performance degradation of HIL simulations and outdoor flights when operating in strong winds. The performance was also effected by time delays. The control algorithms provided in this dissertation are continuous, but a discrete version was implemented on the UAVs. An analysis

of the effects of time-delay and stability on the discretized algorithms should be completed. Time delays can be reduced by moving the control algorithm to hardware linked directly to the autopilot. This bypasses the ground station and wireless transmitter in getting the state information to the controller.

Bibliography

[1] J. Almeida, C. Silvestre, and A. Pascoal. Coordinated Control of Multiple Vehicles with Discrete-Time Periodic Communications. In *IEEE Conference on Decision and Control*, pages 2888–2893, 2007.

[2] L. B. Arranz, A. Seuret, and C. C. de Wit. Translation Control of a Fleet Circular Formation of AUVs under Finite Communication Range. In *IEEE Conference on Decision and Control*, pages 8345–8350, Shanghai, P.R. China, 2009.

[3] L. B. Arranz, A. Seuret, and C. C. de Wit. Contraction Control of a Fleet Circular Formation of AUVs under Limited Communication Range. In *American Control Conference*, pages 1–6, Baltimore, Maryland, 2010.

[4] R. W. Beard, T. W. McLain, M. A. Goodrich, and E. P. Anderson. Coordinated Target Assignment and Intercept for Unmanned Air Vehicles. *IEEE Transactions on Robotic and Automation*, 18(6):911–922, 2002.

[5] M. Burger and K. Y. Pettersen. Curved Trajectory Tracking for Surface Vessel Formations. In *IEEE Conference on Decision and Control*, pages 7159–7165, December 2010.

[6] M. E. Campbell and J. Ousingsawat. On-line Estimation and Path Planning for Multiple Vehicles in an Uncertain Environment. In *AIAA Guidance, Navigation, and Control Conference*, Monterey, California, 2002.

[7] M. E. Campbell and W. W. Whitacre. Cooperative Tracking Using Vision Measurements on SeaScan UAVs. *IEEE Transactions on Control Systems Technology*, 15(4):613–626, 2007.

[8] Y. Cao and W. Ren. Distributed Coordinated Tracking via a Variable Structure Approach - Part I : Consensus Tracking. In *American Control Conference*, pages 4744–4749, Baltimore, Maryland, 2010.

[9] Y. Cao and W. Ren. Distributed Coordinated Tracking with Reduced Interaction via a Variable Structure Approach. *IEEE Transactions on Automatic Control*, 57(1):33–48, 2012.

[10] D. W. Casbeer. *Decentralized Estimation Using Information Consensus Filters with a Multi-Static UAV Radar Tracking System*. PhD thesis, Brigham Young University, 2009.

[11] D. W. Casbeer and R. W. Beard. Distributed Information Filtering using Consensus Filters. In *American Control Conference*, pages 1882–1887, St. Louis, Missouri, 2009.

[12] D. W. Casbeer, D. B. Kingston, R. W. Beard, and T. W. McLain. Cooperative forest fire surveillance using a team of small unmanned air vehicles. *International Journal of Systems Science*, 37(6):351–360, May 2006.

[13] H. Chao and Y. Chen. Surface Wind Profile Measurement Using Multiple Small Unmanned Aerial Vehicles. In *American Control Conference*, pages 4133–4138, Baltimore, Maryland, 2010.

[14] J. Cochran and M. Krstic. Source Seeking with a Nonholonomic Unicycle without Position Measurements and with Tuning of Angular Velocity Part I : Stability Analysis. In *IEEE Conference on Decision and Control*, pages 6009–6016, 2007.

[15] A. M. P. De Leege, M. Mulder, and M. M. Van Paassen. Novel Method for Wind Estimation Using Automatic Dependent Surveillance-Broadcast. *Journal of Guidance, Control, and Dynamics*, 35(2):648–652, 2012.

[16] L. DeVries and D. A. Paley. Multivehicle Control in a Strong Flowfield with Application to Hurricane Sampling. *Journal of Guidance, Control, and Dynamics*, 35(3):794–806, 2012.

[17] V. N. Dobrokhodov, I. I. Kaminer, K. D. Jones, and R. Ghabcheloo. Vision-Based Tracking and Motion Estimation for Moving targets using Small UAVs. In *American Control Conference*, pages 1428–1433, Minneapolis, Minnesota, 2006.

[18] J. Elston and E. W. Frew. Reduction of Computational Complexity for Guidance of Unmanned Aircraft through Strong Wind Fields. In *AIAA Guidance, Navigation, and Control Conference*, Chicago, Illinois, August 2009.

[19] J. Elston and E. W. Frew. Unmanned Aircraft Guidance for Penetration of Pre-Tornadic Storms. *Journal of Guidance, Control, and Dynamics*, 33(1):99–107, 2010.

[20] C. C. Eriksen, T. J. Osse, R. D. Light, T. Wen, T. W. Lehman, P. L. Sabin, J. W. Ballard, and A. M. Chiodi. Seaglider: A Long-Range Autonomous Underwater Vehicle for Oceanographic Research. *IEEE Journal Oceanic Engineering*, 26(4):424–436, 2001.

[21] J. A. Fax and R. M. Murray. Graph Laplacians and Stabilization of Vehicle Formations. In *IFAC World Congress*, pages 283–288, Barcelona, Spain, July 2002.

[22] J. A. Fax and R. M. Murray. Information Flow and Cooperative Control of Vehicle Formations. *IEEE Transactions on Automatic Control*, 49(9):1465–1476, 2004.

[23] E. Fiorelli, N. E. Leonard, P. Bhatta, D. A. Paley, R. Bachmayer, and D. M. Fratantoni. Multi-AUV Control and Adaptive Sampling in Monterey Bay. *IEEE Journal of Oceanic Engineering*, 31(4):935, 2006.

[24] M. Flint, M. Polycarpou, and E. Fernhdez-Gaucherand. Cooperative Control for Multiple Autonomous UAV's Searching for Targets. In *IEEE Conference on Decision and Control*, pages 2823–2828, Las Vegas, Nevada, 2002.

[25] E. W. Frew, D. A. Lawrence, and S. Morris. Coordinated Standoff Tracking of Moving Targets Using Lyapunov Guidance Vector Fields. *Journal Guidance, Control, and Dynamics*, 31(2):290–306, 2008.

[26] B. K. Funk, J. C. Castelli, A. S. Watkins, C. B. McCubbin, A. J. Marshall, J. D. Barton, A. J. Newman, C. K. Peterson, J. T. DeSena, D. A. Dutrow, and P. A. Rodriguez. JEFX 10 Demonstration of Cooperative Hunter Killer UAS and Upstream Data Fusion. In *SPIE Defense, Security, and Sensing Conference*, volume 8045, pages 1–19, Orlando, Florida, 2011.

[27] B. P. Grocholsky, H. F. Durrant-Whyte, and P. W. Gibbens. Information-Theoretic Approach to Decentralized Control of Multiple Autonomous Flight Vehicles. In *Society of Photo-Optical Instrumentation Engineers (SPIE) Conference Series*, volume 4196, pages 348–359, 2000.

[28] C. Hager, D. Zarzhitsky, H. Kwon, and D. Pack. Cooperative Target Localization Using Heterogeneous Unmanned Ground and Aerial Vehicles. In *IEEE/RSJ International conference on Intelligent Robots and Systems*, pages 2952–2957, Taipei, Taiwan, 2010.

[29] C. H. Hsieh, Z. Jin, D. Marthaler, B. Q. Nguyen, D. J. Tung, A. L. Bertozzi, and R. M. Murray. Experimental Validation of an Algorithm for Cooperative Boundary Tracking. In *American Control Conference*, volume 2, pages 1078–1083, 2005.

[30] E. W. Justh and P. S. Krishnaprasad. Equilibria and Steering Laws for Planar Formations. *Systems and Control Letters*, 52(1):25–38, 2004.

[31] H. K. Khalil. *Nonlinear Systems*. Prentice Hall, third edition, 2002.

[32] D. B. Kingston. *Decentralized Control of Multiple UAVs for Perimeter and Target Surveillance*. PhD thesis, Brigham Young University, Provo, Utah, December 2007.

[33] D. B. Kingston and R. W. Beard. UAV Splay State Configuration for Moving Targets in Wind. In *Advances in Cooperative Control and Optimization*, pages 109–128. Springer Berlin/Heidelberg, 2007.

[34] T. Kirubarajan and Y. Bar-Shalom. Tracking Evasive Move-Stop-Move Targets with a GMTI Radar Using a VS-IMM Estimator. *IEEE Transactions on Aerospace and Electronic Systems*, 39(3):1098–1103, 2003.

[35] D. J. Klein and K. A. Morgansen. Controlled Collective Motion for Trajectory Tracking. In *American Control Conference*, pages 5269–5275, Minneapolis, Minnesota, June 2006.

[36] J. W. Langelaan, N. Alley, and J. Neidhoefer. Wind Field Estimation for Small Unmanned Aerial Vehicles. *Journal of Guidance, Control, and Dynamics*, 34(4):1016–1030, 2011.

[37] N. R. J. Lawrance and S. Sukkarieh. Autonomous Exploration of a Wind Field with a Gliding Aircraft. *Journal of Guidance, Control, and Dynamics*, 34(3):719–733, 2011.

[38] J. Lee, R. Huang, A. Vaughn, X. Xiao, J. K. Hedrick, M. Zennaro, and R. Sengupta. Strategies of Path-Planning for a UAV to Track a Ground Vehicle. *AINS Conference*, 2003.

[39] N. E. Leonard and E. Fiorelli. Virtual Leaders, Artificial Potentials and Coordinated Control of Groups. In *IEEE Conference on Decision and Control*, pages 2968–2973, Orlando, Florida, December 2001.

[40] N. E. Leonard, D. A. Paley, F. Lekien, R. Sepulchre, D. M. Fratantoni, and R. E. Davis. Collective Motion, Sensor Networks, and Ocean Sampling. *Proceedings of the IEEE*, 95(1):48–74, 2007.

[41] K. M. Lynch, I. B. Schwartz, P. Yang, and R. A. Freeman. Decentralized Environmental Modeling by Mobile Sensor Networks. *IEEE Transactions on Robotics*, 24(3):710–724, 2008.

[42] I. Maza and A. Ollero. Multiple UAV Cooperative Searching Operation Using Polygon Area Decomposition and Efficient Coverage Algorithms. In *Distributed Autonomous Robotic Systems 6*, pages 221–230. Springer Japan, 2007.

[43] R. M. Murray. Recent Research in Cooperative Control of Multivehicle Systems. *Journal of Dynamic Systems, Measurement, and Control*, 129(5):571–583, 2007.

[44] P. Ögren, E. Fiorelli, and N. E. Leonard. Cooperative Control of Mobile Sensor Networks: Adaptive Gradient Climbing in a Distributed Environment. *IEEE Transactions on Automatic Control*, 49(8):1292–1302, 2004.

[45] R. Olfati-Saber. Ultrafast Consensus in Small-World Networks. In *American Control Conference*, pages 2371–2378, Portland, Oregon, June 2005.

[46] R. Olfati-Saber. Distributed Tracking for Mobile Sensor Networks with Information-Driven Mobility. In *American Control Conference*, pages 4606–4612, 2007.

[47] R. Olfati-Saber. Kalman-Consensus Filter: Optimality, Stability, and Performance. In *IEEE Conference on Decision and Control held jointly with Chinese Control Conference*, pages 7036–7042, December 2009.

[48] R. Olfati-Saber, J. A. Fax, and R. M. Murray. Consensus and Cooperation in Networked Multi-Agent Systems. *Proceedings of the IEEE*, 95(1):215–233, 2007.

[49] R. Olfati-Saber and R. M. Murray. Graph Rigidity and Distributed Formation Stabilization of Multi-Vehicle Systems. In *IEEE Conference on Decision and Control*, pages 2965–2971, December 2002.

[50] R. Olfati-Saber and J. S. Shamma. Consensus Filters for Sensor Networks and Distributed Sensor Fusion. In *IEEE Conference on Decision and Control*, pages 6698–6703, Seville, Spain, December 2005.

[51] J. Ousingsawat and M. E. Campbell. Establishing Trajectories for Multi-Vehicle Reconnaissance. In *AIAA Guidance, Navigation, and Control Conference*, number AIAA-2004-5224, pages 2188–2199, Providence, Rhode Island, August 2004.

[52] J. Ousingsawat and M. E. Campbell. Optimal Cooperative Reconnaissance Using Multiple Vehicles. *Journal of Guidance, Control, and Dynamics*, 30(1):122–132, 2007.

[53] D. A. Paley, N. E. Leonard, and R. Sepulchre. Stabilization of Symmetric Formations to Motion Around Convex Loops. *Systems and Control Letters*, 57(3):209–215, 2008.

[54] D. A. Paley and C. Peterson. Stabilization of Collective Motion in a Time-Invariant Flow Field. *Journal of Guidance, Control, and Dynamics*, 32(3):771–779, 2009.

[55] D. A. Paley, L. Techy, and C. A. Woolsey. Coordinated Perimeter Patrol with Minimum-Time Alert Response. In *AIAA Guidance, Navigation, and Control Conference*, number AIAA-2009-6210, August 2009.

[56] J. Petrich and K. Subbarao. On-Board Wind Speed Estimation for UAVs. In *AIAA Guidance, Navigation, and Control Conference*, Portland, Oregon, 2011.

[57] J. Petrich, C. A. Woolsey, and D. J. Stilwell. Planar Flow Model Identification for Improved Navigation of Small AUVs. *Ocean Engineering*, 36(1):119–131, January 2009.

[58] R. W. Beard and T. W. McLain. *Small Unmanned Aircraft: Theory and Practice*. Princeton University Press, Princeton, New Jersey, 2012.

[59] W. Ren, R. W. Beard, and E. M. A. Atkins. A Survey of Consensus Problems in Multi-Agent Coordination. In *American Control Conference*, pages 1859–1864, Portland, Oregon, June 2005.

[60] A. Richards and J. P. How. Aircraft Trajectory Planning with Collision Avoidance Using Mixed Integer Linear Programming. In *American Control Conference*, volume 3, pages 1936–1941, 2002.

[61] M. Ridley, E. Nettleton, A. Goktogan, G. Brooker, A. Sukkarieh, and H. F. Durrant-Whyte. Decentralised Ground Target Tracking with Heterogeneous Sensing Nodes on Multiple UAVs. In *Information Processing in Sensor Networks*, pages 545–565. Springer Berlin/Heidelberg, 2003.

[62] A. Ryan, M. Zennaro, A. Howell, R. Sengupta, and J. K. Hedrick. An Overview of Emerging Results in Cooperative UAV Control. In *IEEE Conference on Decision and Control*, pages 602–607, 2004.

[63] R. Rysdyk. Course and Heading Changes in Significant Wind. *Journal of Guidance, Control, and Dynamics*, 30(4):1168–1171, 2007.

[64] T. Samad, J. S. Bay, and D. Godbole. Network-Centric Systems for Military Operations in Urban Terrain: The Role of UAVs. *Proceedings of the IEEE*, 95(1):92–107, 2007.

[65] R. Sepulchre, D. A. Paley, and N. E. Leonard. Stabilization of Planar Collective Motion: All-to-All Communication. *IEEE Transactions on Automatic Control*, 52(5):811–824, 2007.

[66] R. Sepulchre, D. A. Paley, and N. E. Leonard. Stabilization of Planar Collective Motion with Limited Communication. *IEEE Transactions on Automatic Control*, 53(3):706–719, 2008.

[67] D. Simon. *Optimal State Estimation: Kalman, H [infinity] and nonlinear approaches*. John Wiley & Sons, Inc., New Jersey, 2006.

[68] A. Sinha, T. Kirubarajana, and Y. Bar-shalomb. Autonomous Ground Target Tracking by Multiple Cooperative UAVs. In *Aerospace Conference*, pages 1–9, Big Sky, Montana, 2005.

[69] S. C. Spry, A. R. Girard, and J. K. Hedrick. Convoy Protection Using Multiple Unmanned Aerial Vehicles: Organization and Coordination. In *American Control Conference*, pages 3524–3529, 2005.

[70] T. H. Summers, M. R. Akella, and M. J. Mears. Coordinated Standoff Tracking of Moving Targets: Control Laws and Information Architectures. *Journal Guidance, Control, and Dynamics*, 32(1):56–69, 2009.

[71] S. Susca, F. Bullo, and S. Martinez. Monitoring Environmental Boundaries with a Robotic Sensor Network. *IEEE Transactions on Control Systems Technology*, 16(2):288–296, 2008.

[72] J. W. R. Taylor and K. Munson. *Jane's Pocket Book of Remotely Piloted Vehicles: Robot Aircraft Today*. Collier Books, New York, 1977.

[73] L. Techy, D. A. Paley, and C. A. Woolsey. Unmanned Aerial Vehicle Coordination on Closed Convex Paths in Wind. *Journal of Guidance, Control, and Dynamics*, 33(6):1946–1951, November 2010.

[74] L. Techy, C. A. Woolsey, and D. G. Schmale. Path Planning for Efficient UAV Coordination in Aerobiological Sampling Missions. In *IEEE Conference on Decision and Control*, pages 2814–2819, Cancun, Mexico, December 2008.

[75] J. Tisdale, Z. Kim, and J. K. Hedrick. Autonomous UAV Path Planning and Estimation. *IEEE Robotics and Automation Magazine*, 16(2):35–42, 2009.

[76] J. Tisdale, A. Ryan, D. Tornqvist, and J. K. Hedrick. A Multiple UAV System for Vision-Based Search and Localization. In *American Control Conference*, pages 1985–1990, June 2008.

[77] R. A. Wise and R. T. Rysdyk. UAV Coordination for Autonomous Target Tracking. In *AIAA Guidance, Navigation, and Control Conference*, number AIAA-2006-6453, Keystone, Colorado, August 2006.

[78] P. Zhan, D. W. Casbeer, and A. L. Swindlehurst. Adaptive Mobile Sensor Positioning for Multi-Static Target Tracking. *IEEE Transactions on Aerospace and Electronic Systems*, 46(1):120–132, 2010.

[79] F. Zhang and N. E. Leonard. Coordinated Patterns of Unit Speed Particles on a Closed Curve. *Systems and Control Letters*, 56(6):397–407, 2007.

[80] K. Zhou and S. I. Roumeliotis. Optimal Motion Strategies for Range-Only Constrained Multisensor Target Tracking. *IEEE Transactions on Robotics*, 24(5):1168–1185, 2008.

[81] S. Zhu and D. Wang. Cooperative Ground Target Tracking with Input Constraints. In *International Conference on Control, Automation, Robotics and Vision*, pages 1051–1056, Singapore, 2010.